GROWTH AND CHARACTERIZATION OF EPITAXIAL SILVER INDIUM DISELENIDE

BY

PAMELA PENA MARTIN

DISSERTATION

Submitted in partial fulfillment of the requirements
for the degree of Doctor of Philosophy in Materials Science and Engineering
in the Graduate College of the
University of Illinois at Urbana-Champaign, 2015

Urbana, Illinois

Doctoral Committee:

Professor Angus. A. Rockett, Chair and Director
Professor Joseph Lyding
Emeritus Profesor John R. Abelson
Assistant Professor Andre Schleife

ABSTRACT

Photovoltaics (solar cells) are a key player in the renewable energy frontier, and will become increasingly important as their cost per watt continues to drop, especially if fossil fuel costs increase. One particularly promising photovoltaic technology is based on chalcopyrite-structure semiconductors. Within the chalcopyrite compounds the highest efficiency thin film solar cell absorber material to date is $Cu(In,Ga)Se_2$ (CIGS). While current efficiency records are over 21% for single-junction cells, there is still room for improvement. Replacing some of the Cu with Ag has been shown to be beneficial in CIGS devices. However, the Ag- containing chalcopyrites are still relatively unknown in terms of their growth mechanism, energetics, and surface atomic and electronic properties. These are best inferred through study of epitaxial films, yet they have little mention in literature and have not been the subject of a detailed study. This work describes the growth of epitaxial $AgInSe_2$ (AIS) on GaAs substrates, studying the morphology, structure, and surface properties to understand how growth takes place. It also seeks to experimentally determine the surface electronic and atomic structure at the atomic scale to gain insight into the part of the material that forms the heterojunction that collects photon energy in the device. Finally, this work seeks to compare and contrast these findings with what is known about CIGS to determine where similarities and, more importantly, the differences may lie.

This study has found that single phase tetragonal AIS can be epitaxially grown on GaAs, as illustrated by x-ray diffraction (XRD), transmission electron microscope (TEM), and surface morphology data. Like CIGS, the close packed polar (112) planes have the lowest energy. The morphology points to a difference in step dynamics, leading to less faceted, straight edged island shapes compared to CIGS. Epitaxial temperature as a function of growth direction shows a different trend in AIS than in CIGS. Interdiffusion of the group III elements across the substrate interface

was found to result in an epitaxial intermixed layer between the film and substrate in some cases, which may help mediate the lattice mismatch.

At the atomic scale, scanning tunneling microscopy (STM) was used to observe details of the surface morphology, which indicated growth of the (112)A orientation of AIS by a screw dislocation mechanism (other surfaces were not examined by STM but are expected to show similar results). The surface atomic structure was directly imaged for the first time, revealing an arrangement similar to that expected from a bulk terminated surface. The electronic structure shows a gap in surface electronic states with a width comparable to bulk AIS, n-type conduction, and a tail of states near the valence band edge that decay well into the gap. The conduction and valence bands show fluctuations as a function of position on the surface, with greater magnitude in the valence band. The fluctuations in both bands are less than those observed on the surface of CIS by STM. It seems to indicate a reduction in band tails, both in magnitude and spacial extent, in AIS compared to CIS, likely tied to a reduction in point defect concentration at the surface.

Dedication

I dedicate this work first and foremost to my beautiful daughter Adela, who I hope will always be the compassionate, fearless, and genuinely funny person that she is now at almost three.

I also dedicate this to my husband Jeronimo who has tirelessly and enthusiastically supported me throughout this thesis. He has accepted all my venting, worry, and strife that is a part of graduate work, and returned it all with kindness and understanding.

Finally, I dedicate this to my late grandparents Ralph and Ruth DeMarco and Ira and Martha Martin, and my late great grandmother Madeline DeMarco, who did not survive to see me finish this thesis, but who held me up with encouragement, prayers, and words of wisdom throughout my life.

Acknowledgements

I am deeply grateful for the opportunity to pursue my graduate studies at the University of Illinois in the Materials Science department. I gratefully acknowledge the support of the International Institute for Carbon Neutral Energy Research (WPI-I2CNER), sponsored by the Japanese Ministry of Education, Culture, Sports, Science and Technology. I owe a huge debt of gratitude to my thesis advisor Angus Rockett who has been a mentor, source of encouragement, and a great model as a researcher and person. Countless times I would seek his guidance, with some question, frustration, or problem that I faced, and after a helpful conversation, I always left his office uplifted, encouraged, and motivated. His unwavering support of gender equity is unmatched, and I will never forget his support for me in the time I became a mother during my graduate studies, allowing me to make that transition in a positive and entirely supported environment. I am also extremely thankful for my thesis committee. Prof. Joseph Lyding, who graciously let me use his scanning tunneling microscopes, has been a valuable mentor and guide not only in my work, but he has helped me to connect with female mentors in my field who have also been a significant encouragement to me. Prof. John Abelson has been an important influence on my work, providing helpful feedback and interesting, thought provoking questions from preliminary exam onward. I have also had the privilege of learning a great deal about the learning process and teaching from him. Prof. Andre Schleife has been an enthusiastically supportive member of my committee, and I am so grateful for discussions with him about research and also career paths. I am also thankful for Prof. Lane Martin, who served on my preliminary exam committee, whose valuable insight was significant in this thesis. My committee as a whole has provided great insight, helpful questions, and encouraging words when needed. I have greatly benefited from their guidance, and I believe I am a better scientist because of their influence. I am also grateful for the guidance and wisdom imparted to me from Prof. Elif Ertekin, who has been a great encouragement to me for these last few years of

graduate school. I also must recognize my undergraduate research advisor Prof. Tom Oder at Youngstown State University, who first introduced me to the world of scientific research. Working with him sparked my interest in electronic materials, and it was his kind and gentle leadership and encouragement that led me to pursue graduate studies in the first place.

This long and winding road of graduate school has been made so much more fulfilling, interesting, and enjoyable due to being surrounded by an amazing group of coworkers. This list includes fellow "Rocketeers" past and present including Angel Aquino, whose sense of humor made the office a happy place to be, and who always had something encouraging to say at the right moment; Allen Hall, who has greatly contributed to my research with his ideas and advice, as well as purveyor of a wealth of information on such a wide variety of topics from fungi to polymers; Damon Hebert, a kind and helpful colleague who taught me so much about film growth; Dan Heinzel, whose always greets me with his token "Yo!" greeting, and who is always happy to trade puns with me; Thomas Erickson, an especially kind colleague whose patience and helpfulness are unmatched; Zhengfeng Yang, always an encouraging friend to me when we shared an office, and who shared delicious Chinese snacks with me; Elizabeth Pogue, who always amazes me with her apparently boundless energy and enthusiasm for research and science; Mohit Tuteja, who took part in many helpful discussions with me; Xiaoqing He, who has been a kind friend to me, in addition to his assistance with the TEM work in this thesis; Nicole Johnson, who has given me so much insight into the teaching world; Justin Kardel, my latest office mate and coffee buddy; and the newest group members Kara Kearney, May-Ling Li, Leah Moldauer, and Michael Darrow, who have all been a joy to get to know; "half-Rocketeer" Stephen House, who I was blessed to work alongside in a research project as well as in teaching, and from whom I learned how to properly use the word "whelmed"; "visiting Rocketeers" Zhen Zhou, Yiming Liu, and Po-chuan Tsai; Lyding group members Wei Ye, who taught me so much of what I know about scanning tunneling microscopy, Justin Koepke, Scott

Schmucker, Gregory Scott, Sumit Ashtekar, Kevin He, Adrian Radocea, and the rest of the gang; and other wonderful friends including Nam-hoon Kim, Navneet Kumar, Marta Trelka, Nihan Yonet, Grazyna Antczak, Xinning Ho, and Martin Bettge.

Much of my microanalysis work was carried out in the CMM, where I had the pleasure of working with staff members who are not only highly skilled, knowledgeable, and talented, but also extremely kind, helpful, and truly wonderful people. I would like to specifically acknowledge Jim Mabon, Scott Maclaren, Timothy Spila, Richard Haasch, Mauro Sardela, Julio Soares, Steve Burdin, and Vania Petrova for their work in helping to train me, answer questions, provide helpful discussions about results, and for just generally being such wonderful people.

I am also grateful for our building custodian, Russel, who always has an encouraging and positive thing to say in the morning when I arrive, and keeps our work space looking so nice.

Outside of the academic sphere, I am also deeply indebted to my parents, Ron and Patty Martin, who gave me the courage and support to follow my dreams, cheerfully took the 450 mile journey to Illinois from Ohio many, many times to spend time with me, and have paved my life's path with their prayers; to my sister Melanie, who I can always count on to make me laugh and brighten my day; my brother David; to my aunts and uncles and cousins who have been a source of comfort, advice, friendship, and love; and to my dear lifelong friend Kari for being a light and encouragement to me always.

TABLE OF CONTENTS

CHAPTER 1

INTRODUCTION

1.1 Motivation

Solar cells are likely to become a major player in the energy sector for a number of reasons. Cutting back significantly on production of pollution is vital to ensuring that the earth remains a place that can sustain life. The use of fossil fuels, especially coal, as a source of electricity has significant drawbacks, particularly in the lasting effects of the pollution it contributes. The World Health Organization released an alarming study that reported that one in eight deaths worldwide in 2012 (over 7 million people) were a result of exposure to air pollution, with those in lower income classes in the Pacific and south Asian regions experiencing the most significant effects of this [1]. Moving toward alternate sources of electricity that do not produce pollution is critical. Solar energy provides a clean and renewable option for supplying electricity for households or industrial use.

Thin films of $Cu(In,Ga)Se_2$ (CIGS) are a promising technology among the available options for the absorber layer in photovoltaic devices. Thin film technologies take advantage of materials with a high absorption coefficient, which are used to make high performing solar cells from a thin layer, hence less raw material. No thin film polycrystalline material to date has a record efficiency that beats CIGS. The current top research cell efficiency of 21.7% for $Cu(In,Ga)Se_2$ devices is held by ZSW [2]. The CIGS system represents just one set of materials within the I-III-VI_2 chalcopyrites, an attractive system for electronic applications due to the fact that one can tune the band gap by substitution of atoms from any of the groups. For example, $CuIn_xGa_{1-x}Se_2$ has a gap that ranges between 1.0 eV (x=1) to 1.68 eV (x=0) and can be controlled through group III composition. While this has typically been exploited for chalcopyrite based photovoltaics, the group I composition offers another option for further tuning of the band gap.

$AgInSe_2$ (AIS) is a promising optoelectronic semiconductor with a band gap and absorption coefficient that make it ideal for the absorber layer in photovoltaic devices. Preliminary studies have shown Ag incorporation into CIGS devices is beneficial to device performance in a number of ways. Spectrophotometer experiments CIGS with added Ag shows less sub-gap absorption, suggesting that defect densities are reduced [3]. Ag also has the effect of widening the band gap of CIGS, which leads to improved open circuit voltage and increased efficiency compared to CIGS alone [4], [5]. The additional of Ag to CIS also serves to improve the uniformity of the material as well, as observed by cryogenic cathodoluminescence studies, which found less inter- and inner- grain fluctuations in luminescence compared to CIS [6]. However, significantly less work has been done on understanding some of the fundamental properties regarding growth mechanisms and surface energetics, which are key to developing and improving Ag-based devices. There have been no dedicated studies on epitaxial growth of AIS, which is the best way to learn about these properties. The surface properties of CIS are key to its operation, yet even after decades of study there are still questions that remain. AIS has been the subject of relatively few studies that have reached no consensus on things like the presence or identity of a surface ordered defect compound, and no study has proposed a surface reconstruction or probed the surface electronic properties. In particular, understanding how any of these characteristics differ from related and better known CIS will have implications on how to go about improving devices that contain Ag.

The purpose of this work is to shed light on several key properties of AIS. These include developing and exploiting a method for the growth of epitaxial layers of AIS, to better understand its growth and surface energetics, as well as utilizing surface analysis techniques to determine the surface atomic and electronic structure. These properties are compared to CIS in order to elucidate the important similarities and differences that are relevant to AIS as a candidate photovoltaic absorber layer.

1.2 Thesis statement

The growth mechanism and properties of $AgInSe_2$ are inferred through study of vapor phase grown epitaxial films. The surface atomic structure, chemistry, and electronic properties have been studied at the micro- and nano-scale to determine the effects of growth parameters on the morphology, defects, and electronic behavior. These results are then compared to other I-III-VI2 chalcopyrite materials, to help relate this information to possible improvement in device performance.

1.3 Thesis summary

This work has two main foci that have been studied and are presented here. This includes study of AIS growth mechanisms and detailed atomic scale surface analysis. **Chapter 2** provides relevant background to set the story for where this work takes the stage. The results of previous studies of epitaxial growth of other chalcopyrites are relayed to highlight the importance of this type of study. Relevant work related to the growth of AIS and its related compounds are also described and their findings stated. Finally, a background of scanning tunneling microscopy (STM) and spectroscopy (STS) is given, with particular emphasis on study of chalcopyrite surfaces by these techniques.

Chapter 3 provides details about the experiments performed throughout the course of this study. This chapter includes sections that describe the film growth process, growth conditions for this study, special sample preparation methods, microanalysis instrument use and conditions, and details about the custom built STM used for this study.

The next four chapters contain the results and analysis of these experiments described in Chapter 3. **Chapter 4** contains an analysis of the morphology of the epitaxial films of AIS as a function of growth direction and temperature, and uses this to help describe the growth mechanism for epitaxial films in the AIS/GaAs system. It is shown that the (112) close packed polar planes of

AIS are the lowest in energy, given by their preference to form (112) facets even when growth propagates on non-polar surfaces. The morphological features of AIS grown on GaAs (110) are studied as a function of growth temperature and both thermodynamic roughening of the size scale of morphological features and a smoothing out of facet surfaces, due to increased adatom diffusion length during growth, are observed.

In **Chapter 5**, the film and interface structure are studied, providing confirmation of epitaxial growth of single phase, fully relaxed chalcopyrite films. The conditions to obtain epitaxial growth are discussed, in particular the minimum substrate temperatures for epitaxial growth as a function of substrate orientation. The interface between the film and substrate are directly observed by transmission electron microscopy, revealing the presence of an epitaxial interface layer that forms out of the top layer of the GaAs substrate during growth. This layer, with its intermediate lattice parameter between film and substrate, is likely important for making epitaxial growth possible and improving film adhesion. Ga diffusion from the substrate into the film during growth is also observed, and study of the film Ga profiles have made it possible to extract an activation energy for Ga diffusion in AIS, which may be of critical importance to know for fabrication of devices that require a specific Ga gradient.

The next two chapters discuss surface analysis carried out primarily by STM and STS. **Chapter 6** reveals atomic scale steps and terrace edges of AIS (112)A, giving direct evidence of screw dislocations as a likely mechanism for growth. The terrace edges are observed to contain a high density of kinks, indicating a much lower kink energy in AIS than related compound CIS. The surface has been atomically resolved for the first time, which has revealed an atomic arrangement that appears to be similar to bulk terminated AIS (112). The possible reasons for why CIS is so much more difficult to be resolved is discussed as well.

Chapter 7 examines the electronic properties of the surface of AIS by STS. Current-voltage measurements indicate that the surface of AIS is n-type, like bulk AIS, with a decaying tail of states located at the valence band edge. Fluctuations in the band edges have been observed as a function of distance on the surface give a unique way to observe band tail fluctuations at the nm-scale that techniques such as PL are not capable of showing. The fluctuations in AIS are much less than observed in CIS, which corroborates bulk PL measurements at the atomic scale, and lends credibility to AIS as a material for high performance devices.

This thesis concludes with **Chapter 8**, which is a summary of the above work, along with suggested routes for continuation of this work.

The results contained in Chapters 4-7 each represent a complete manuscript, either in preparation close to the submission stage or already accepted and published. These include:

(Chapter 4) P. Peña Martin and A. Rockett "Growth Mechanisms and Surface Morphology of $AgInSe_2$" (manuscript in preparation).

(Chapter 5) P. Peña Martin, X. He, and A. Rockett "Characterization of epitaxial $AgInSe_2$ thin films grown on GaAs" (manuscript in preparation).

(Chapter 6) P. Peña Martin, J. Lyding, and A. Rockett "Growth mechanism and surface atomic structure of $AgInSe_2$" Journal of Vacuum Science and Technology A **30** 04D115 (2012).

(Chapter 7) P. Peña Martin, J. Lyding, and A. Rockett "Scanning tunneling spectroscopy of epitaxial silver indium diselenide" Surface Science **636** 8-12 (2015).

In addition to the work outlined in this thesis, I have contributed to other projects that resulted in the following papers:

W. Ye, P. Peña Martin, N. Kumar, S. Daly, A. Rockett, J. Abelson, G. Girolami, and J. Lyding "Direct writing of sub-5 nm hafnium diboride metal nanostructures" ACS Nano **4**(11) 6818-6824 (2010).

W. Ye, K. Min, P. Peña Martin, A. Rockett, N. Aluru, and J. Lyding "Scanning tunneling spectroscopy and density functional calculation of silicon dangling bonds on the Si(100)-2x1:H surface" Surface Science **609** 147-151 (2013).

Kim, N., P. Peña Martin, A. Rockett, and E. Ertekin, "Phase stability of $CuInSe_2$, $AgInSe_2$, and $AuInSe_2$ comparison of conventional and screened-exchange density functional theory descriptions" (manuscript in preparation).

1.4 References

[1] World Health Organization, "Burden of disease from the joint effects of Household and Ambient Air Pollution for 2012," vol. 35, no. February, p. 17, 2014.

[2] M. A. Green, K. Emery, Y. Hishikawa, W. Warta, and E. D. Dunlop, "Solar cell efficiency tables (Version 45)," *Prog. Photovoltaics Res. Appl.*, vol. 23, no. 1, pp. 1–9, 2015.

[3] J. Boyle, G. Hanket, and W. Shafarman, "Optical and quantum efficiency analysis of (Ag,Cu)(In,Ga)Se_2 absorber layers," *Conf. Rec. 34th IEEE Photovoltaics Spec. Conf. June 7-12, 2009 Philadelphia, PA*, pp. 1349–1354, 2009.

[4] W. Shafarman, C. Thompson, J. Boyle, G. Hanket, P. Erslev, and J. D. Cohen, "Device characterization of (AgCu)(InGa)Se_2 solar cells," in *Photovoltaic Specialists Conference (PVSC), 2010 35th IEEE*, 2010, pp. 325–329.

[5] G. M. Hanket, J. H. Boyle, W. N. Shafarman, and G. Teeter, "Wide-bandgap (AgCu)(InGa)Se_2 absorber layers deposited by three-stage co-evaporation," *Proc. 2010 IEEE World Conf. Photovolt. Energy Convers.*, pp. 003425–003429, 2010.

[6] A. R. Aquino, A. A. Rockett, S. A. Little, and S. Marsillac, "Cryogenic cathodoluminescence from $Cu_xAg_{1-x}InSe_2$ thin films," *Photovolt. Spec. Conf. (PVSC), 2010 35th IEEE*, pp. 3386–3390, 2010.

CHAPTER 2

BACKGROUND

Here the backstory that motivates this work will be presented. A summary on chalcopyrite semiconductors and their relevance to photovoltaics will open this chapter. Next the $AgInSe_2$ (AIS) compound will be introduced. The following section will describe previous studies on epitaxial chalcopyrite films. Next will be a discussion of surface study of chalcopyrite materials in both theory and experiment, as well as an overview of what is known about the AIS surface. Finally an overview of scanning tunneling microscopy (STM) studies on chalcopyrite semiconductors will be presented.

2.1 Chalcopyrite semiconductors

$Cu(In,Ga)Se_2$ (CIGS) is the top performing thin film photovoltaic absorber layer material that currently holds the world record for its category among research grade devices [1]. Its high absorption coefficient and ability to tolerate (or excel due to) point defects make it a promising contender among solar cell technologies. A further benefit to this material is that it consists of an alloy of two compounds, $CuInSe_2$ and $CuGaSe_2$, with band gaps of 1.02 and 1.68 eV, respectively, that allow the band gap of the resulting alloy to be tuned with In:Ga ratio. While CIGS is the most well-known, other substitution of group I, III, or VI atoms also have the potential for further broadening the band gaps that can be covered. Group I atom substitution has been investigated primarily with Ag showing promising results in combination with CIGS.

AIS is a direct gap semiconductor with a band gap of 1.25 eV [2], high absorption coefficient, and also miscible with CIGS such that it offers the possibility of further widening the gap of CIGS currently used in high performance devices, which are limited by degradation when the Ga/(In+Ga) increases beyond 30%, limiting the band gap to about 1.2 eV.

2.2 $AgInSe_2$ growth studies

Since the first bulk samples were prepared in 1953 [3], AIS has been grown by a variety of techniques including the Bridgeman method [4]–[12], stoichiometric melt [2], [13]–[17], vertical gradient freeze method [18], and hot press [19], [20]. Thin films of AIS are more technologically relevant, and AIS films have been obtained through a variety of thin film deposition techniques including evaporation from bulk material [21]–[24], electrodeposition [25], several variations of sputtering [26]–[30], flash evaporation from powder [31]–[34], pulsed laser deposition [35], [36], coevaporation or molecular beam epitaxy [37]–[45], screen printing [46], hot walled evaporation [47], and sol-gel deposition [48].

The hybrid growth process, which involves a combination of magnetron sputtering and evaporation, is advantageous because it can be scaled up for commercial processing and it allows composition to be controlled easily through sputtering current. This technique has been applied to polycrystalline and epitaxial thin films of CIS, and more recently has been used for polycrystalline films of AIS.

2.3 Epitaxial chalcopyrite thin films

Epitaxial growth of thin films allows one to elucidate growth dynamics and surface energetics without the presence of grain boundaries to complicate the results. Since epitaxial growth continues the stacking of the substrate's crystal structure, the film growth direction can be controlled through choosing the orientation of substrate for growth. The thin film studies to date on AIS have almost exclusively been on polycrystalline or amorphous films, with only one study that observes epitaxial growth of AIS, which utilized hot walled evaporation on Si(100) substrates and did not elaborate on the growth mechanism [47].

CIGS, on the other hand, has been the subject of a number of epitaxial growth studies that have shed important light on its growth behaviors, establishing that the polar (112) orientations are

lowest energy, so much so that it shows a preference to exposing these planes rather than grow nonpolar (220) films when grown on GaAs(110) substrates [49]. Experimental results have proved that the surface is stabilized by point defects, particularly Cu vacancies, using angle resolved x-ray photoelectron spectroscopy [50]. This finding is especially important because it not only offers a mechanism to explain the low surface energy associated with these planes, which was corroborated by density functional theory calculations [51], but it provided an explanation for the reason that the heterojunction partner CdS is so significant, since the near surface vacancies provided lattice sites where Cd could then migrate to dope the surface, thereby forming a homojunction in the CIS [52], [53].

2.4 Scanning tunneling microscopy

The scanning tunneling microscope (STM), a tool developed by Binnig and Rohrer [54], is an especially valuable tool for learning about the surface properties of materials, since it gives a direct measurement of both topography and the local density of states. The beauty of STM is in its ability to show atomically resolved images of a surface in real space, unlike diffraction techniques that give a reciprocal space rendering that needs to then be translated into real space coordinates. This is important in determining things like the surface reconstruction of surfaces.

The principle of operation is based on quantum mechanical tunneling, which occurs when when the wave functions from an atom at the end of a sharp tip overlap with those of the surface atoms of the material to be studied, as when the two are brought in close enough proximity. If a bias is placed between them, a net current can flow in either direction, and this current is exponentially dependent on the tip-sample spacing s, with a dependence that is proportional such that

$$I(V) \sim e^{-sK} \int_0^{eV} \rho_s(E_f - eV + E)dE, \quad [55] \qquad (2.1)$$

where V is the applied sample bias, s is the tip-sample spacing, K is a constant, ρ_s is the local density of states of the sample, and E_f is the Fermi level of the system. Thus, as the tip moves spacially

across a surface, sub-angstrom changes in topography will affect the measured tunneling current by a measureable amount. In operation, the STM is often run in constant current mode, in which the tunneling current is set for a particular bias, and as the tip rasters across the surface, in response to changes in current through a feedback loop, the tip height moves inward or outward in order to restore the setpoint current. By sampling different biases, one probes states within different ranges of E_f, which is exploited through scanning tunneling spectroscopy (STS). It has been shown that the differential conductance, dI/dV, is proportional to the local density of states of the sample,

$$\frac{dI}{dV}(V) \propto \rho_s(E_f - eV). \qquad [55] \qquad (2.2)$$

This relation makes it possible to measure the local density of states at a particular location on the surface by sweeping the sample bias and measuring the current.

2.5 Scanning tunneling microscopy of chalcopyrites

There have been a number of STM studies that looked at the surface of CIGS since the late 1980's to try to elucidate the material's surface atomic structure, morphology, and electronic properties. Part of this work used the STM mainly for its ability to resolve surface features at the atomic scale. The earliest of this work was pioneered by Kazmerski and colleagues, who studied CIS that was epitaxially grown on large grain CIS substrates that were fractured in situ in order to be able to examine pristine and oxygen exposed (110) surfaces and grain boundaries [56]. Use of spectroscopic STM (SSTM), in which a laser beam is incident on the sample during the scan to enhance sensitivity to specific atoms, was used to identify the surface atoms, observe defects, and modify the surface using the STM tip to place oxygen atoms near defect sites in the vicinity of a Σ9 grain boundary [57], [58]. Apart from use of nano-electron beam induced current (nano-EBIC) near grain boundaries, most of this work was looking at the atomic structure and used SSTM as a means of determining the identity of atoms [57]–[59]. No one else has been able to obtain such clear

atomically resolved images found in these studies, and the results have not been able to resolve topics of huge debate within the community, such as identifying the surface reconstruction. Additionally, much of this work looked at (220) surfaces of CIS, which are of less interest than the preferred low energy (112) planes that are most relevant to devices because they are typically the exposed surface that forms the heterojunction.

Use of the STM as a probe of electronic information about the surface began with Riedl et al., who studied air-exposed thin film polycrystalline CIS by STS and found that Cu-rich samples showed both p-type and metallic behavior in different regions, presumably with metallic behavior being due to metallic surface phases, and variations across the sample were attributed to fluctuations in composition [60]. It is expected that composition, hence electronic properties, would lead to differences in local density of states as measured by STM, and this has been exploited to help characterize super lattice structures based on $Cu_xIn_{2-x}Se2$ by examining fracture cross sections [61]. Another study looked at both p- and n-type CIS and found an STS-obtained surface bandgap gap of less than 1 eV and around 1.3 eV for p-type and n-type samples, respectively [62]. They also reported defect states near both band edges as evidenced in the density of states. STS carried out under laser illumination has been used to observe differences in the local surface photovoltage of CIS from one grain to another, attributed to composition variations [63]. These studies were carried out probing areas too large and samples too rough to be able to get resolution anywhere near atomic scale. Mayer et al. have obtained electronic measurements of the surface of CIS with STS by using careful surface preparations including in situ cleaving of epitaxial layers and in situ sputtering and annealing cycles, resulting in the observation of band edge fluctuations consistent with length scales of a few atoms [64], [65]. Even with a presumably pristine CIS surface, and even when the tip was able to easily resolve the GaAs substrate in close proximity to the interface, the CIS surface did not yield clear atomically resolved images [64]. Mönig et al have used STS to study changes in surface

electronic behavior of CIS near grain boundaries in polycrystalline samples, and differential conductance (dI/dV) data indicate fewer deep defects at the grain boundaries of CIS [66]. They also measured an average band gap of about 1.4 eV for a CIGS sample and observed that the electronic properties obtained at each grain had some variation, though not on the scale of what was observed by Mayer et al [67].

An exhaustive literature search yielded no STM studies of AIS itself, and only one study that looked at the surface of (Cu,Ag)$InSe_2$. This study used contact mode I-V curves carried out in the STM to observe changes in conductivity in a p-n-p junction formed in $Cu_xAg_{1-x}InSe_2$ [68]. While the study found variations in the conductivity throughout regions of the device, as well as demonstrated modulation of photoconductivity in STM scans by use of illumination, no atomically resolved images were obtained and the samples had significantly more Cu than Ag [68].

2.6 References

[1] M. A. Green, K. Emery, Y. Hishikawa, W. Warta, and E. D. Dunlop, "Solar cell efficiency tables (Version 45)," *Prog. Photovoltaics Res. Appl.*, vol. 23, no. 1, pp. 1–9, 2015.

[2] J. L. Shay, B. Tell, H. M. Kasper, and L. M. Schiavone, "Electronic Structure of $AgInSe_2$ and $CuInSe_2$," *Phys. Rev. B*, vol. 7, no. 10, pp. 4485–4490, 1973.

[3] H. Hahn, G. Frank, W. Klingler, A.-D. Meyer, and G. Störger, "über einige ternäre Chalkogenide mit Chalkopyritstruktur," *Z. anorg. allg. Chemie.*, vol. 271, pp. 153–170, 1953.

[4] L. Martinez Z., S. A. Lopez-Rivera, and V. Sagredo, "Preparation and Properties of $AgInS_2$ and $AgInSe_2$ Single Crystals and of the Quaternary Alloys $AgInSe_{2(1-x)}S_{2x}$(*).," *Nuovo Cim.*, vol. 2D, no. 6, pp. 1687–1694, 1983.

[5] T. F. Ciszek, "Melt growth and some properties of $Cu_xAg_{1-x}InSe_2$ and $CuIn_yGa_{1-y}Se_2$ chalcopyrite solid solution crystals," *J. Cryst. Growth*, vol. 79, pp. 689–694, 1986.

[6] D. G. Kilday, G. Margaritondo, T. F. Ciszek, S. K. Deb, S.-H. Wei, and A. Zunger, "Common-anion rule and its limits: Photoemission studies of $CuIn_xGa_{1-x}Se_2$-Ge and $Cu_xAg_{1-x}InSe_2$-Ge interfaces.," *Phys. Rev. B. Condens. Matter*, vol. 36, no. 17, pp. 9388–9391, Dec. 1987.

[7] D. G. Kilday, G. Margaritondo, T. F. Ciszek, and S. K. Deb, "The common-anion rule and the role of cation states: binary versus ternary semiconductors," *J. Vac. Sci. Technol. B Microelectron. Nanom. Struct.*, vol. 6, no. 4, pp. 1364–1368, 1988.

[8] I. V Bodnar, "Properties of $AgGa_xIn_{1-x}Se_2$ Solid Solutions," *Inorg. Mater.*, vol. 40, no. 9, pp. 914–918, 2004.

[9] I. V. Bodnar', "Optical properties of $AgGa_xIn_{1-x}Se_2$ alloys," *Semiconductors*, vol. 42, no. 2, pp. 156–158, Feb. 2008.

[10] S. Ozaki and S. Adachi, "Optical absorption and photoluminescence in the ternary chalcopyrite semiconductor $AgInSe_2$," *J. Appl. Phys.*, vol. 100, no. 11, p. 113526, 2006.

[11] Y. Huang, B. J. Zhao, S. F. Zhu, W. L. Zhu, C. F. Xu, S. Q. Wan, and Z. Y. He, "Properties of $AgGa_{1-x}In_xSe_2$ single crystals grown by Bridgman method," *Cryst. Res. Technol.*, vol. 42, no. 3, pp. 227–230, Mar. 2007.

[12] K. Koitabashi, S. Ozaki, and S. Adachi, "Optical properties of single-crystalline chalcopyrite semiconductor $AgInSe_2$," *J. Appl. Phys.*, vol. 107, no. 5, p. 053516, 2010.

[13] G. H. Chapman, J. Shewchun, J. J. Loferski, B. K. Garside, and R. Beaulieu, "Lattice constants and band-gap variations of the pentenary semiconductor system $Cu_{1-y}Ag_yInS_{2(1-x)}Se_{2x}$," *Appl. Phys. Lett.*, vol. 34, no. 11, pp. 735–737, 1979.

[14] N. Goyal, "Electrical and photo-electrical properties of a chalcopyrite," vol. 40, no. 2, pp. 97–105, 1993.

[15] I. V. Bodnar', I. A. Viktorov, and S. L. Sergeev-Nekrasov, "$Cu_{1-x}Ag_xInSe_2$ solid solutions," *Cryst. Res. Technol.*, vol. 33, no. 6, pp. 885–890, 1998.

[16] M. S. Al-Kotb, W. Puff, S. a. Hassan, and M. Mohsen, "A Study of Vacancy-Like Defects in the Chalcopyrite Semiconductor $AgInSe_2$," *Mater. Sci. Forum*, vol. 363–365, pp. 150–152, 2001.

[17] J. G. Albornoz, R. M. Rojas L., J. M. Merino, and M. León, "Structural, thermal and electrical properties of the semiconductor system $Ag_{(1-x)}Cu_xInSe_2$," *J. Phys. Chem. Solids*, vol. 75, no. 1, pp. 1–7, Jan. 2014.

[18] K. Yoshino, "Optical and electrical properties of $AgIn(S,Se)_2$ crystals," *Phys. B Condens. Matter*, vol. 302–303, pp. 349–356, 2001.

[19] K. Kishigui, K. Abe, G. Murakami, Y. Shim, K. Yoshino, and K. Wakita, "Study of steady-state photoluminescence of $AgInSe_2$ crystals," *Thin Solid Films*, vol. 517, no. 4, pp. 1445–1448, 2008.

[20] K. Yoshino, a Kinoshita, Y. Shirahata, M. Oshima, K. Nomoto, T. Yoshitake, S. Ozaki, and T. Ikari, "Structural and electrical characterization of $AgInSe_2$ crystals grown by hot-press method," *J. Phys. Conf. Ser.*, vol. 100, no. 4, p. 042042, Mar. 2008.

[21] S. M. Patel and A. D. Patel, "Electrical resistivity of polycrystalline $AgInSe_2$ thin films," *Mater. Lett.*, vol. 2, no. 2, pp. 127–130, 1983.

[22] Y. Ema and N. Harakawa, "Formation and properties of $AgInSe_2$ thin films deposited from alloy chunks," *Jpn. J. Appl. Phys.*, vol. 34, pp. 3260–3265, 1995.

[23] D. Abdel-Hady and A. M. Salem, "Electrical resistivity of $AglnSe_2$ films," *Physica A*, vol. 242, pp. 141–149, 1997.

[24] A. Ammar, "Heat treatment effect on the structural and optical properties of $AgInSe_2$ thin films," *Vacuum*, vol. 66, no. 1, pp. 27–38, Jun. 2002.

[25] D. Raviendra and J. K. Sharma, "n-CdS / p-$AgInSe_2$ Solar Cells by Electrodeposition," *Phys. Status Solidi*, vol. 365, pp. 365–368, 1986.

[26] R. D. Weir, P. E. Jessop, and B. K. Garside, "Growth and annealing of $AgInSe_2$ thin films," *Can. J. Phys.*, vol. 65, pp. 1033–1036, 1987.

[27] A. R. Aquino, A. A. Rockett, S. A. Little, and S. Marsillac, "Cryogenic cathodoluminescence from $Cu_xAg_{1-x}InSe_2$ thin films," *Photovolt. Spec. Conf. (PVSC), 2010 35th IEEE*, pp. 3386–3390, 2010.

[28] T. Begou, S. A. Little, A. Aquino, V. Ranjan, A. Rockett, R. W. Collins, and S. Marsillac, "In situ and ex situ characterization of (Ag, Cu)$InSe_2$," in *Photovoltaic Specialists Conference (PVSC), 2011 37th IEEE*, 2011, vol. 1, no. i, pp. 326–328.

[29] Y. Tauchi, K. Kim, H. Park, and W. Shafarman, "Characterization of (AgCu)(InGa)Se_2 Absorber Layer Fabricated by a Selenization Process from Metal Precursor," *IEEE J. Photovoltaics*, vol. 3, no. 1, pp. 467–471, 2013.

[30] M. A. Abdullaev, a. K. Akhmedov, D. K. Magomedova, and P. P. Khokhlachev, "Properties of $AgInSe_2$ films grown by magnetron sputtering," *Inorg. Mater.*, vol. 48, no. 10, pp. 987–990, Sep. 2012.

[31] C. M. Joseph and C. S. Menon, "Electrical conductivity , optical absorption and structural studies in $AgInSe_2$ thin films," *Semicond. Sci. Technol.*, vol. 11, pp. 1668–1671, 1996.

[32] P. P. Ramesh, S. Uthanna, B. S. Naidu, and P. Jayarama, "Photoconductive response of polycrystalline n-$AglnSe_2$, thin films," *Vacuum*, vol. 47, no. 95, pp. 211–213, 1996.

[33] H. Matsuo, K. Yoshino, and T. Ikari, "Preparation of $AgInSe_2$ thin films grown by vacuum evaporation method," *Phys. Status Solidi*, vol. 3, no. 8, pp. 2644–2647, 2006.

[34] D. Pathak and R. K. B. Davinder, "Growth of $AgInSe_2$ on Si (100) substrate by thermal evaporation technique," *Appl. Phys. A*, vol. 95, pp. 843–847, 2009.

[35] V. Y. Rud', V. F. Gremenok, Y. V. Rud', R. N. Bekimbetov, and I. V. Bodnar', "Fabrication and photosensitivity of $AgInSe_2$ / III – VI isotypic heterojunctions," *Semiconductors*, vol. 33, no. 10, pp. 10–12, 1999.

[36] H. Mustafa, D. Hunter, A. K. Pradhan, U. N. Roy, Y. Cui, and A. Burger, "Synthesis and characterization of $AgInSe_2$ for application in thin film solar cells," vol. 515, pp. 7001–7004, 2007.

[37] M. C. S. Kumar and B. Pradeep, "Photo-electrical properties of silver indium selenide thin films," *Solid State Phys.*, pp. 287 – 291, 2003.

[38] T. Nakada, K. Yamada, R. Arai, H. Ishizaki, and N. Yamada, "Novel wide-band-gap $Ag(In_{1-x}Ga_x)Se_2$ thin film solar cells," *Mater. Res. Soc. Proc.*, vol. 865, pp. 1–8, 2005.

[39] K. Yamada, N. Hoshino, and T. Nakada, "Crystallographic and electrical properties of wide gap $Ag(In_{1-x},Ga_x)Se_2$ thin films and solar cells," *Sci. Technol. Adv. Mater.*, vol. 7, no. 1, pp. 42–45, Jan. 2006.

[40] P. T. Erslev, J. Woo, W. N. Shafarman, and J. D. Cohen, "The in fluence of Na on metastable defect kinetics in CIGS materials," *Thin Solid Films*, vol. 517, no. 7, pp. 2277–2281, 2009.

[41] G. M. Hanket, J. H. Boyle, W. N. Shafarman, and G. Teeter, "Wide-bandgap $(AgCu)(InGa)Se_2$ absorber layers deposited by three-stage co-evaporation," *IEEE*, pp. 3425–3429, 2010.

[42] C. A. Arredondo and G. Gordillo, "Photoconductive and electrical transport properties of $AgInSe_2$ thin films prepared by co-evaporation," *Phys. B Condens. Matter*, vol. 405, no. 17, pp. 3694–3699, Sep. 2010.

[43] J. H. Boyle, B. E. McCandless, G. M. Hanket, and W. N. Shafarman, "Structural characterization of the $(AgCu)(InGa)Se_2$ thin film alloy system for solar cells," *Thin Solid Films*, vol. 519, no. 21, pp. 7292–7295, Jan. 2011.

[44] H. Simchi, B. E. Mccandless, K. Kim, J. H. Boyle, R. W. Birkmire, and W. N. Shafarman, "An Investigation of the Surface Properties of $(Ag,Cu)(In,Ga)Se_2$ Thin Films," *IEEE J. Photovoltaics*, vol. 2, no. 4, pp. 519–523, 2012.

[45] L. Chen, J. Lee, and W. N. Shafarman, "The Comparison of $(Ag ,Cu)(In,Ga)Se_2$ and $Cu(In, Ga)Se_2$ Thin Films Deposited by Three-Stage Coevaporation," *IEEE J. Photovoltaics*, vol. 4, no. 1, pp. 447–451, 2014.

[46] S. Nomura, Y. Matsuo, and T. Wada, "Fabrication of $(Cu,Ag)InSe_2$ Thin," *Mater. Res.*, vol. 1012, pp. 3–6, 2007.

[47] D. Pathak, R. K. Bedi, and D. Kaur, "Growth of heteroepitaxial $AgInSe_2$ layers on Si(100) substrates by hot wall method," *Optoelectron. Adv. Mater.*, vol. 4, no. 5, pp. 657–661, 2010.

[48] F. A. Al-Agel and W. E. Mahmoud, "Synthesis and characterization of AIS chalcopyrite thin films for solar cell applications," *Mater. Lett.*, vol. 82, pp. 82–84, Sep. 2012.

[49] D. Liao and A. Rockett, "Epitaxial growth of $Cu(In,Ga)Se_2$ on GaAs(110)," *J. Appl. Phys.*, vol. 91, no. 4, pp. 1978–1983, 2002.

[50] D. Liao and A. Rockett, "Cu depletion at the $CuInSe_2$ surface," *Appl. Phys. Lett.*, vol. 82, no. 17, p. 2829, 2003.

[51] S. Zhang and S.-H. Wei, "Reconstruction and energetics of the polar (112) and $(1\bar{1}\bar{2})$ versus the nonpolar (220) surfaces of $CuInSe_2$," *Phys. Rev. B*, vol. 65, no. 8, pp. 1–4, Feb. 2002.

[52] D. Liao and A. Rockett, "Cd doping at the $CuInSe_2$/CdS heterojunction," *J. Appl. Phys.*, vol. 93, no. 11, pp. 9380–9382, 2003.

[53] Y. M. Strzhemechny, P. E. Smith, S. T. Bradley, D. X. Liao, A. A. Rockett, K. Ramanathan, and L. J. Brillson, "Near-surface electronic defects and morphology of $CuIn_{1-x}Ga_xSe_2$," *J. Vac. Sci. Technol. B Microelectron. Nanom. Struct.*, vol. 20, no. 6, p. 2441, 2002.

[54] G. Binnig, H. Rohrer, C. Gerber, and E. Weibel, "7x7 Reconstruction on Si(111) resolved in real space," *Phys. Rev. Lett.*, vol. 50, no. 2, pp. 120–123, 1983.

[55] L. B. Ruppalt, "Integration of Single-Walled Carbon Nanotubes with Gallium Arsenide (110) and Indium Arsenide (110) surfaces: a scanning tunneling microscopy study," no. 110, pp. 1–155, 2007.

[56] L. L. Kazmerski, "Atomic imaging and microanalysis of photovoltaic semiconductor surfaces and interfaces," *Proc. 20th IEEE Photovolt. Spec. Conf. IEEE, New York 19891*, 1988.

[57] F. A. Abou-Elfotouh, L. L. Kazmerski, A. M. Bakry, and A. Al-Douri, "Correlation of single-crystal $CulnSe_2$ surface processing with defect levels and cell performance," *(IEEE, Kissimmee, FL, 1990)*, pp. 541–545, 1990.

[58] L. L. Kazmerski, "Specific atom imaging, nanoprocessing, and electrical nanoanalysis with scanning tunneling microscopy," *J. Vac. Sci. Technol. B Microelectron. Nanom. Struct.*, vol. 9, no. 3, p. 1549, May 1991.

[59] L. Kazmerski, "Atomic-level imaging, processing and characterization of defects and surfaces using proximal probe techniques," *Vacuum*, vol. 43, no. 11, pp. 1011–1017, Nov. 1992.

[60] W. Riedl, J. Rimmasch, V. Probst, F. Karg, and R. Guckenberger, "Surface microstructure of CIS thin films produced by rapid thermal processing," *Sol. Energy Mater. Sol. Cells*, vol. 35, pp. 129–139, Sep. 1994.

[61] R. P. Raffaelle, J. G. Mantovani, and R. Friedfeld, "Scanning tunneling microscopy of electrodeposited $CuInSe_2$ nanoscale multilayers," *Sol. Energ. Mat. Sol. C.*, vol. 46, no. 3, pp. 201–208, Jun. 1997.

[62] Z. Zhang, P. Heuell, M. Kulakov, and B. Bullemer, "Surface energy band gap of polycrystalline $CuInSe_2$ thin-films in tunneling spectroscopy," *Proc. 1994 IEEE 1st World Conf. Photovolt. Energy Convers. - WCPEC (A Jt. Conf. PVSC, PVSEC PSEC)*, vol. 1, pp. 299–302, 1994.

[63] D. Eich, "Lateral inhomogeneities of $Cu(In,Ga)Se_2$ absorber films," *Thin Solid Films*, vol. 361–362, no. 1–2, pp. 258–262, Feb. 2000.

[64] M. A. Mayer, L. B. Ruppalt, D. Hebert, J. Lyding, and A. A. Rockett, "Scanning tunneling microscopic analysis of $Cu(In,Ga)Se_2$ epitaxial layers," *J. Appl. Phys.*, vol. 107, no. 3, p. 034906, 2010.

[65] M. Mayer, P. Martin, J. Lyding, and A. Rockett, "Scanning tunneling microscopy as a probe of defects in $CuInSe_2$," *Conf. Rec. Thirty Fifth IEEE Photovolt. Spec. Conf.*, pp. 233–238, 2010.

[66] H. Mönig, Y. Smith, R. Caballero, C. Kaufmann, I. Lauermann, M. Lux-Steiner, and S. Sadewasser, "Direct Evidence for a Reduced Density of Deep Level Defects at Grain Boundaries of $Cu(In,Ga)Se_2$ Thin Films," *Phys. Rev. Lett.*, vol. 105, no. 11, pp. 2–5, Sep. 2010.

[67] H. Mönig, R. Caballero, C. a. Kaufmann, T. L. Schmidt, M. C. Lux-Steiner, and S. Sadewasser, "Nanoscale investigations of the electronic surface properties of $Cu(In,Ga)Se_2$ thin films by scanning tunneling spectroscopy," *Sol. Energy Mater. Sol. Cells*, vol. 95, no. 6, pp. 1537–1543, Jun. 2011.

[68] N. S. McAlpine, P. McConville, D. Haneman, L. Chernyak, and D. Cahen, "Junction sharpness in field-induced transistor structures in $Cu_xAg_{1-x}InSe_2$," *J. Appl. Phys.*, vol. 79, no. 9, p. 7370, 1996.

CHAPTER 3

EXPERIMENTAL METHODS

3.1 Introduction

In this chapter, the experimental details for the procedures in this thesis are described. The first section of this chapter explains the growth procedure for obtaining epitaxial films, including details about the growth chamber and parameters used for samples included in this study. The next section includes information about the analytical equipment used to characterize the films. The last section describes the custom built scanning tunneling microscope used in this study, as well as a discussion on the preparation of pristine samples for surface analysis.

3.2 Film growth

Thin films of AIS were grown by a hybrid growth process in a custom built stainless steel vacuum chamber with a base pressure of $4x10^{-6}$ torr. The chamber is equipped with two magnetrons, which in this study were used to sputter 4" Ag and In targets, and a Knudsen effusion cell, which supplied the Se. Films were grown on epi-ready GaAs substrates purchased from MTI, polished to (001), (110), (111)A, and (111)B orientations, the last of which correspond to cation and anion terminated GaAs(111), respectively. The samples were held in place on a resistive substrate heater with clips, and samples were heated through a programmed ramp up to set point temperatures that ranged from 500-740°C during growth, measured by thermocouple inserted in the substrate heater. A schematic of the growth chamber is shown in Fig. 3.1 that illustrates the configuration of the sources in the chamber. The substrates were clipped to a resistive substrate heater which faces downward, while the magnetrons and effusion cell face upward pointed toward the center of the heater.

Samples were brought to the growth temperature in twelve minutes, and during the ramp up the magnetrons were turned on while the substrate and magnetrons were still covered by shutters to

allow several minutes of initial sputtering as a means of cleaning the surfaces of the targets. Ultra high purity argon was used as the sputtering gas, and the chamber was brought to a pressure of about 2.0 mtorr before initiation of sputtering. During the growths, the magnetrons were controlled by voltage to maintain currents that yielded slightly group-I poor films, with typical working parameters of about 50 mA and 330 V for the Ag magnetron and 130 mA and 540 V for the In magnetron. Se was supplied in overpressure to ensure that there was sufficient Se to obtain proper stoichiometry. To do this, the Se effusion cell was initially ramped up to 520°C to quickly heat the crucible and initiate evaporation, then lowered to 310°C where it was maintained for the duration of growth. At the end of growth, the Se cell remained hot long enough to ensure Se was being supplied until the sample was sufficiently cooled such that Se desorption from the film was unlikely. Growth rates were about 10-12 nm/min, and the sample thicknesses ranged from about 400-600 nm, measured by analysis of fracture cross sections by scanning electron microscope (SEM). The samples were brought through a programmed cool down to prevent film delamination from the substrates.

In order to ensure as similar growth conditions as possible for a given sample set, GaAs substrates of all four orientations used in this study were cut into thin strips and mounted next to each other on the substrate heater. This ensured that the flux received at all samples were as similar as possible, with measured compositions that were comparable in a given sample set. The sample temperatures were monitored by pyrometer, with measurements taken a few minutes after the onset of growth on each sample, as well as about half way through the growth period. It was noticed that the (111) samples were typically higher in pyrometer measured temperature than the (001) and (110) samples, often by about 20°. Switching the order in which samples were mounted had no effect, ruling out temperature fluctuations on the substrate heater or differences in heating along the clips that held the samples to the heater. It is thought that the (111) samples, which were both cut from

the same double side polished (111) wafers, may be slightly thicker than the (001) or (110) samples, which would mean the clips would hold them more securely to the substrate heater. It is also possible that they had better contact with the substrate heater due to the rear side being polished, since both (001) and (110) samples had unpolished back sides. The sample temperatures listed in the tables of data found in this thesis are those measured by pyrometer.

3.3 Analysis techniques

A variety of analysis equipment was exploited to help gain insight into the properties of the thin films grown in this study. These include observation and characterization of film morphology, study of the structure of the films and interface, obtaining the average composition of each film, as well as looking at the composition profiles through the films. These techniques are described here along with any relevant parameters used for the studies.

Preliminary study of the samples to observe their surface morphology and establish likelihood of epitaxy was performed in a Hitachi S-4700 SEM at 20 kV accelerating voltage. Fracture cross sections were also imaged with this instrument to determine film thickness and observe the interface structure. Film composition was determined in a JEOL 7000 SEM equipped with a Thermo Electron energy dispersive x-ray spectroscopy (EDS) microanalysis system using a Phi-Rho-Z correction method. An electron beam energy of 10 kV was used for EDS measurements to ensure that signal from the GaAs substrate was not contributing to the measured composition.

Topographic analysis of morphological features was performed using an Asylum Research MFP-3D atomic force microscope (AFM) in tapping mode using Si probes purchased from Ted Pella. AFM data was analyzed with use of both the Igor software and Gwyddion software [1]. Scan sizes varied from 10 μm down to 1 μm, and the scan rate was adjusted from one sample to another such that the tip could keep up with the morphological features that some of the samples, particularly those grown on (001) and (110) substrates, typically showed.

Composition profiles as a function of depth were obtained through time-of-flight secondary ion mass spectrometry (TOF-SIMS) using a Physical Electronics PHI Trift III system. A Cs ion beam sputtered a 400 μm x 400 μm square at 2 kV and 30-50 nA in cycles along with an Au liquid metal ion gun used for analysis of a 50 μm x 50 μm region at 22 kV and 2-7 nA, with the analysis spot centered within the larger square to ensure as flat an area as possible for the analysis, which improves the depth resolution. Sputtering and analysis cycles lasted 10 sec and 32 sec, respectively, and masses analyzed ranged from 0 to 800 amu. Samples were sputtered until film signals dropped off and substrate signals stabilized. The craters were measured by Dektak profilometer to determine the sputtering depth and rate.

Film structure was studied by x-ray diffraction using a Philips X'pert MR system using Cu K_α (λ=0.154056 nm) x-rays. Survey 2θ scans were performed on the films covering 2θ=20-105° and more detailed scans were taken around the highest intensity substrate and film peaks observed in the survey scans, with a step size of 0.005°. Analysis of the XRD data, including peak identification and fitting, was performed using MDI Jade software. The PDF+4 database from the International Center for Diffraction Data was utilized to find powder diffraction files with which to compare the acquired data to confirm the identity and structure of the films.

The film and interface properties were also studied using transmission electron microscopy (TEM). A cross section sample was prepared by in-situ lift-out method using an FEI Helios Nanolab 600i focused ion beam, with a final cleaning step using 15 pA and 1 kV to remove a damaged amorphous layer at the surface. High resolution TEM images and selected area diffraction patterns were acquired in a JEOL 2010 LaB_6 TEM. To study the composition of the film and interface region, scanning transmission electron microscope energy dispersive x-ray spectroscopy (STEM-EDS) line and spot mode data were acquired in a JEOL 2010F TEM equipped with an Oxford EDS detector. The sample was tilted intentionally at the interface to get clear lattice fringe

images of both the AIS film and GaAs substrate to make sure that they did not overlap prior to acquisition of EDS, to ensure as sharp as possible an interface. The Gatan Digital Micrograph program was used for analysis of images and electron diffraction pattern.

3.4 Scanning tunneling microscope

Scanning tunneling microscopy (STM) measurements were carried out in a custom built system within a three chamber ultra high vacuum system[2]. Systems of this design show extremely low drift, as low as 1 Å per hour in all three spacial directions. The system's three chambers are separated by gate valves, and consist of a turbomolecular pumped entry lock, where samples are initially introduced into the system, a preparation chamber equipped with a dipstick equipped for direct and indirect sample heating, and an analysis chamber where the scanning tunneling microscope is located. The analysis chamber has a base pressure of $9x10^{-11}$ torr that is maintained by ion pumps and titanium sublimation pumps.

Samples were prepared for analysis in the STM by transferring to the STM lab immediately upon venting the deposition chamber after growth. The chamber was vented with ultra-high purity N_2 and the sample immediately removed upon reaching atmosphere and sealed in a plastic bag filled with N_2. The sample was transferred to the STM laboratory in another building, where it was mounted in the STM sample holder in atmosphere and loaded as quickly as possible into the entry lock of the STM chamber. The sample experienced an estimated less than 20 minutes of air exposure. While even that amount of exposure can be enough to form a native oxide on some surfaces, analysis of other samples that experienced a similar amount of exposure showed little to no oxygen presence by x-ray photoelectron spectroscopy measurements. Once the entry lock reached $5x10^{-8}$ torr, the sample was transferred to a preparation chamber where it was heated to about 100°C

for a few hours in order to remove any water molecules that may have adsorbed to the surface during atmosphere exposure.

STM analysis was carried out at room temperature using electrochemically etched W tips. The instrument is configured such that the sample is biased relative to a grounded tip, so biases reported in this study are sample biases. Constant current mode was used throughout this work, in which a current set point is selected, and the tip height responds to changes in the tunneling current due to topographic features or changes in the local density of states as it moves across the surface, moving toward or away from the sample in order to maintain the set point current for a given sample bias. A variety of tunneling current and sample bias conditions were attempted, but it became apparent that positive biases between 2 - 3 V and currents from about 0.1 – 1 nA provided the best imaging conditions. In fact, when good imaging conditions were obtained, switching to a negative bias caused resolution to significantly degrade.

Scanning tunneling spectroscopy (STS) data were obtained by stopping the tip at predefined locations within a scan, shutting off the feedback loop that controls the tip height, and sweeping the sample bias over a range while measuring the tunneling current. A range of -2 V to +2 V was sufficient in this study to observe the band edges and gap region. Each current-voltage (I-V) point consisted of 1000 points within the voltage range, and the I-V curves were treated with light Gaussian smoothing within the acquisition program that allowed features less than the thermal energy at room temperature to be removed, while maintaining the shape of the data. STS was carried out in variable height mode, in which the tip moves inward linearly during the course of an I-V sweep, with the tip nearest the sample at 0 V, continuing a linear return to the initial height by the end of the sweep. This mode increases the signal at the band edges in semiconductors, enhancing the band edge resolution [3]. In this study the height change was set to 2 Å, and the software that controls the instrument and acquires the data corrects it for the height sweep.

In addition to the software written by J. Lyding to take measurements and analyze and export data, much of the image processing and additional analysis was done using Gwyddion software [1].

3.5 References

[1] D. Nečas and P. Klapetek, "Gwyddion: an open-source software for SPM data analysis," *Cent. Eur. J. Phys.*, vol. 10, no. 1, pp. 181–188, 2012.

[2] J. W. Lyding, S. Skala, J. S. Hubacek, R. Brockenbrough, G. Gammie, and J. W, "Variabletemperature scanning tunneling microscope," *Rev. Sci. Instrum.*, vol. 59, pp. 1897–1902, 1988.

[3] P. Martensson and R. M. Feenstra, "Geometric and electronic structure of antimony on the GaAs(110) surface studied by scanning tunneling microscopy," *Phys. Rev. B*, vol. 39, no. 11, pp. 7744–7753, 1989.

3.6 Figures

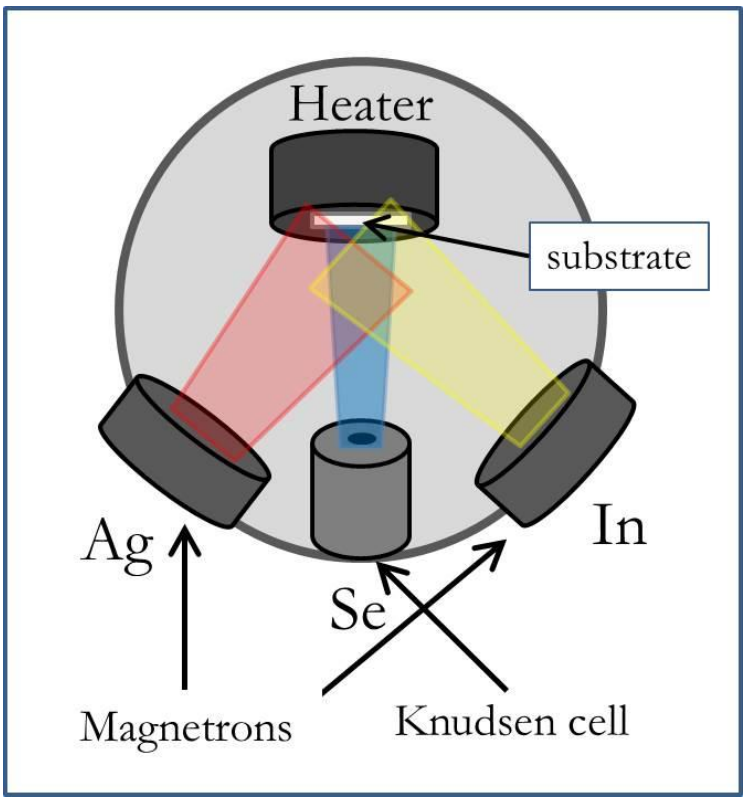

Figure 3.1 Schematic that illustrates the configuration of the sources and sample within the hybrid growth chamber, which include two magnetrons and a Knudsen effusion cell for this study.

CHAPTER 4

SURFACE MORPHOLOGY

4.1 Introduction

The epitaxial growth of $AgInSe_2$ (AIS) on GaAs is studied as a function of temperature and growth direction to discern the effect of these parameters on the morphology. Study of the morphology of epitaxial films yield a wealth of information about what is happening during growth like adatom diffusion and the surface energetics. Findings from this study that are discussed here include discovering the lowest energy surface of AIS, establishing trends in growth dynamics as a function of temperature, and discussion of the differences between AIS and related $CuInSe_2$ (CIS).

4.2 Results and discussion

AIS films were grown epitaxially on GaAs substrates polished to (001), (110), and both the cation and anion terminated (111) at a range of temperatures in order to discern how growth temperature and direction affect the growth and thus the resulting morphology of the film. All films were studied by scanning electron microscope (SEM) and energy dispersive x-ray spectroscopy (EDS) to determine the morphology and composition. The films highlighted in the analysis of this chapter are listed in Table 4.1, which lists the orientations, growth temperatures, and compositions of the films.

4.2.1 Morphology as a function of orientation

The AIS film surface morphology was found to exhibit a strong dependence on orientation, as can be seen in the AFM images in Fig. 4.1. The films grown on (100) GaAs have a morphology consisting of rectangular features, with two-sided, triangular or trapezoidal facets (Fig. 4.1a). Both polarities of (111) GaAs substrates yield films that are relatively flat with mesas that vary from simple triangles to hexagons or more complicated shapes (Fig. 4.1 b and c). There is no obvious difference in morphology between the two polarities. The films on (110) GaAs exhibit elongated

features (Fig. 4.1d) that have also been observed on CIGS [1]. The large difference in the scale of surface features from one orientation to another is illustrated in Fig. 4.2, where line topographs from each of the films in Fig. 4.1 are plotted together with the same height scale. The line profiles allow one to measure the angle between the two planes of the facets on films, and for those grown on (100) and (110) GaAs this measured angle is consistent with facets being (112)-type planes. This preference for (112) planes existing even for films grown on non-polar (110) GaAs, which would be expected to yield a non-polar AIS surface, provides significant credibility to the conclusion that the (112) planes must be lowest in energy. The formation of the (112) facets on the AIS films on (110) GaAs, represent an increase in surface area of about 25% compared to the formation of (220) AIS planes, which gives an idea of how much lower in energy the (112) close packed planes must be than the (220) to make them so preferable. These results seem to contradict recent *ab-initio* calculations that predict that the (110) surface of AIS should be lowest in energy [2]. This preference to (112) planes has been observed in epitaxial growth of $CuInSe_2$ on GaAs as well [1], though there are differences between the scale of morphological features between the two materials. For example, (200) oriented CIS growth results in elongated ripples with the occasional square pit, while for (200) oriented AIS, square and rectangular pits cover the surface entirely. The homologous temperatures during growth (ratio of the growth temperature to the melting temperature) were higher in this study than for the CIS studies, which may result in higher surface adatom mobilities. This could contribute to roughening. The results also suggest a higher (100) surface energy and a smaller difference in the two polar (112) surface energies for AIS compared to those for CIS.

The (112)-oriented AIS films (Fig. 4.1 b and c) have flat terraces with irregular edges, compared to the case of CIS on which the terrace edges are very straight [3]. In the scanning tunneling microscopy (STM) results that will be detailed in Chapter 6, it will be shown that at the atomic scale terrace edges meander, with numerous kinks and protrusions visible [4]. Thus, the step

morphology indicates that the step kink energy is low compared to CIS. While the islands on CIS are almost exclusively triangles; on AIS, triangles are only one of many island shapes that form. The absence of any obvious difference in step morphology for the cation- and anion-terminated (112) surfaces and the absence of strongly triangular features suggests that the step kink energies are not sensitive to surface termination. There are four surface step types, ignoring the pattern of cations on the $(112)_A$ surface. On the cation-terminated surface the step edge cations bond downward to a row of exposed anions that have dangling bonds reaching out from the step edge, oriented such that there are either one or two dangling bonds per step atom. On the anion-terminated surface the situation is the same except that the cations and anions are reversed. The presence of a large number of step kinks and the convolution of the step edges, combined with the rougher surfaces overall, indicate that the energies of these four steps are relatively similar, possibly due to a step-edge reconstruction.

Fig. 4.3 shows an amplitude AFM image of a sample of AIS grown on GaAs(110) at 700°C. Unlike the large mesas on (112)-oriented surfaces, these facets appear to have more prominent triangular features. The angle between the facets matches and their orientation on the surface shows that these are the $(112)_A$ and $(112)_B$ faces. As with CIS, a roughness difference is observed between the two facets when grown on GaAs (110) [1]. For AIS, the difference between the morphology of the two coexisting faces is much less obvious than for CIS. However, close examinations shows that one of the sets of facets is smoother than the other. On the rough facets the triangular mesas on the facets point from the base of the facet to its peak while on the smooth facets this is reversed. This implies that the steps on both types of facets are similar geometry. In analogy to the interpretation of CIS growth, it is expected that the smoother facets are the $(112)_A$ and the rougher facets are the $(112)_B$, and that when both facets are present adjacent to each other that surface steps

nucleate and grow primarily on the $(112)_B$ surface [1]. These facets are exploited to help elucidate the effect of substrate temperature on adatom diffusion behavior.

4.2.2 Morphology as a function of temperature

Changes in morphology as a function of growth temperature were easiest to observe and quantify for films grown on (110) GaAs. Fig. 4.4 shows two AFM topographic images of AIS films grown at substrate temperatures of 584°C (Fig 4.4a) and 700°C (Fig. 4.4b), (110) samples from sets 1 and 8 listed in Table 4.1. The size and roughness of the features changes significantly between the two films. Line topographs of each of these samples are included in the figure (4.4c). Over the profile length of 2 μm, there are about twice as many corrugations in the profile for the film grown at 700°C compared to the 584°C growth. Even though the corrugations are shrinking in spacing at higher temperature they are also becoming smoother, as discussed below. Fig. 4.5 shows a plot of the average size of the corrugations, defined as the length required follow the "uphill" and "downhill" portions of a given corrugation and calculated by counting facets along a profile in a given length and dividing to get an average corrugation size, as a function of growth temperature. The data shows a linear decrease in average corrugation size with increasing temperature.

As growth temperature increases, the roughness on the facet faces decreases. For example, the higher temperature film in Fig 4.4 shows clearly defined facets with large regions that show few clear steps. The facets are much rougher on the lower temperature growth. Evidently the mobility of adatoms is the limiting factor in growth at lower temperatures, such that nucleation of steps on a facet occurs faster than facet growth, leading to rougher facets.

Figure 4.6 shows 0.5x0.5 μm^2 size sections of AFM amplitude images, ordered in descending substrate temperature, that are centered at a corrugation to show the detail of the two sides of the corrugation. For the two highest temperature films, the roughness is similar on both facets. For the remaining three, the right side is very heavily stepped to the point that there is little flat facet to be

seen, while the left side still shows reasonably wide terraces. This indicates that there may be a higher tendency to nucleate steps on one facet while the other tends toward terrace growth. This may be leading to the difference in corrugation width observed in this study. If one side of the facets grows terraces faster, one side of the corrugation could be growing faster than the other and cause two smaller corrugations to coalesce into one larger corrugation. At a higher temperature, if the growth rate of both facets is of similar order, all corrugations will grow and result in more corrugations being visible.

Analyzing the slopes of the facet faces presents a good way of quantifying the roughness of the facets, because a higher step density will cause the apparent slope of the facet to deviate from the expected slope for what one would expect to be a (112) plane. For the slope analysis, eight height profiles were taken from AFM topographs of five films grown between 700°C and 584°C, including those shown in Fig. 4.4 and three others. The profiles were aligned such that they were perpendicular to the corrugations. The differential surface slope was computed at each point along the topograph. A histogram was constructed from the resulting slopes from all eight topographs and examined to see how the slope distribution changed with temperature. Both the positive and negative slopes (uphill and downhill along the topograph line) were studied, since these would presumably correspond to different terminations of (112) planes and may not be affected in the same way by growth temperature. All topographs were aligned for this analysis such that slopes on the smoother side of the corrugation were positive slopes. Fig. 4.7 shows the distribution of slopes as a function of growth temperature. Each point is a bin from the histogram with a width of 0.05. The histogram bin for zero slope implies a (220)/(204) surface while slopes of ± 0.737 correspond to the two ideal, unstepped (112) facets. The distribution tends toward lower slope (approaching zero) as the growth temperature decreases.

Analysis of the slopes as a function of temperature show that the surface slopes increase as growth temperature is increased, indicating a preference for the (112) facets as expected. Lower slope indicates that additional upward steps are created as one traverses down a facet from the peak. At lower temperatures there is a marked preference for one of the two facets to be closer to the (112) and also to appear smoother in the AFM images (positive slopes in the histograms). The facets are closest to (112) for growth at 684°C, although the positive slopes at 650°C are nearly the same as at 684°C. At the highest temperature, 700°C, the two surfaces show nearly the same tendency to (112) facet orientation but the probability of finding the (112) plane slope decreased. It is concluded from these results and the other observations that as surface diffusion kinetics increases the surface becomes smoother and tends more strongly to (112) facets up to ~680°C, above which entropy drives surface roughening. However, the increased diffusion kinetics also makes nucleation of steps on the two (112) surface facets much more equal, resulting in the similar number of surface steps on the two facet types and smaller corrugation scales.

4.3 Conclusions

This study has analyzed AIS growth on different orientations of GaAs to understand atomic mobility on the growth surface. The morphology shows a dependence on both growth direction and temperature. The (112) A and B surfaces are the lowest energy surfaces based on the observed roughnesses and surface facet orientations. By analogy to the results for CIS, it is concluded that this is driven thermodynamically and not kinetically, implying that these are the lowest energy surface planes of AIS. The combination of decreasing feature size and smoother facet faces with increasing growth temperature indicate that thermodynamic roughening is balanced against an increase in adatom mobility with entropy-driven roughening dominating at the highest temperatures and kinetics-driven smoothening dominating at lower temperatures. A difference in roughness between (112)A and (112)B terminated facet faces has been observed, but this is significantly smaller

than reported for CIS. The structure of the surface steps indicates that the surface steps have relatively similar energies and that the step kink energies are lower for AIS than for CIS. The step and kink energies are low enough that at 700°C the surface is significantly roughening and the two surface facets are similar in roughness. This also contributes to a reduction in the scale of surface corrugations at higher temperatures.

4.4 References

[1] D. Liao and A. Rockett, "Epitaxial growth of Cu(In,Ga)Se_2 on GaAs(110)," *J. Appl. Phys.*, vol. 91, no. 4, pp. 1978–1983, 2002.

[2] A. Shigemi and T. Wada, "Surface Stabilities of Various Crystal Faces of $CuInSe_2$ and Related Compounds by First-Principles Calculation," *Jpn. J. Appl. Phys.*, vol. 51, p. 10NC22, 2012.

[3] D. Liao and A. Rockett, "The structure and morphology of (112)-oriented Cu(In,Ga)Se_2 epitaxial films," *J. Appl. Phys.*, vol. 104, no. 9, p. 094908, 2008.

[4] P. Peña Martin, A. A. Rockett, and J. Lyding, "Growth mechanism and surface atomic structure of $AgInSe_2$," *J. Vac. Sci. Technol. A*, vol. 30, p. 04D115, 2012.

4.5 Tables

Table 4.1: List of samples included in this study, with substrate orientation, growth temperature, and composition

Sample set	Substrate orientation	Growth temperature (°C)	Ga / (In+ Ga)	Ag / (In + Ga)	Ag / In
1	(1 1 0)	700	0.23	0.83	1.07
2	(1 1 0)	684	0.17	0.75	0.91
4	(1 1 0)	650	0.14	0.75	0.87
6	(0 0 1)	612	0.12	0.77	0.88
	(1 1 1)A	648	0.07	0.79	0.85
	(1 1 1)B	654	0.07	0.78	0.84
	(1 1 0)	625	0.07	0.81	0.88
8	(1 1 0)	584	0.07	0.87	0.94

4.6 Figures

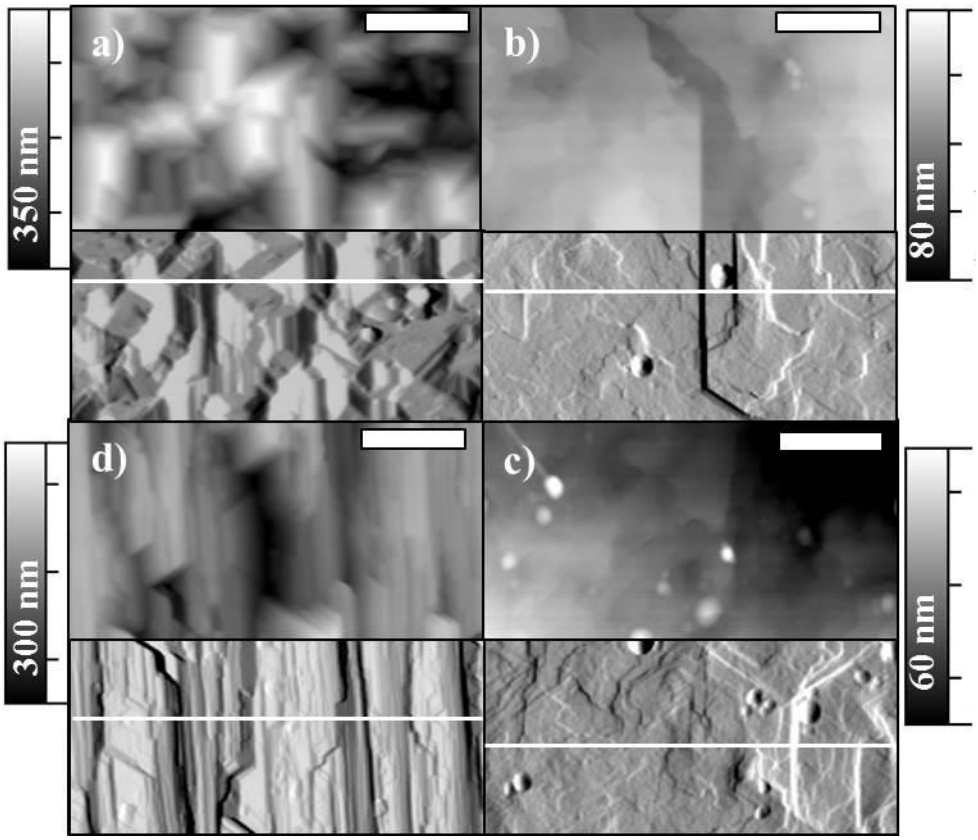

Figure 4.1 AFM topographic images, of epitaxial AIS on four orientations of GaAs: a) (100), b) (111)A, c) (111)B, and d) (110). These correspond to set 6 from table 4.1, where further details about growth conditions can be found. The scale bars are 0.5 μm. Each image shows a white line that marks where a height profile was obtained, which are plotted in Fig. 4.2. In each panel of this figure, the upper part of the image is a topographic image, with the corresponding scale bar and data range shown next to each panel. The lower half of each image is shown as the amplitude image, which shows detail of the topography.

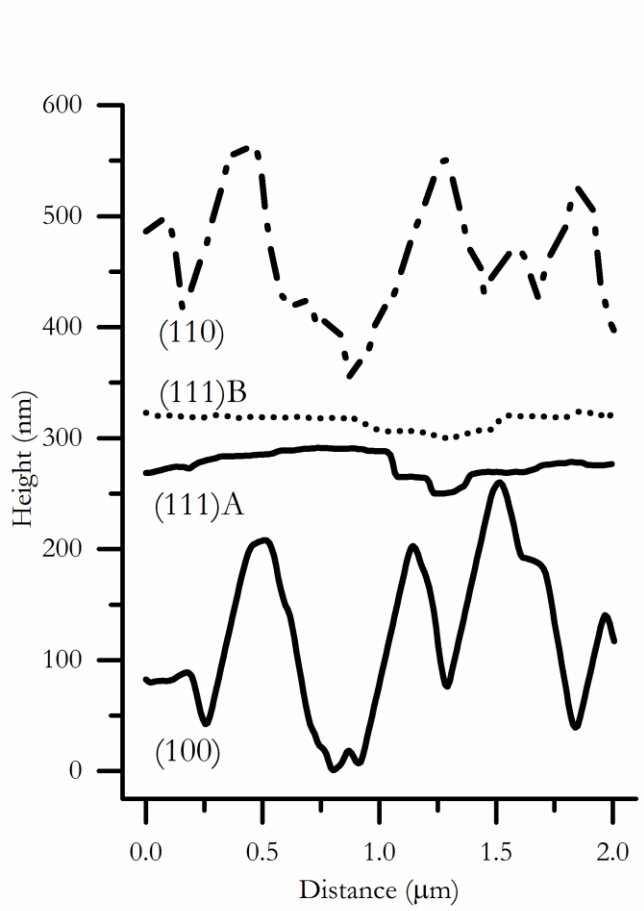

Figure 4.2: Height profiles acquired from the AFM data shown in Fig. 4.1 along the lines indicated.

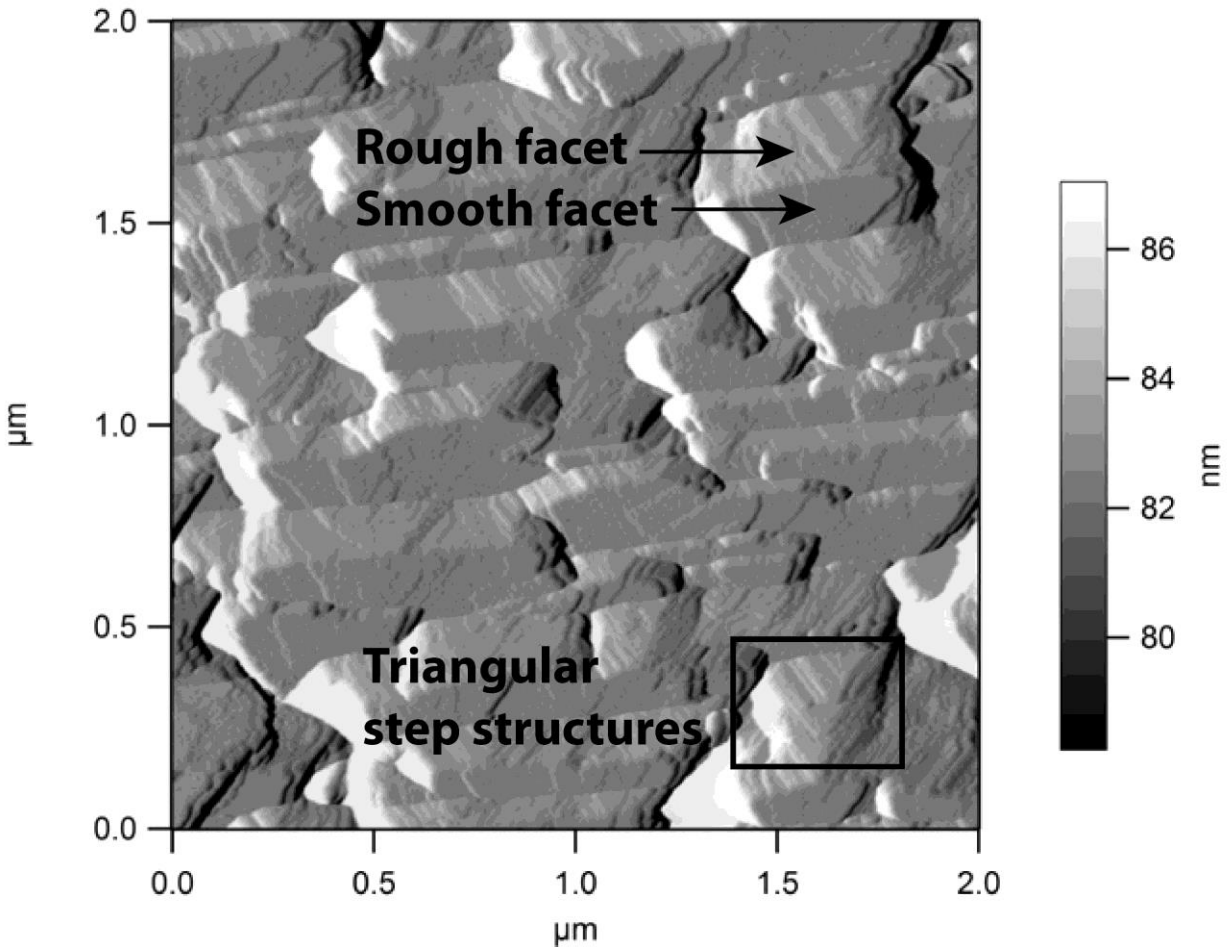

Fig. 4.3: AFM amplitude image of the AIS (220) surface that shows details of the terrace structure on the facet faces. The rough and smooth side of the facets are pointed out, and a box encloses a representative region that illustrates the presence of triangular terraces that are rather common on the facet faces for this surface. This sample corresponds to the (110) sample in set 1.

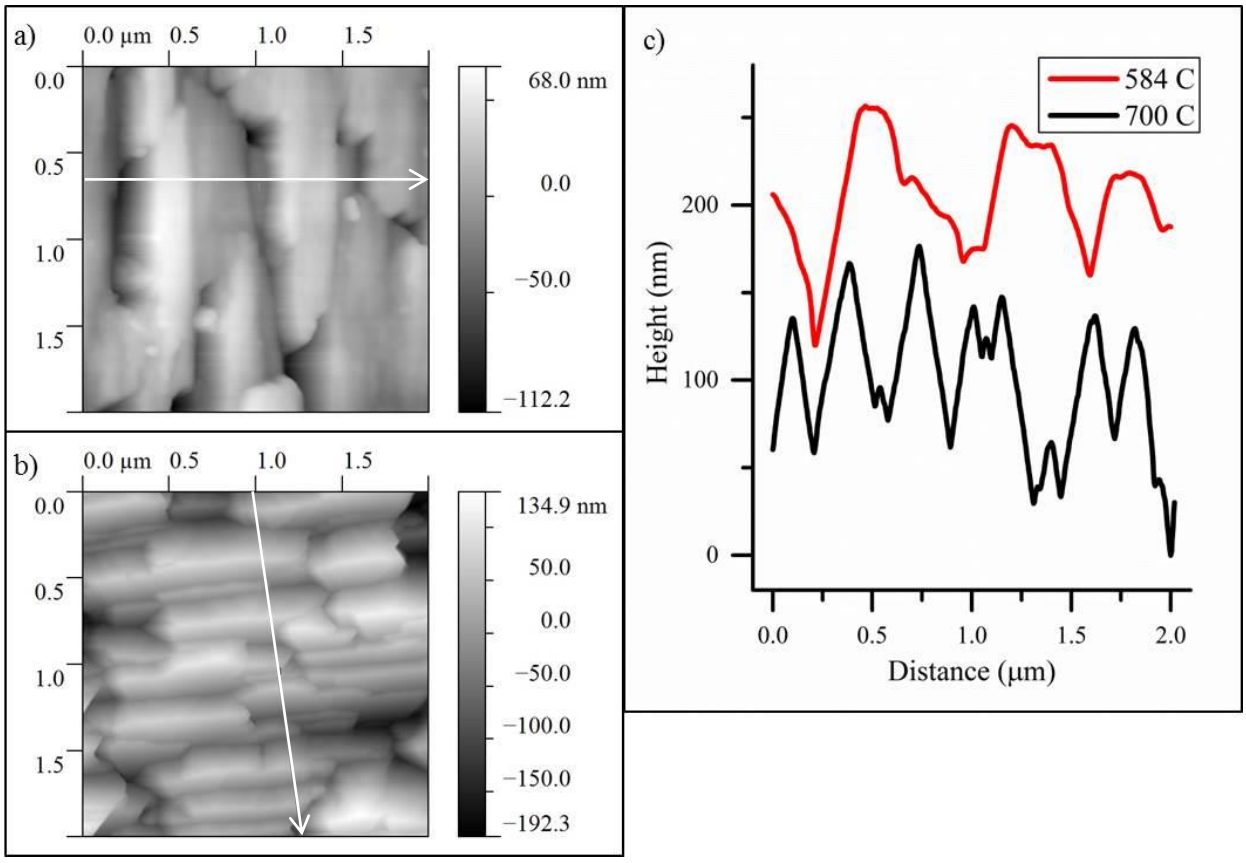

Figure 4.4: Topographic AFM scans of two samples of AIS (220) grown at substrate temperatures of a) 584°C and b) 700°C, the (110) samples from set 8 and 1, respectively. Line profiles were extracted along the arrows in the topographic scans and plotted in c).

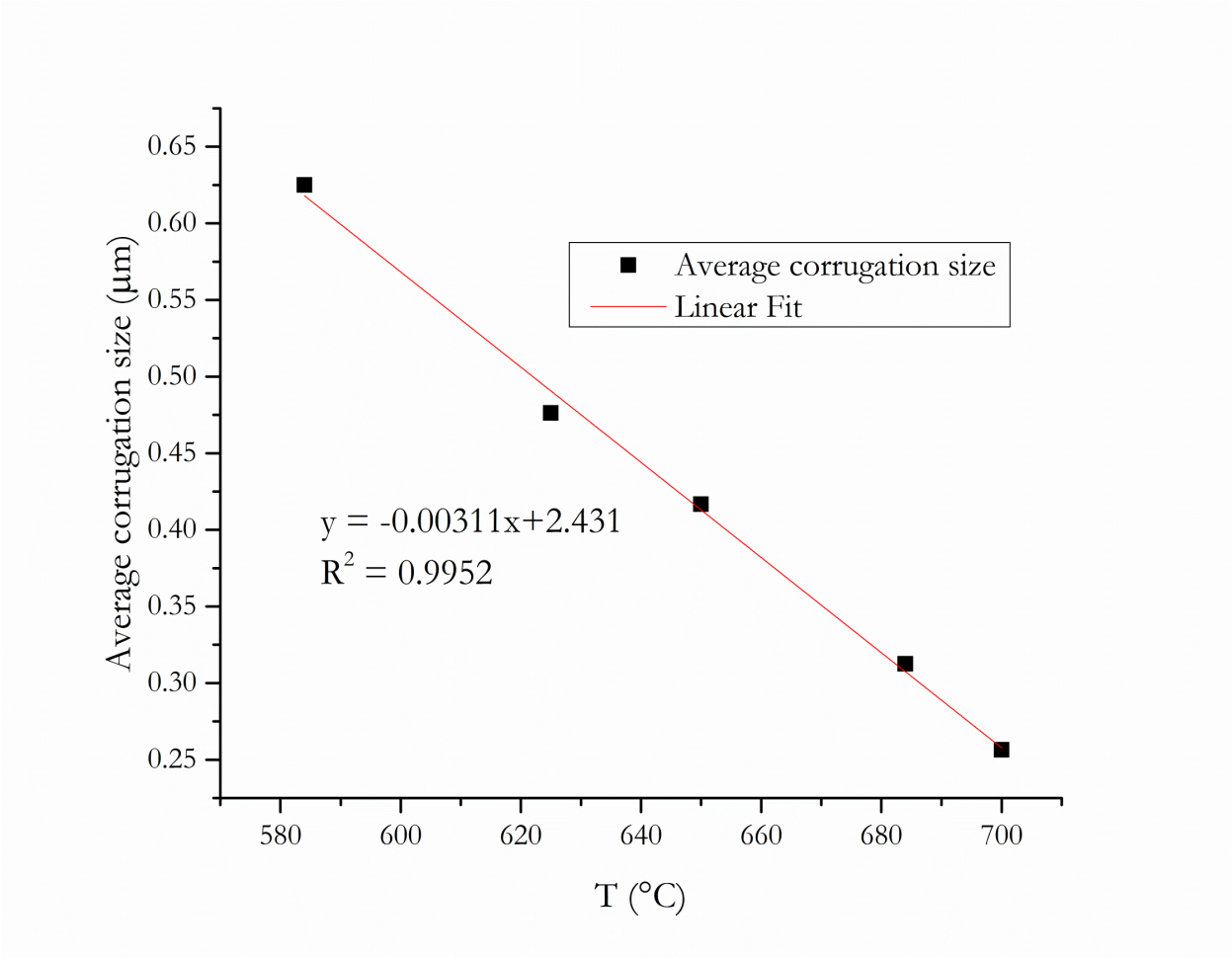

Figure 4.5: Plot of the average corrugation size on AIS(220) as a function of growth temperature. Corrugations were counted from height profiles and averaged for each sample.

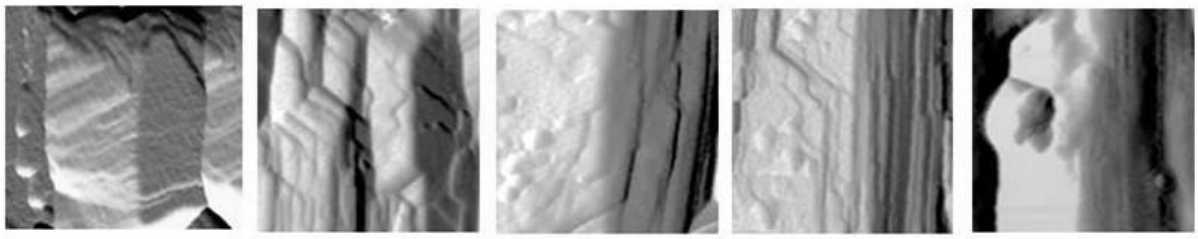

Figure 4.6: Square sections of AFM amplitude scans, 0.5µm x 0.5µm, with facets of AIS(220) arranged such that details of both sides of a given facet are in view, and rotated so that corrugations run the same direction. The samples were grown at temperatures of, from left to right, 700°C, 684°C, 650°C, 625°C, and 584°C.

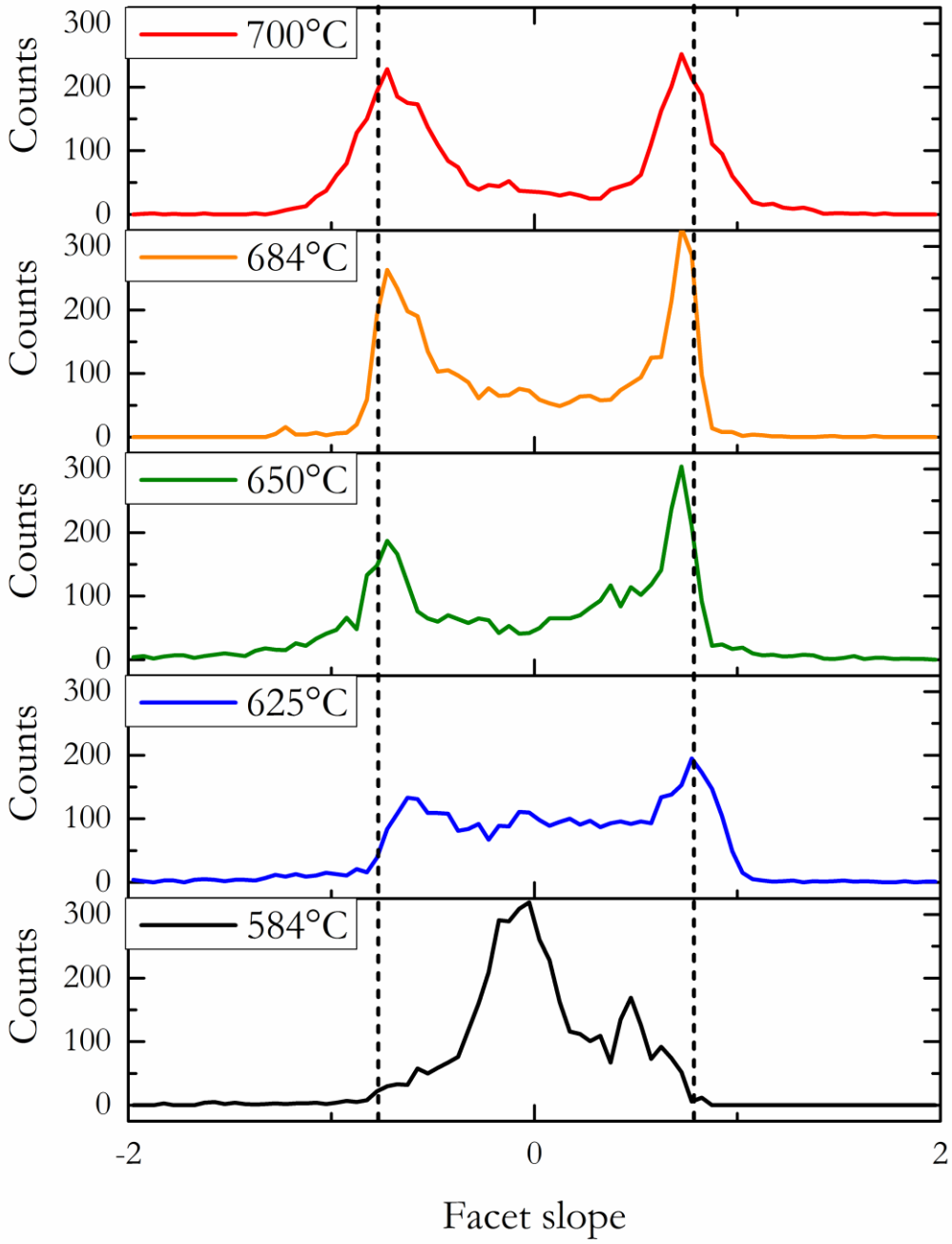

Figure 4.7: Plot of the distribution of slopes of facets as a function of growth temperature for AIS(220) films. Positive and negative refer to the uphill and downhill side of the corrugation. The slope that corresponds to a step-free (112) plane tilt from (220) is marked on both the positive and negative side by a vertical dashed line.

CHAPTER 5

FILM STRUCTURE CHARACTERIZATION

5.1 Introduction

To ensure technological relevance of AIS as a photovoltaic material, it is vital to be able to reliably deposit single phase AIS, as well as understand the roles of thermodynamics and kinetics to obtain a film that minimizes detrimental point defects and provides uniform electronic behavior. This chapter presents a study of the structure and composition of thin epitaxial films of AIS grown on GaAs in order to learn about how epitaxial growth propagates, understand critical parameters for obtaining epitaxial films, and tie these identified properties to device fabrication and operation.

Epitaxial films were grown at varying substrate temperatures to gain an understanding into how growth proceeds. Substrates of different orientations were used to help differentiate between growth directions. In chapter 4 the significant differences in morphology as a function of orientation were discussed, and this study aims to elucidate how that affects the film structure.

5.2 Results and discussion

Thin films of AIS were grown on four substrate orientations of GaAs, (100), (111)A, (111)B, and (110), over a range of temperatures as shown in Table 5.1, where sample details and results of energy dispersive x-ray spectrosopy (EDS) obtained composition measurements are reported.

First the conditions for obtaining epitaxial films were established. Samples were studied by SEM to determine at what temperature the substrate transitions from epitaxial to polycrystalline, as judged by the alignment of surface feature geometry to substrate crystallography. Fig. 5.1a-e shows SEM micrographs of five samples of AIS (001) grown at substrate temperatures from 595 to 694°C. The morphology itself has been discussed in Chapter 4, and here the focus is to determine the conditions that enable epitaxial growth. The film in Fig. 5.1e, grown at 595°C, is polycrystalline

throughout, with virtually no aligned features observable anywhere. The next higher temperature, 5.1d grown at 612°C, shows regions that are aligned similar to the higher temperature growths, but when one looks closely, there are still polycrystalline grains scattered around them, indicating that epitaxy is not complete across the surface. Increasing the temperature, Fig 5.1c, 663°C, shows no evidence of polycrystalline grains and highly aligned surface features throughout the sample. By this observation, one can estimate that at some temperature between 612° and 663° there was a transition to growing a completely epitaxial film, giving an approximate epitaxial temperature of 640°C for AIS on GaAs(001). The epitaxial temperature for AIS on GaAs(110) was determined by the same method, and Fig 5.2 shows a set of SEM images used for this determination. It was found that at substrate temperatures of 509°C, polycrystalline grains begin to appear across the surface. Below this the film was completely polycrystalline. From this, the epitaxy temperature for AIS on GaAs(110) is estimated to be approximately 550°C.

Attempts were made to find the epitaxial temperatures for AIS grown on the (111)A and B faces of GaAs, but samples did not make a transition to polycrystalline growth within the range of temperatures studied. Based on the limit of the pyrometer to accurately read the temperature, it is expected that the epitaxial temperature for AIS on GaAs(111)A and B to be ≤500°C.

The difference in epitaxial temperature among orientations is not unexpected, considering that the lattice spacings of the interface where the film and substrate meet are a function of the orientation. Previous studies have determined the epitaxial temperatures for CIS to be 640°C, 540°C, and 700°C for growth on GaAs (001), (110), and (111)B, respectively [1]. The epitaxial temperatures for the (001) and (110) orientations are remarkably close for the two materials, while the (111) substrate growths differ dramatically. For CIS, growth on (111) GaAs requires the highest temperatures of the substrates, while for AIS it is the lowest. There may be a different growth mechanism for AIS than CIS on this orientation that allows epitaxy to occur at such a low

temperature. For example, it seems likely that this implies that the atomic mobility or activation energy for surface diffusion is lower on AIS than on CIS close packed planes. It is important to note that the homologous temperature at a given growth temperature is higher for AIS than CIS because AIS has a much lower melting temperature than CIS, 780°C for AIS compared to 980°C for CIS [2].

While SEM images indicate epitaxy, an x-ray diffraction (XRD) study can give more quantitative measurement of the crystal structure of the film, as well as show any additional phases present at the surface or interface. In Fig. 5.3, survey θ-2θ scans are plotted for a set of samples grown side-by-side at an average substrate temperature of 700°C, with details for each sample listed in Table 5.1 under set number 2. For each sample the instrument was aligned to the GaAs peak corresponding to the substrate orientation and then the survey scan collected to identify the film peaks. The survey range was from 20-105°, which made it possible to view at least two sets of reflections per orientation. The sharp narrow peaks in all survey scans in Fig. 5.3 are the substrate GaAs peaks, and film peaks are found to the left of them. The powder diffraction file (PDF) for tetragonal AIS (ICDD #04-001-4947) [3] is also included on the plot at the bottom. In all of the films, the film peaks are located at the reference locations, indicating that the films are fully relaxed and tetragonal in structure. The fact that only one the set of crystal planes is contributing to the XRD spectra indicates that the films are highly oriented epitaxial layers on each substrate. There is a small peak that is unaccounted for at 21.8° that appears in the scan on the AIS/GaAs(110) sample, which is not due to the substrate or tetragonal AIS, nor could it be identified as any potential related selenide phase.

To extract more information about the AIS film through study of its diffraction peaks, more detailed scans were obtained in regions that encompass the film and substrate peak for the highest intensity reflection. For the films on GaAs(001) this is the range of 57-74° to include the AIS(400)

and GaAs(400) peaks; for GaAs(111), 24-40° was used to include the AIS(112) and GaAs(111) peaks; and (110)GaAs, 34-53° includes GaAs(220) and AIS (220) and (204) peaks; all taken with a step size of 0.005°. Note that for AIS, unlike CIS, the (220) and (204) peaks are distinct, which is due to the tetragonal distortion in the AIS crystal, resulting in a ratio of the c axis to the a axes differing from 2. For CIS and AIS these values are 2.01 and 1.92, respectively, calculated using lattice parameter data from literature [2], so the CIS (220) and (204) planes are nearly equivalent while for AIS, the *c*-axis component of the (204) planes is shifted with respect to the (220).

A representative set of detailed scans is shown in Fig. 5.4a-d, from the same sample from which the data in Fig. 5.3 was obtained. After background subtraction, the peaks were fit with Pseudo-Voigt or Pearson-VII solutions to Scherrer's equation, depending on which simulated the data most accurately, in order to deconvolute the film and substrate peaks, since there is considerable overlap. From the fit, one obtains the peak position and full width at half maximum, from which the interplanar spacings, hence lattice parameters, can be calculated. In addition this determines the coherent domain size in the film, a measure that quantifies the size scale over which changes in the crystal structure occur, which could be due to rotations within the structure of the film or misfit dislocations at the interface.

Fig. 5.5 shows the measured lattice parameters as a function of substrate temperature. Obtaining *a* from the (400) or (220) peaks is straightforward. The *c*/*a* ratio was determined from the (220)/(204) peak positions. The lattice parameters did not show a significant change with growth temperature, as shown in Fig. 5.6. The average *a* value was 0.610 nm and the average *c* was 1.162 nm, which gives a *c*/*a* ratio of 1.90; close to literature value of 1.92. While the tetragonal distortion could be different depending on the substrate since the lattice spacings are surface orientation

dependent, this thesis assumes the literature value of tetragonal distortion to compute *a* for the (112) orientations.

Fig. 5.5 shows a plot of lattice parameter *a* vs. substrate temperature, with *a* being calculated from the (400), (112), (112), and (220) peaks for the films grown on (100), (111)A, (111)B, and (110) GaAs, respectively. The literature accepted value of *a* is represented with a horizontal dashed line. The (100) and (110) data show little change over the temperature range studied, while the (111)A and B films both show a trend toward larger *a* with decreasing growth temperature, T. Dependence on T could be related to the Ga content of the film, which diffuses into the film during deposition. Ga was found to be present in measureable amounts as evidenced by the EDS compositions shown in Table 5.1. $AgGaSe_2$ has a smaller *a* lattice constant than AIS, so a decreasing *a* lattice parameter with an increasing amount of Ga is not surprising. However, one would expect this to be observable in the other films as well, since they have similar Ga concentrations at the given temperatures. Another more likely explanation is that there is some remaining strain in the films that distorts the lattice. At the temperature at which films are grown, the thermal expansion coefficients of the film and substrate can lead to significant deviations from the literature accepted lattice parameters for the materials. GaAs has a positive thermal expansion coefficient, so during growth the lattice parameters should be expanded compared to room temperature [4]. AIS has anomalous thermal expansion properties that are highly dependent on orientation, with a negative thermal expansion coefficient along the *a*-axis ($\alpha_\perp$) and positive changing to negative for the *c*-axis direction ($\alpha_\parallel$) at the growth temperatures in this study, with $\alpha_\perp<\alpha_\parallel$ [5], suggesting that for the lattice at growth temperature, both *a* and *c* are compressed, *a* more so, with respect to their room temperature values. Combined with the increasing lattice parameter of GaAs, these would make lattice mismatch improve at growth temperatures involved in this study, as well as lead to strain in the film upon cooling, since the AIS would presumably try to expand while the substrate contracts.

In addition to the peaks themselves, the ratio of the (220) and (204) peaks shown in Fig. 5.4d can shed light into the presence of rotated domains within the film. The peaks were fitted in Jade software and background removed in order to measure the peak intensities as accurately as possible. The PDF card for AIS predicts that the (204) peak should be about double the intensity of the (220) peak in an ideal random powder. However, the intensity ratio (204)/(220) for the peaks in Fig. 5.4d is actually 0.37, indicating that there is a strong preference toward nucleating (220) oriented domains. This could be related to the fact that lattice parameter *a* compresses at the growth temperatures.

There is also an extra peak that appears between the film and substrate peaks in (112) and (220)/(204) oriented AIS that cannot be attributed to either material. Fig. 5.6 shows two high resolution θ-2θ XRD scans of films on (111)A and B GaAs in which the film and substrate peaks are both identified, with the additional peak marked at 26.6°. Potential matches include $AgIn_5Se_8$ (112), $Ag(In_xGa_{1-x})Se_2$ (112), and zincblende $AgInSe_2$ (111) (here the zincblende phase would represent a disordered cation lattice). Previous studies indicate that, in some cases, polycrystalline AIS films show an ordered defect compound at the surface.[6], [7], [8] One such study observed the presence of an additional set of XRD peaks beyond those of the tetragonal phase in polycrystalline $Cu_xAg_{1-x}InSe_2$ when $x \leq 0.2$; these extra peaks were attributed to either $Ag_3In_5Se_9$ or $AgIn_5Se_8$ [6]. The enhancement of the extra peaks with grazing incidence measurements indicated the presence of these phases at the surface [6]. Others have used XRD as well as XPS to observe an additional surface phase on $(Cu,Ag)(In,Ga)Se_2$ films that was attributed to $AgIn_5Se_8$ [7], [8]. This was also observed for $Ag(In,Ga)Se_2$ films [7]. Angle resolved XRD was attempted on the samples in this study, but for epitaxial samples, the intensity decreases significantly with glancing angle so the lack of an observation of any increase in peak height with glancing angle is not conclusive. It is also impossible to tell from the XRD data if the peak emanates from the surface or interface of the film.

To directly observe the film and interface, a sample of AIS, from set 2 in Table 5.1 grown on (111)B GaAs, was studied by TEM in cross section. In addition to observing the film and substrate, an additional intermediate layer was found at the interface. Figure 5.7 shows a lattice image that includes the AIS film, intermediate layer, and substrate. Lattice fringes are visible throughout the image in both film and substrate. White boxes in each section of the film are expanded to show the detail better. There are also large voids, marked with the letter K, which are likely the Kirkendall voids, also observed in SEM fracture cross sections. These have been observed in AIS [9] as well as CIS [10] previously. The Kirkendall voids are observable throughout the intermediate layer. It is concluded that what is observed here is an epitaxial intermediate layer between the film and substrate, with a thickness of about 30 nm, that must be forming during the growth process. In cross section the film seemed to be very uniform until the intermediate layer.

To further study the film and interface layer, selected area diffraction patterns (SADPs) were obtained to gain insight into the local crystalline structure and interplanar spacings. Fig. 5.8a-b. Fig. 5.8a shows a SADP taken well into the AIS film, where the film mainly should be contributing to the diffraction spots. The AIS spots show up in pairs consisting of one bright and one faint spot. These are confirmed to be AIS by comparing the data to SADPs taken well into the film, where only AIS should be contributing. The bright spot is the tetragonal AIS peak and the fainter peak is due to rotational twins. The direction of rotation is about the [112] direction, as is evidenced by the direction along which the tetragonal spots are split. A high density of twins was observed in the AIS film, as is common in epitaxial chalcopyrite films.

There is an additional set of spots that are not identifiable as either AIS or GaAs present in Fig. 5.8b. The arrangement is the same as that of GaAs, but the spacing is larger, meaning it is likely from material with the same crystal structure as GaAs. A section of the SADP is enlarged in Fig. 5.9 to make it easier to see the additional spots. Measuring the spacing between the spots gives an

estimated interplanar spacing, d, of 0.339 nm. The XRD peak measured at 26.6° corresponds to an interplanar spacing of 0.335 nm, compared to the AIS (112) spacing of 0.347 nm and for GaAs(111) of 0.326 nm. To ensure that these spots are truly from the intermediate layer, the lattice spacings were measured in each image for the substrate, intermediate layer, and the AIS. The spacings were all calibrated using the known spacing for the GaAs(111) planes. A power spectrum density map was taken from a TEM lattice image, shown in Fig. 5.10 that only included the substrate and intermediate layer, and the interplanar spacing measured by this method was consistent with that measured by the diffraction spots. This seems to be good proof that the additional diffraction spots are indeed due to the intermediate layer. The fact that the diffraction spots have the same symmetry as the GaAs substrate in the SADPs indicates that the layer has the same crystalline structure with a larger lattice parameter. Point-mode nano-probe EDS was performed to obtain the composition of the layer. Results indicate that the intermediate layer contains constituents of both the film and substrate with a composition of about 30% GaAs to 70% AIS. If one assumes a linear relationship between the interplanar spacing of AIS and GaAs, this composition would yield an interplanar spacing of about 0.341 nm, consistent with the spacing in the intermediate layer found by SADP analysis.

The observation of Kirkendall voids throughout the interfacial layer indicates that the layer formed during growth and that the voids nearest the AIS layer formed earlier in growth than the ones back toward the substrate. It has been established that during epitaxial growth of CIS on GaAs, Ga diffusion into the film leads to Kirkendall voids at the interface [11]. The Ga observed in the AIS film by EDS most likely diffused into the film by a similar mechanism, leaving behind voids at the film/substrate interface. An additional reaction appears to be occurring in AIS, such that film constituents also diffuse into the substrate. The progression of the voids toward the back of the film suggests that they nucleate at the GaAs/intermediate layer interface once the intermediate layer

forms. Composition measurements by EDS and SIMS profiles confirm the presence of Ga in the AIS films, even though no Ga was intentionally added. As with CIGS, no As was detected. It is presumed that any As that enters the AIS film passes through quickly and desorbs, as has been suggested for epitaxial CIGS.

Figure 5.11 shows SIMS profiles for AIS grown on GaAs (111)B at 720°C (5.11a) and 620°C (5.11b), the (111)B samples from set 2 and 8 listed in Table 5.1. The profiles are arranged with the surface to the left and profiles are given as a function of sputter time. The approximate interface between the film and substrate is labeled in the figure. The In, Ag, and Se profiles are relatively flat throughout the film region in both the higher and lower temperature film, while the Ga profile is only flat in the high temperature film. In the lower temperature film the Ga profile is heavily sloped. The decrease in Ga counts in the GaAs compared to in the AIS is an artifact due to a significant difference in the ion yield of Ga ions between the AIS matrix and the GaAs matrix. EDS gives the true average composition of the film region, and the GaAs 50% Ga.

Ga profiles extracted from SIMS experiments were fit with an error function to extract the Ga diffusivity as a function of growth temperature. The results are shown in an Arrhenius plot in Fig. 5.12, with the data from this study denoted by squares. Diffusivity data from all orientations of film were included on one plot because it did not appear that there was a significant difference in diffusivity that could be tied to orientation. One point that was several orders of magnitude higher than the rest of the data was not included. The data shows a general trend of higher diffusivity at higher growth temperatures. A fit yields an activation energy for Ga diffusion in AIS of about 3.4 eV. To the author's knowledge there is no experimental data for diffusivity of Ga in AIS with which to compare this data, so included on the plot are diffusivity data for Ga in CIGS reported in Schroeder et al. (circles) [12] and Lei et al. (triangles) [11]. These data are within an order of magnitude of the AIS data, but are generally lower than AIS, especially at the higher temperature

side of the data. Also, of the two points shown from Schroeder's study, the lower diffusivity point is much closer to the group I to indium ratio in the AIS films, so it may be the better comparison point. It likely means that diffusivity is actually somewhat higher in AIS than CIS. Since Ga profiles are significant to device performance, maintaining a desired profile throughout processing can be a challenge. It may be more difficult to obtain a high Ga gradient in AIS than CIS. However, since AIS also shows a higher structural order than CIS at a given processing temperature, it may be possible to use lower growth temperatures for AIS and still yield a high performing device, which may offset the problem of the higher Ga diffusivity.

5.3 Conclusions

Epitaxial films of AIS have been grown on GaAs, and this information is used to help extract details about what happens during growth. The diffusivity of Ga in AIS has been established, which indicates a higher diffusivity than in CIS. The studies involved in this work did not observe an ordered defect compound at the surface as others have reported. An intermediate layer between the film and substrate indicates that epitaxial growth occurs with an intermixing between the two layers, which leads to a coherent region with a lattice parameter intermediate between the two, likely helping to mediate the large lattice mismatch.

5.4 References

[1] D. Liao and A. Rockett, "Epitaxial growth of Cu(In,Ga)Se_2 on GaAs(110)," *J. Appl. Phys.*, vol. 91, no. 4, pp. 1978–1983, 2002.

[2] J. L. Shay, B. Tell, H. M. Kasper, and L. M. Schiavone, "Electronic Structure of $AgInSe_2$ and $CuInSe_2$," *Phys. Rev. B*, vol. 7, no. 10, pp. 4485–4490, 1973.

[3] ICDD, *PDF-4+ 2010 (Database)*. Newtown Square, PA, USA: International Centre for Diffraction Data, 2010.

[4] J. Blakemore, "Semiconducting and other major properties of gallium arsenide," *J. Appl. Phys.*, vol. 53, no. 10, pp. R123–R181, 1982.

[5] N. S. Orlova and I. V. Bodnar, "The Anisotropy of the Thermal Expansion in the $AgInC_2^{VI}$ Chalcopyrite-Type Compounds from the X-Ray Diffraction Data," *Phys. Status Solidi*, vol. 101, pp. 421–425, 1987.

[6] A. R. Aquino Gonzalez, "Physical and optoelectronic properties of copper silver indium diselenide thin films," 2012.

[7] H. Simchi, B. E. Mccandless, K. Kim, J. H. Boyle, R. W. Birkmire, and W. N. Shafarman, "An Investigation of the Surface Properties of (Ag,Cu)(In,Ga)Se_2 Thin Films," *IEEE J. Photovoltaics*, vol. 2, no. 4, pp. 519–523, 2012.

[8] H. Simchi, B. E. Mccandless, K. Kim, J. H. Boyle, and W. N. Shafarman, "Effect of Rapid Thermal Processing on the structural and device properties of (Ag,Cu)(In,Ga)Se_2 thin film solar cells," *Thin Solid Films*, vol. 535, pp. 102–106, 2012.

[9] P. Peña Martin, A. A. Rockett, and J. Lyding, "Growth mechanism and surface atomic structure of $AgInSe_2$," *J. Vac. Sci. Technol. A*, vol. 30, p. 04D115, 2012.

[10] C. Lei, A. Rockett, I. M. Robertson, W. N. Shafarman, and M. Beck, "Void formation and surface energies in Cu(InGa)Se_2," *J. Appl. Phys.*, vol. 100, no. 7, p. 073518, 2006.

[11] C. H. Lei, a. a. Rockett, I. M. Robertson, N. Papathanasiou, and S. Siebentritt, "Interface reactions and Kirkendall voids in metal organic vapor-phase epitaxy grown Cu(In,Ga)Se_2 thin films on GaAs," *J. Appl. Phys.*, vol. 100, no. 11, p. 114915, 2006.

[12] D. J. Schroeder, G. D. Berry, and A. A. Rockett, "Gallium diffusion and diffusivity in $CuInSe_2$ epitaxial layers," vol. 69, no. October, 1996.

5.5 Tables

Table 5.1: List of samples grown on GaAs(001) substrates, with relevant growth parameters and composition information obtained by EDS.

Sample set	Substrate orientation	Growth temperature (°C)	Ga / (In+ Ga)	Ag / (In + Ga)	Ag / In		Sample set	Substrate orientation	Growth temperature (°C)	Ga / (In+ Ga)	Ag / (In + Ga)	Ag / In
1	(0 0 1)	674	0.20	0.78	0.97		6	(0 0 1)	612	0.12	0.77	0.88
	(1 1 1)A	739	0.25	0.84	1.12			(1 1 1)A	648	0.07	0.79	0.85
	(1 1 1)B	739	0.23	0.82	1.06			(1 1 1)B	654	0.07	0.78	0.84
	(1 1 0)	700	0.23	0.83	1.07			(1 1 0)	625	0.07	0.81	0.88
2	(0 0 1)	687	0.16	0.75	0.90		7	(0 0 1)	595	0.07	0.78	0.84
	(1 1 1)A	721	0.13	0.82	0.94			(1 1 1)A	628	0.02	0.86	0.88
	(1 1 1)B	718	0.17	0.80	0.96			(1 1 1)B	640	0.04	0.84	0.88
	(1 1 0)	684	0.17	0.75	0.91			(1 1 0)	599	0.04	0.91	0.91
3	(0 0 1)	694	0.18	0.77	0.93		8	(0 0 1)	591	0.03	0.89	0.92
	(1 1 1)A	715	0.14	0.84	0.97			(1 1 1)A	619	0.10	0.83	0.92
	(1 1 1)B	720	0.13	0.87	1.00			(1 1 1)B	617	0.04	0.88	0.92
	(1 1 0)	687	0.16	0.82	0.97			(1 1 0)	584	0.01	0.90	0.90
4	(0 0 1)	678	0.19	0.78	0.96		9	(1 1 1)A	549	0.01	0.86	0.87
	(1 1 1)A	698	0.13	0.76	0.88			(1 1 1)B	533	0.03	0.84	0.87
	(1 1 1)B	688	0.12	0.78	0.89			(1 1 0)	509	0.02	0.75	0.76
	(1 1 0)	650	0.14	0.75	0.87		10	(1 1 1)A	539	0.00	0.81	0.81
5	(0 0 1)	663	0.18	0.83	1.01			(1 1 1)B	548	0.00	0.79	0.79
	(1 1 1)A	684	0.09	0.81	0.89			(1 1 0)	477	0.04	0.77	0.80
	(1 1 1)B	681	0.06	0.82	0.87							
	(1 1 0)	684	0.09	0.77	0.85							

5.6 Figures

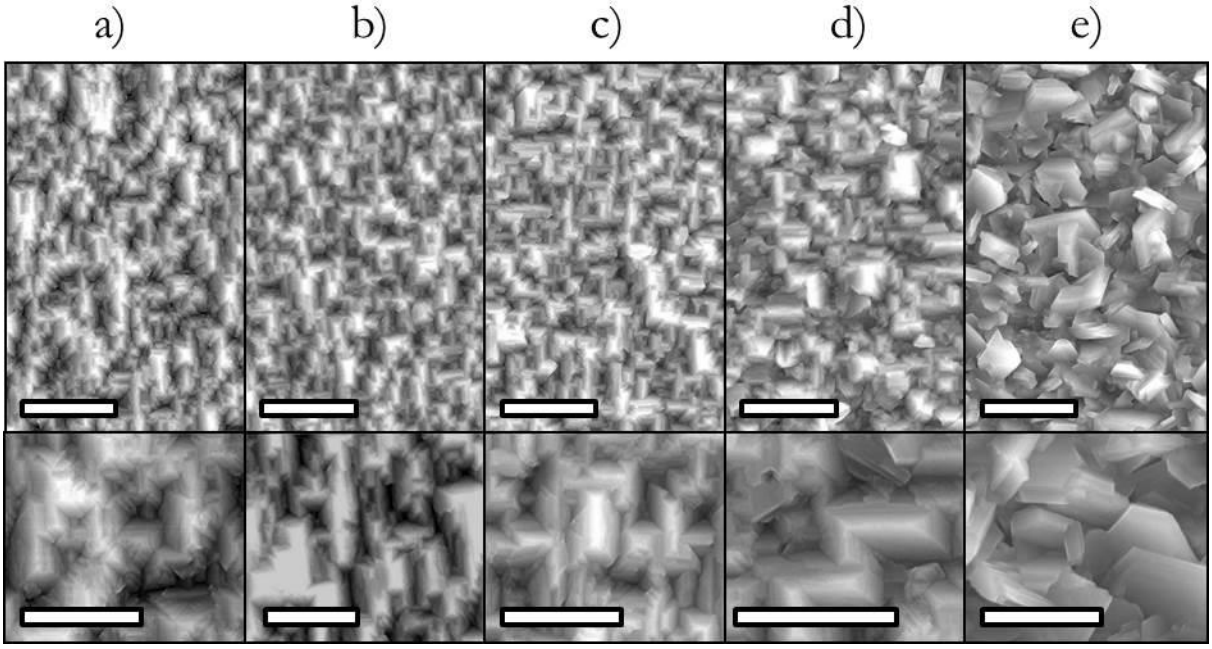

Figure 5.1: SEM micrographs of the surface of AIS grown on GaAs(001) at substrate temperatures of 694°C (a), 678°C (b), 663°C (c), 612°C (d), and 595°C (e). The samples correspond to the films grown on (001) substrate in sets 3, 4, 5, 6, and 7, respectively, from Table 5.1. The upper images have a scale bar width of 2 μm and the lower insets have a scale bar of 1 μm.

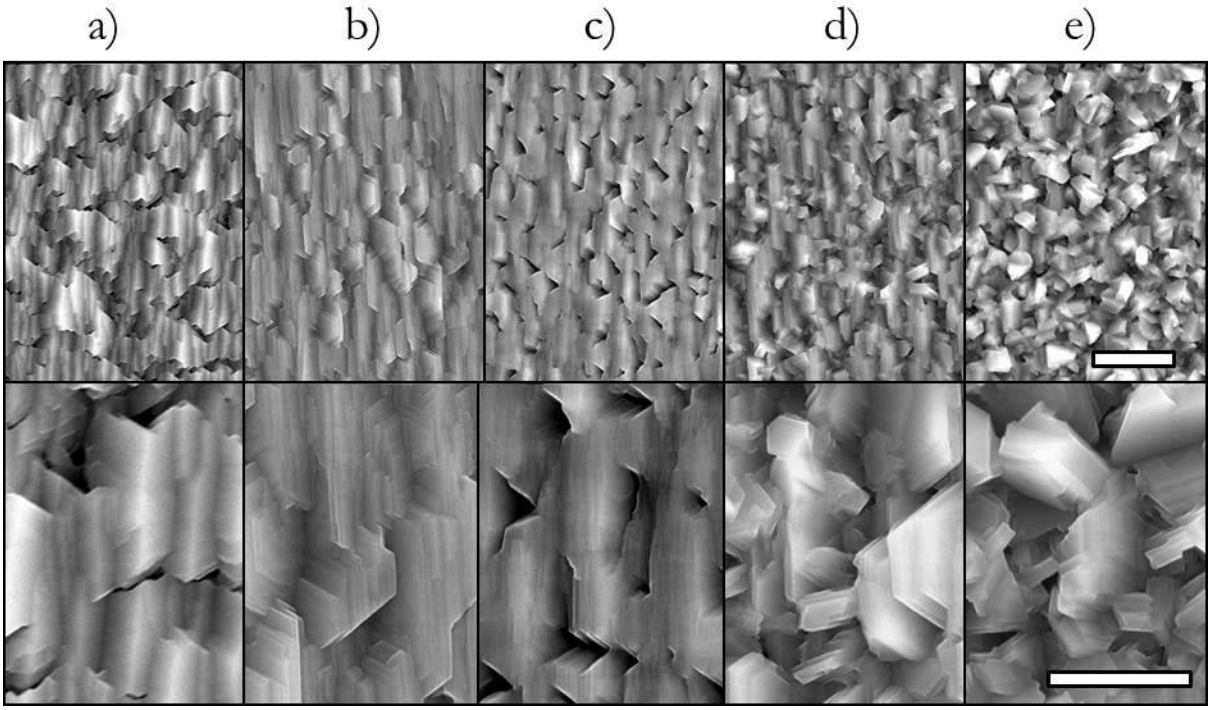

Figure 5.2: SEM micrographs of the surface of AIS grown on GaAs(110) at substrate temperatures of 700°C (a), 625°C (b), 584°C (c), 509°C (d), and 477°C (e). The samples correspond to the films grown on (110) substrates in sets 1, 6, 8, 9, and 10, respectively, from Table 5.1. The upper images have a scale bar width of 2 μm and the lower insets have a scale bar of 1 μm.

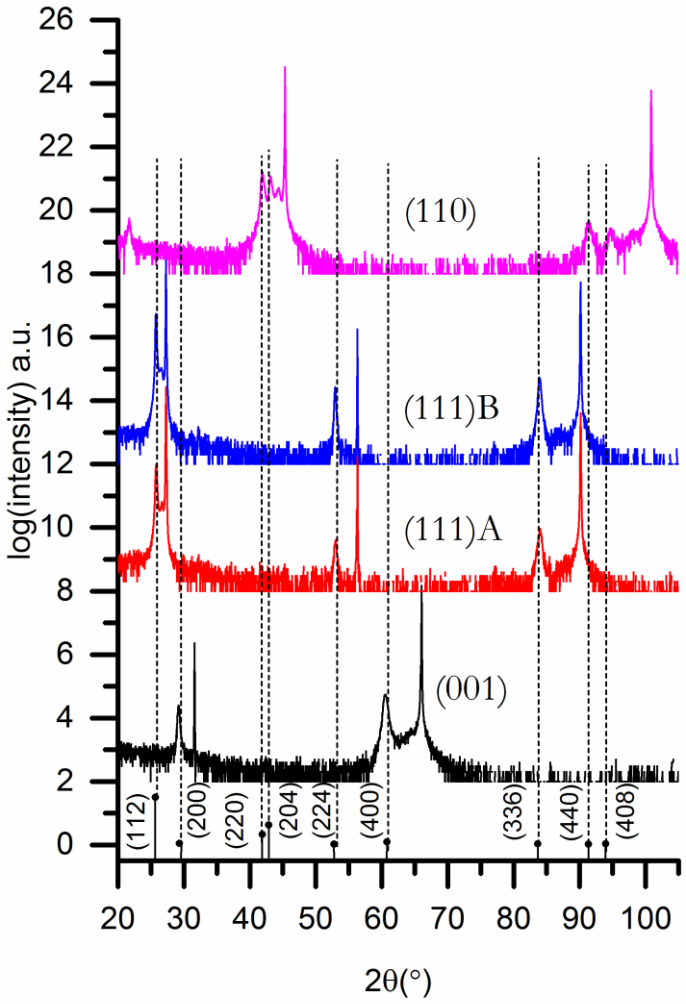

Figure 5.3: X-ray diffraction survey 2θ scan for AIS samples that correspond to samples set 2 from Table 5.1. Powder diffraction file #04-001-4947 [3] for tetragonal $AgInSe_2$ is shown for reference.

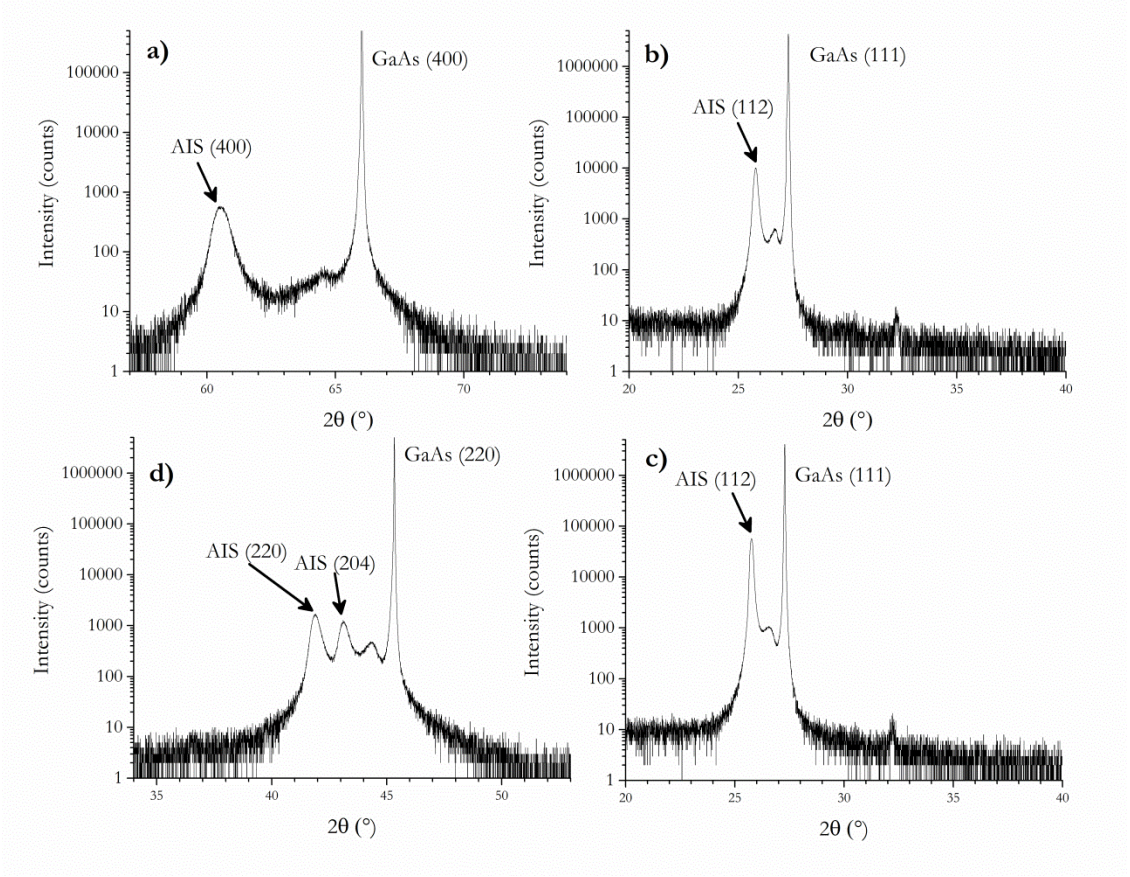

Figure 5.4: X-ray diffraction detailed scans obtained near the highest intensity reflection for the films shown in Fig. 5.3. The samples were grown on GaAs(001), GaAs(111)A, GaAs(111)B, and GaAs(110) shown in panel a), b), c), and d), respectively.

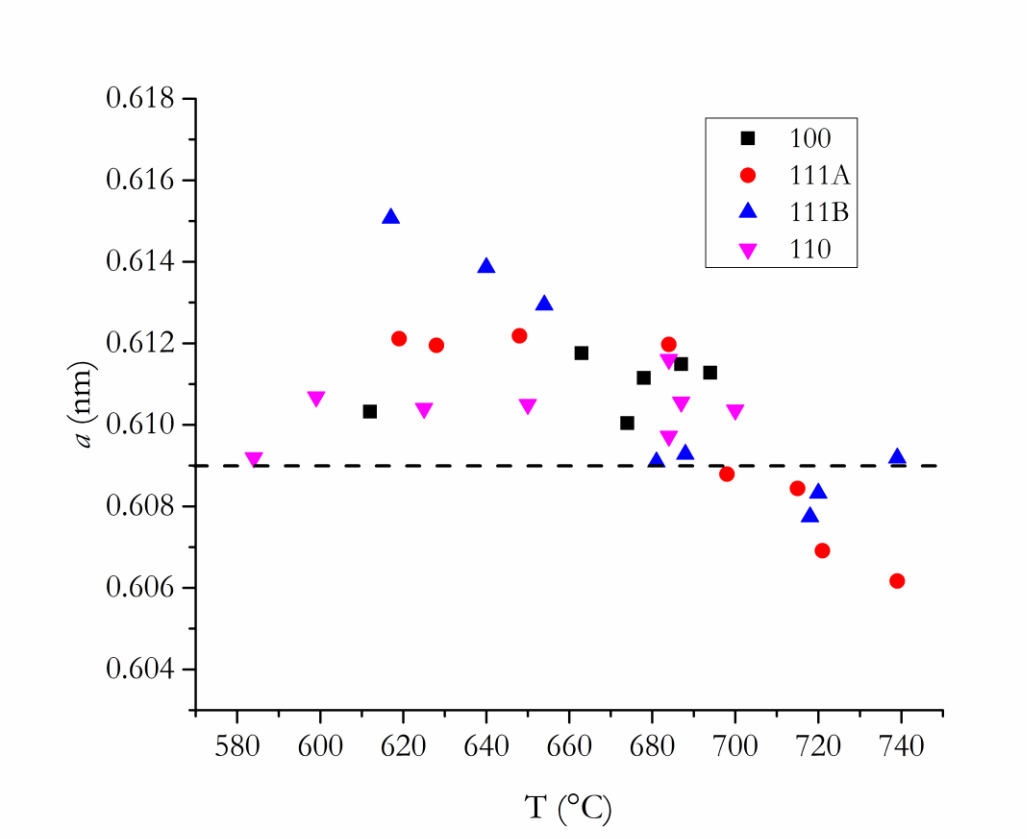

Figure 5.5: Lattice parameter *a* as a function of substrate temperature for films grown on (100), (111)A, (111)B, and (110) AIS. The (400) peak, (112), (112), and (220) peaks, for the (100), (111)A, (111)B, and (110) substrate films, were used to compute *a*, respectively.

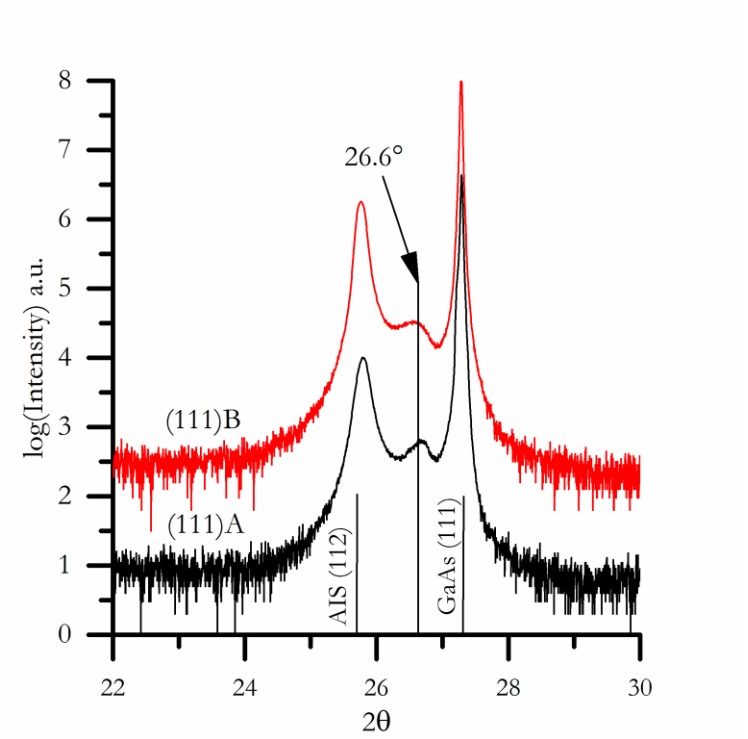

Figure 5.6: X-ray diffraction 2θ scans for AIS films grown on (111)A (black) and (111)B (red) substrates. The AIS (112) peak and GaAs(111) peaks are both labeled, and a third peak is identified in between at 26.6º.

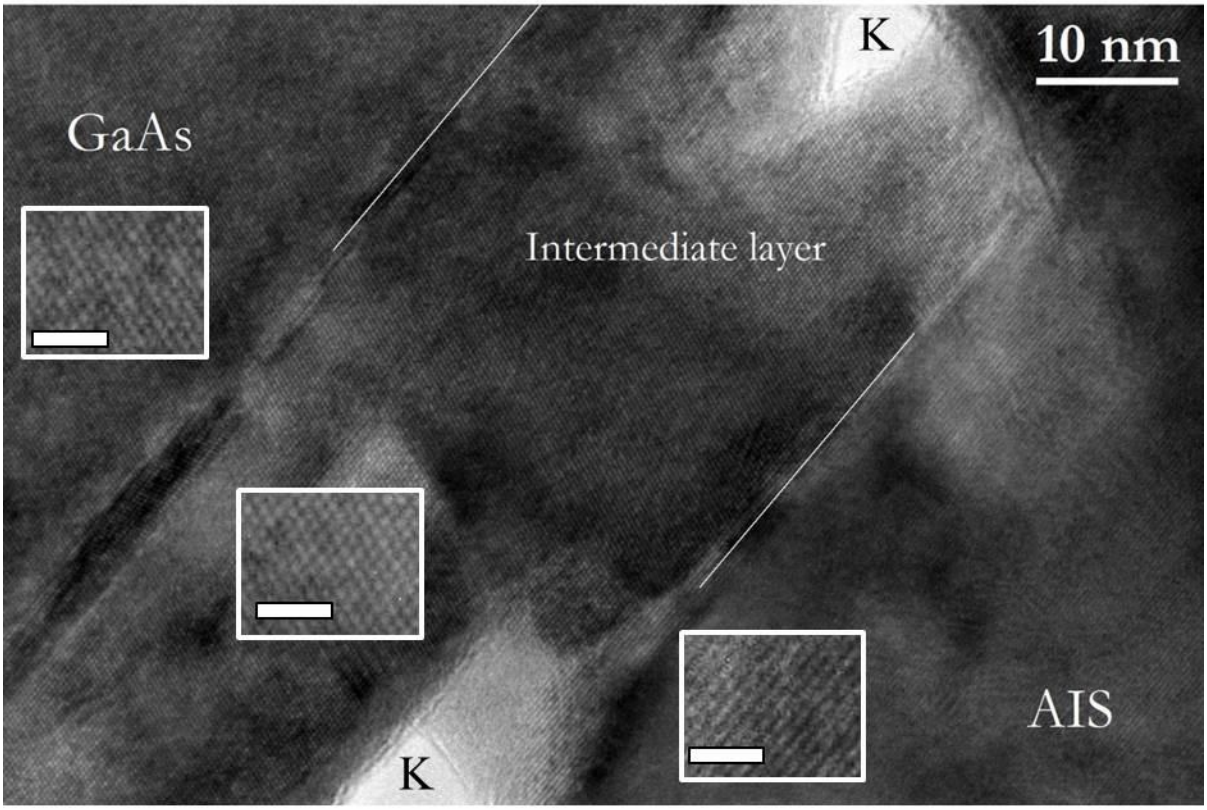

Figure 5.7: Transmission electron micrograph of a cross section of AIS grown on (111)B GaAs showing the film-substrate interface, with the substrate to the upper left and film to the lower right. The white boxes show a section of each layer that has been expanded and contrast enhanced to show the details. The scale bars in the inset boxes are 2 nm. Two Kirkendall voids are marked with the letter K.

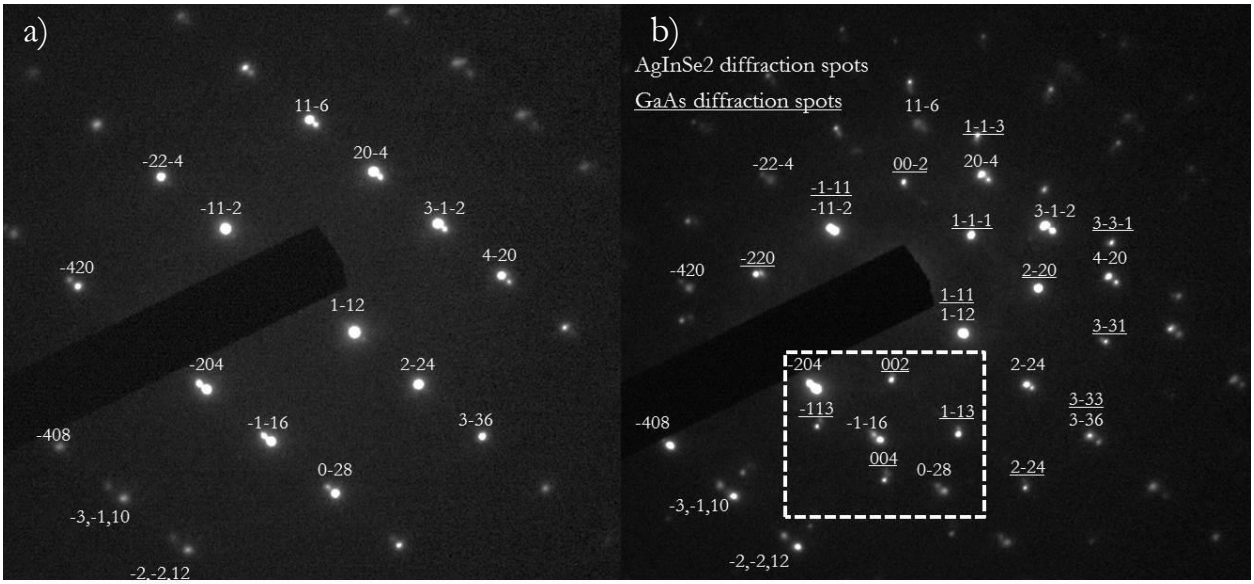

Figure 5.8: Selected area diffraction patterns of the AIS film a) away from the interface and b) at the interface such that film, substrate, and an additional set of diffraction spots are shown. Diffraction spots that have been identified as due to AIS are labeled, along with GaAs substrate spots, which are underlined to show the difference. The region enclosed in a dashed white box is enlarged in Fig. 5.9.

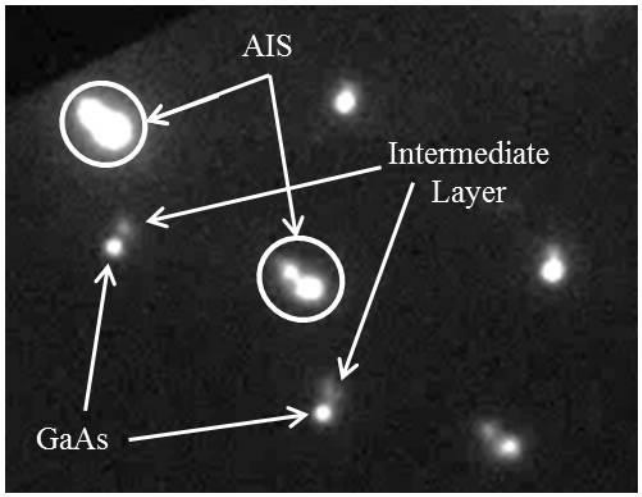

Figure 5.9: Section of the selected area diffraction pattern shown in 5.8b, which shows, in addition to the AIS and GaAs spots (labeled) an additional set of diffraction spots that are attributed to the intermediate layer

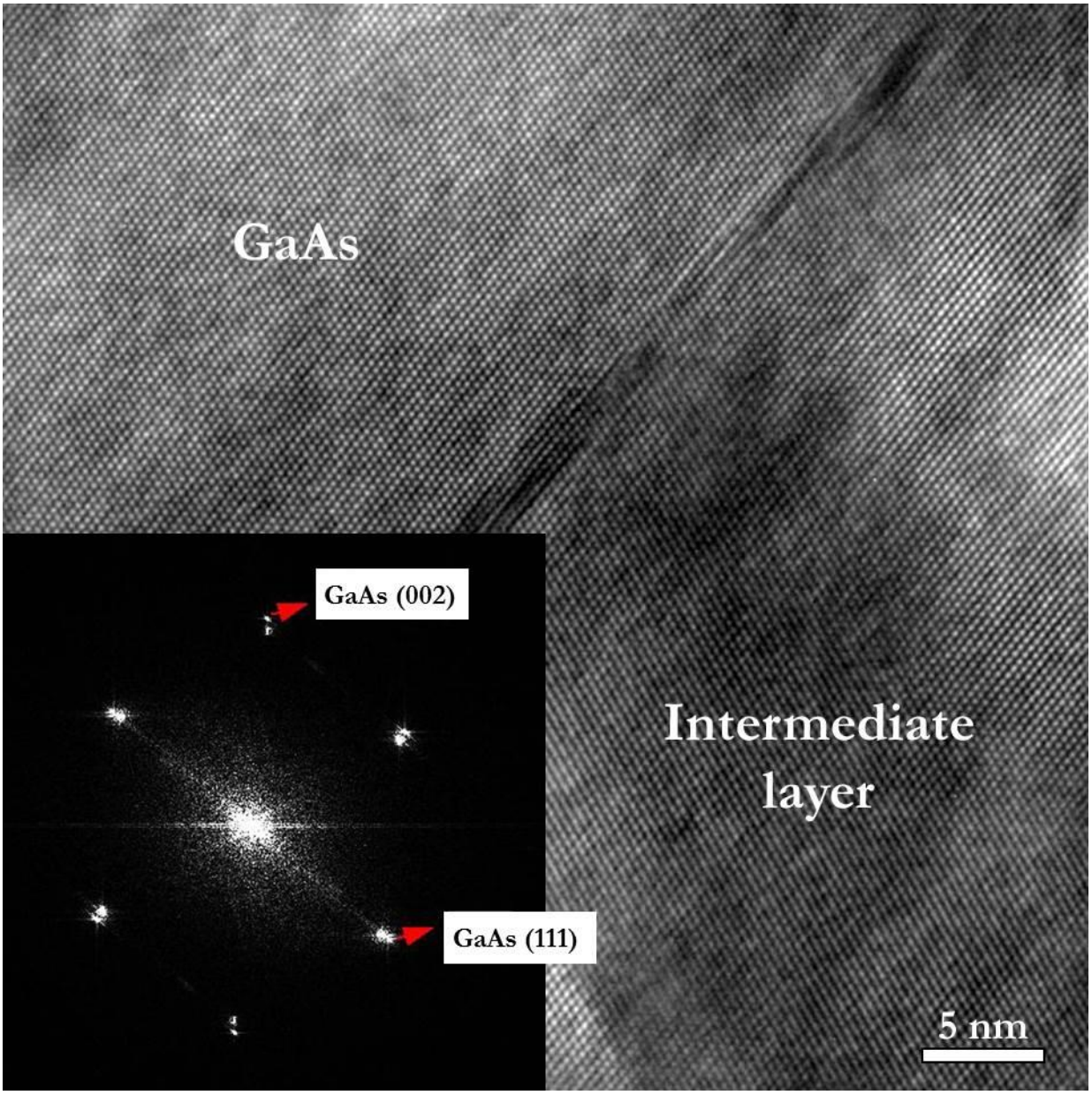

Figure 5.10: Lattice image taken at the interface between the GaAs substrate and the intermediate layer. A power spectrum density image is shown in an inset, taken from the entire region of the lattice image that encompasses both regions. Two sets of spots appear which correspond to each layer.

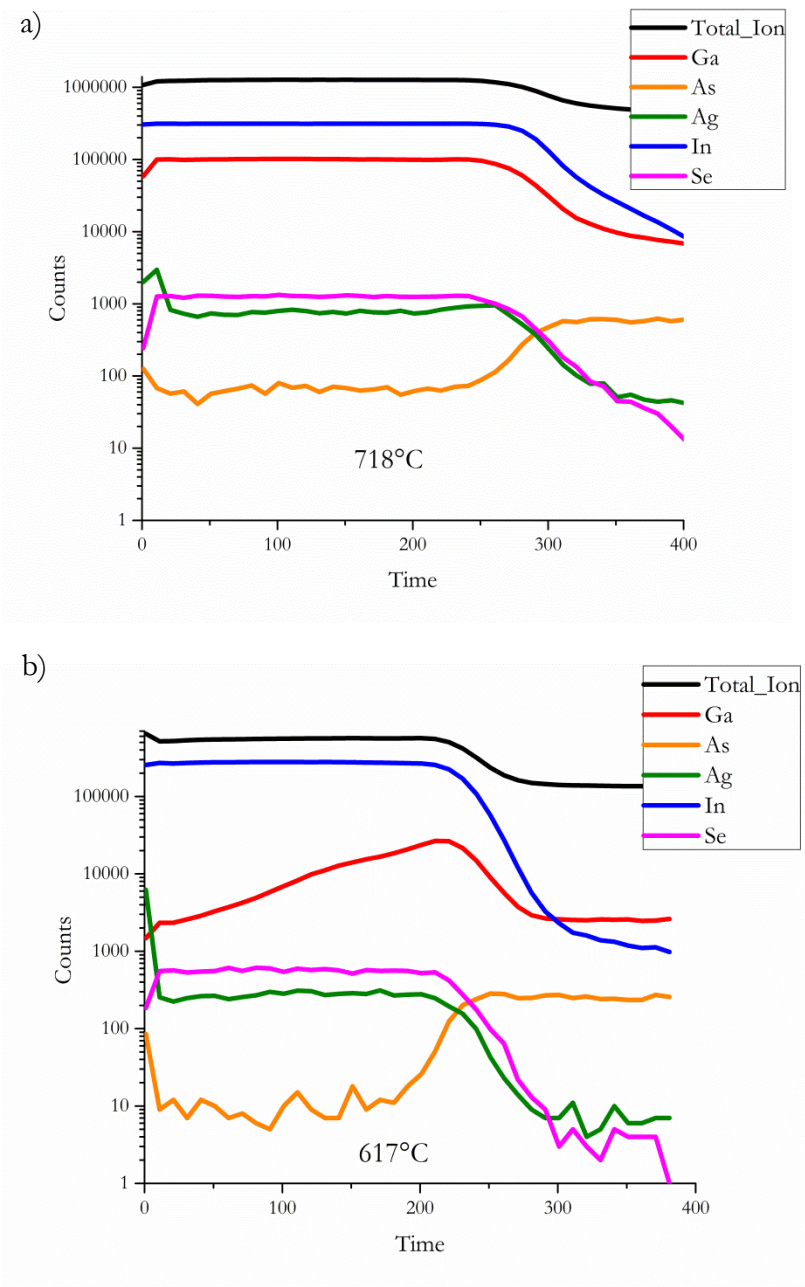

Figure 5.11: Secondary ion mass spectrometry profiles for two samples of AIS, the (111)B samples from sets 2 and 8 in Table 5.1, grown at a) 720°C and b) 620°C, as a function of sputtering time in seconds.

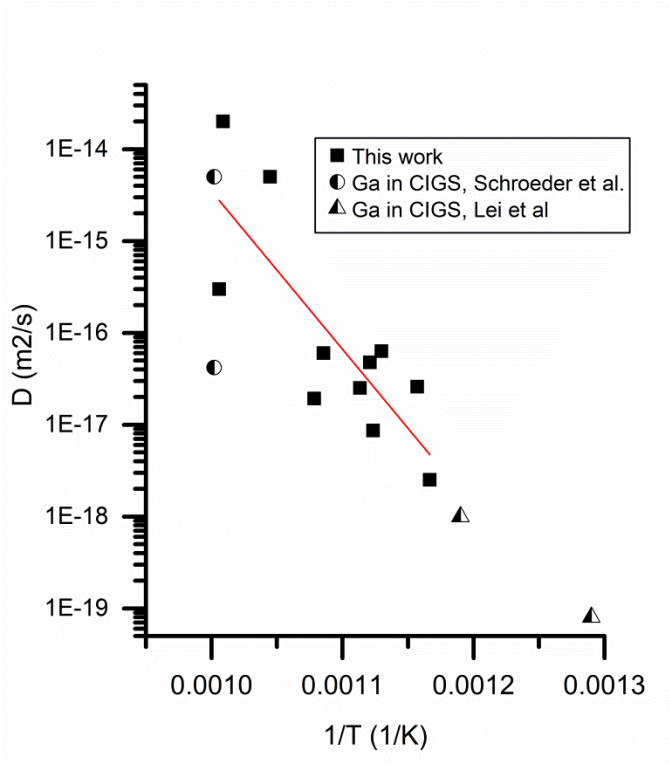

Figure 5.12: Arrhenius plot showing diffusion coefficients for AIS data in this study (black squares). Data is compiled from samples of all orientations in three data sets, set 2, 6, and 8 from Table 5.1. Additional points not included in the fit but plotted in the graph are literature results for the diffusivity of Ga in CIGS by Schroeder et al. [12] (circles) and Lei et al. [11] (triangles).

CHAPTER 6

SURFACE ATOMIC STRUCTURE

6.1 Introduction

This chapter will discuss measurements of the surface of AIS at the atomic scale using scanning probe microscopy, mainly scanning tunneling microscopy (STM). The observations by scanning tunneling microscopy (STM) on the shape and scale of steps will be discussed, along with the implications that can be drawn about growth based on these findings. The surface atomic structure of (112) AIS was directly observed in this study. Most of these findings have been published [1].

6.2 Results and discussion

An AIS film grown on GaAs(111)A at 670°C as described in section 3.2 and prepared for STM analysis using the method described in section 3.4. Initial imaging included a variety of conditions in order to establish those that yielded the best imaging, and the conditions are described in section 3.4. Fig. 6.1a shows a topographic scan region of the surface with several terraces present, nearly all of which appear to originate or end at screw dislocations. Both left and right handed screw dislocations were observed across the surface. A height profile along the red line shown in Fig 6.1a is plotted directly below it in Fig. 6.1b. The profile shows terrace steps are about 0.6-0.8 nm in height, which is consistent with steps of about two atomic layers in height. The 253 nm wide scan from which Fig. 6.1 was acquired is shown in its entirety in Fig. 6.2a. There are two important features of this surface that are revealed through this image. First, the screw dislocations and their prevalence across the surface are illustrated, and it appears even more apparent that screw dislocations serve as starting points for nucleating new terraces. The black square in Fig. 6.2a highlights what is likely a newly nucleated terrace approximately 25 nm from start to end. An image was acquired here to better observe details of this screw dislocation pair, which is shown in Fig.

6.2b. The pair consists of a left and a right handed screw dislocation. It seems plausible that these screw dislocations could originate at the interface of the substrate and film, especially considering the large lattice mismatch between them. Given the step height of the terraces formed by the screw dislocations, the burgers vector for the screw dislocation is given by **b** = 0.7nm **<1 1 2>**. Based on the image size, the screw dislocation density observed at the surface is about 10^{10} /cm^2. The local density observed here seemed typical among regions probed in this study, though it is possible some areas could have locally higher or lower densities.

The second conclusion that can be drawn from Fig. 6.2a is related to the terrace edge structure. The terraces appear to meander in any direction with little preference toward forming outward or inward kinks. Triangular features can be observed along terraces in several locations, both triangular notches that go into the terrace (top left corner of Fig. 6.2a, for example) and triangular protrusions that jut out from the terrace edge. Deviations in terrace edges from forming a straight line require an amount of energy, either to remove an atom to form an inward kink or to add an atom for an outward one. This is the kink energy, which is related to the bonds that need to be broken or formed in order to form the kink. It is clear from this image that there seems to be no preference at all toward straight edged terraces, which indicates that the kink energy is extremely low for this surface. This is in stark contrast to the (112) $CuInSe_2$, for which atomic force microscope images have revealed straight terraces, which tend to form in triangular shapes due to a preference for growth on specific terrace edges, which gives rise to larger scale morphological features consisting almost exclusively in triangular mesas.

To help visualize the contrast between the two materials, Fig. 6.3a-b shows SEM images of AIS (112) (Fig. 6.3a) and CIS (112) (Fig. 6.3b). The samples were both grown epitaxially on GaAs by the hybrid growth process. The AIS sample was grown at 670°C and CIS grown at 725°C; however, since AIS has a lower melting temperature than CIS, the homologous temperatures are 0.90 and 0.81

for AIS and CIS, respectively. The difference in size scale of the morphological features between the two materials is significant; in Fig. 6.3b the AIS surface is magnified 35,000 times while CIS is magnified 5,000 times in 6.3b. The SEM images reveal that the surface of AIS forms plateaus that form in a wide variety of shapes. Hexagons, triangles, and other polygons of varying size can be found throughout the region shown. The shapes of these are indicative of the shape of the terraces upon which growth carries out. The surface of CIS shows almost exclusively large, triangular pyramids that are formed by triangular terraces with flat edges.

To illustrate the height scale of the morphology, Fig. 6.4 is an AFM scan of the same sample on which the STM images were obtained in this study. The film, which has a thickness of about 460 nm measured by SEM of fracture cross section, has an RMS roughness of about 29.8 nm. Even with the large height differences of more than 10-20 nm between mesas, the tops are still extremely flat and it is here that the STM images were acquired.

The surface exposed here is expected to be (112)A terminated AIS, since one would expect the cation-anion stacking in the GaAs(111)A substrate to continue across the interface since the growth is epitaxial. Changing the surface polarity would require a cation-anon stacking fault, which would be energetically unfavorable and has not been known to occur in these materials. The fact that (112)-planes are the lowest in energy lends credibility to the assumption that the surface is of this orientation (see ref. [2] for discussion on this topic regarding CIS).

High resolution STM images were taken in order to gain insight into the surface atomic structure and attempt to determine a surface reconstruction. An atomically resolved image of the surface of AIS is shown in Fig. 6.5 below. Atomic rows are clearly seen along three main directions, and line profiles about 3 nm in length were obtained along these lines to determine the atomic spacings, denoted by green, red, and blue lines. Figure 6.6 plots these profiles, which illustrate the

corrugations and a length scale over several spacings that could give an average spacing. The green, red, and blue lines show regions over which there are six, six, and five atomic spacings, respectively. By dividing the length scale by the number of spacings, one obtains spacings of 0.36 nm, 0.35 nm, and 0.44 nm for the green, red, and blue directions, respectively. Additional measurements at other regions across the sample yielded average spacings of 0.35 nm in directions along the green and red lines, and about 0.41 nm along the blue line.

The measured spacings can be compared to bulk terminated AIS (112)A in order to determine any displacement or restructuring of the surface, in other words the reconstruction. The surface was simulated using Crystalmaker software, using the literature values of a and c for AIS. The results of this are shown in Fig. 6.7a-c, in which a section of the STM topograph is shown (6.7a) alongside a model of the outermost layer of atoms (6.7b), which for the AIS(112)A surface is a termination in Ag and In atoms, shown in gray and white, respectively. One can see that there are three main directions over which atoms are lined up. Two of these directions consist of rows that are arranged two by two of each type, so Ag-Ag-In-In-Ag-Ag- etc. One direction is arranged one-by-one, such that the ordering is Ag-In-Ag-In- etc. For bulk terminated AIS these two types of ordering lead to two different lattice spacings, 0.42 nm and 0.43 nm, as well as a distortion of the angles between the rows that would be 120° if the rows had equal spacings, such that two of the angles are 120.6° and one angle is 118.7°. The angles between the atomic rows measured experimentally for this surface are shown in Fig 6.7a.

The angles and spacings as measured on this surface, while they do show some distortion, apparently have an arrangement that is consistent with all bulk atomic positions for this surface being occupied. One difficulty with conventional STM is that it is not possible to identify which atoms are Ag and which are In, though some studies have shown that by using different polarity one

can highlight cations or anions for III-V semiconductors like GaAs [3]. Thus it is possible that there could be antisite defects between the two cations that cannot be observed by STM. This question is currently the subject of ongoing theoretical modeling project.

If the surface is indeed bulk terminated, this may have profound implications for its use in devices. The CIS (112) surface, while its reconstruction has not been directly shown by STM, has been shown to be Cu-deficient in the first three layers [4], which provides space for Cd atoms from the buffer layer, CdS, to occupy the vacated Cu positions, leading to a heavily n-type doped surface region that forms the homojunction [5]. If similar group-I vacancies do not form at the AIS surface, there may not be a formation of this heavily doped layer and it may instead operate as a heterojunction. This is an important consideration if Ag is to be added to CIGS devices to improve performance or widen the band gap, whether or not the device architecture could benefit from modifications.

6.3 Conclusions

The surface of AIS (112)A has been examined by STM, yielding information about how growth propagates. Epitaxial growth is mediated by screw dislocation, which appear to be the source of terrace formation. The terrace height has been measured, showing that they consist of doubled steps. Atomically resolved images of the AIS surface were obtained for the first time, and the atomic arrangement shows that short of substitutions, the atoms are near the locations expected for bulk terminated AIS (112)A. This apparent lack of a significant reconstruction is surprising for a polar surface, and it illustrates that AIS is a material with markedly different surface properties than closely related CIS, which will have implications for devices fabricated from Ag-compounds.

6.4 References

[1] P. Peña Martin, A. A. Rockett, and J. Lyding, "Growth mechanism and surface atomic structure of $AgInSe_2$," *J. Vac. Sci. Technol. A*, vol. 30, p. 04D115, 2012.

[2] D. Liao and A. Rockett, "The structure and morphology of (112)-oriented $Cu(In,Ga)Se_2$ epitaxial films," *J. Appl. Phys.*, vol. 104, no. 9, p. 094908, 2008.

[3] M. Feenstra, J. A. Stroscio, J. Tersoff, and A. P. Fein, "Atom-selective imaging of the GaAs(110) surface," *Phys. Rev. Lett.*, vol. 58, no. 12, pp. 1192–1195, 1987.

[4] D. Liao and A. Rockett, "Cu depletion at the $CuInSe_2$ surface," *Appl. Phys. Lett.*, vol. 82, no. 17, p. 2829, 2003.

[5] D. Liao and A. Rockett, "Cd doping at the $CuInSe_2$/CdS heterojunction," *J. Appl. Phys.*, vol. 93, no. 11, pp. 9380–9382, 2003.

6.5 Figures

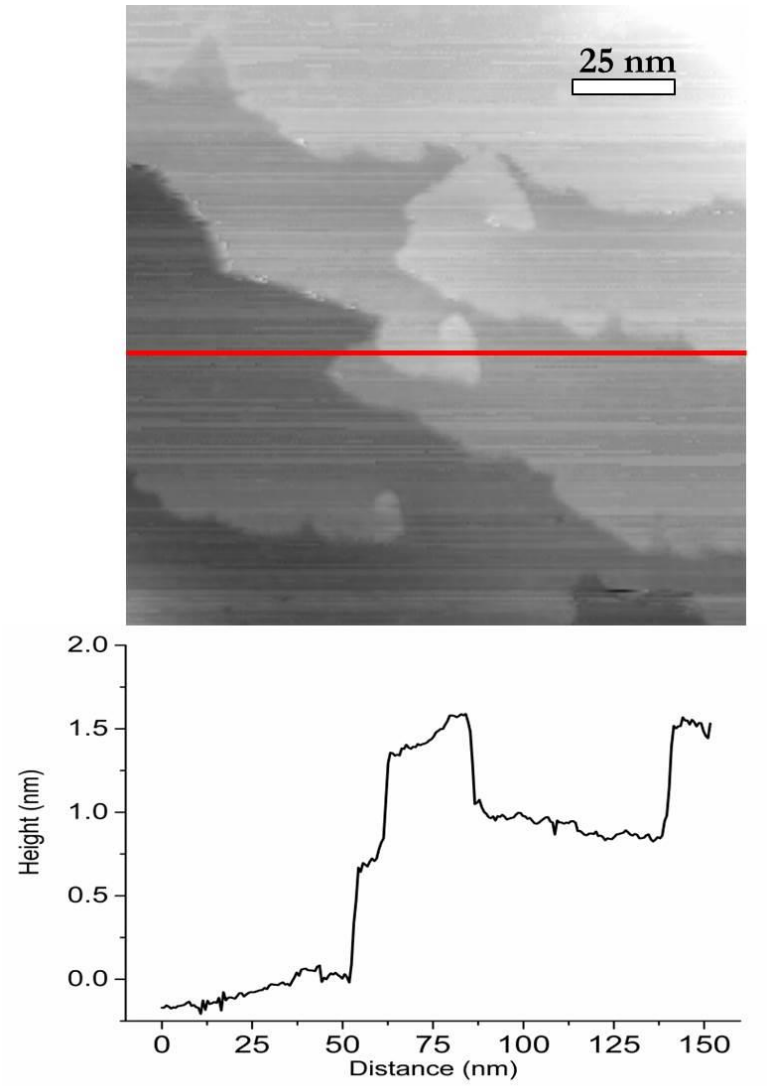

Figure 6.1: STM topographic image (a) of the surface of AIS (112)A. The image is 151 nm in width and a section of a larger scan to show detail of the terraces and screw dislocations. The scan was acquired at 0.5 nA current and a sample bias of +2.5 V. A height profile along the image in the location denoted by a red line is shown below (b).

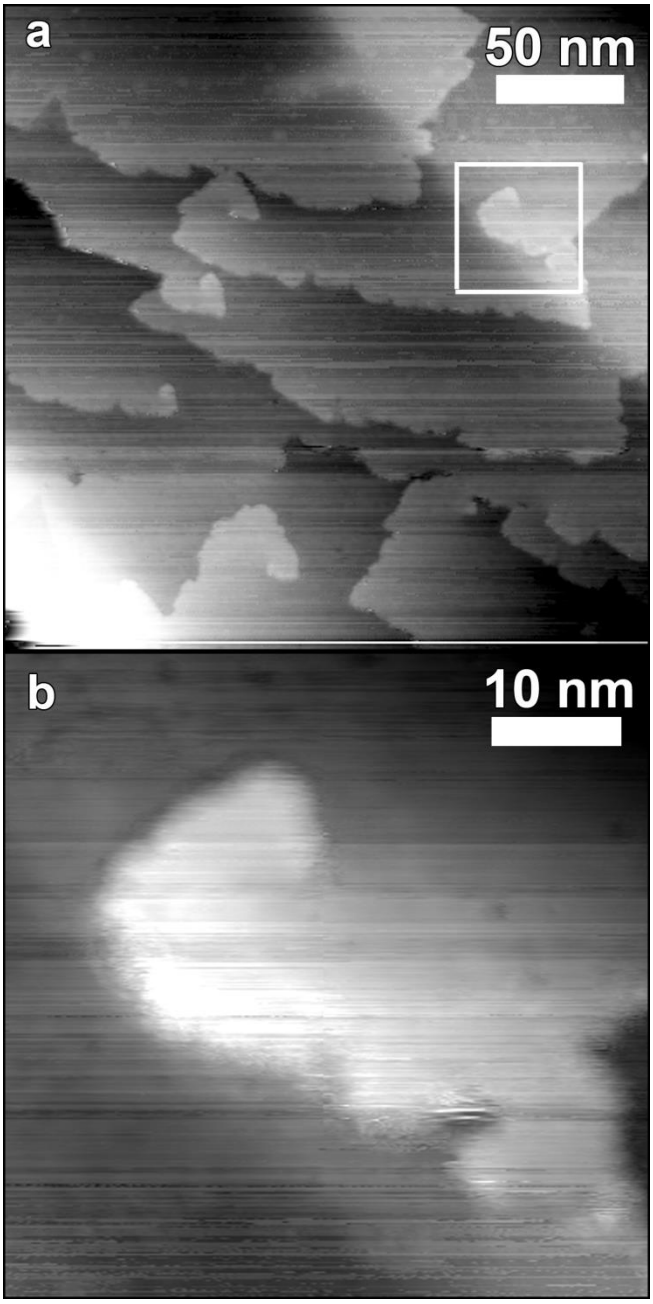

Figure 6.2: STM topographic image (a) of the surface of AIS (112)A. The image is 253 nm in width and was acquired at 0.5 nA tunneling current and +2.5 V sample bias. Note the triangular features along the terraces that point both inward and outward. The square indicates a region where a detailed scan (b) was subsequently acquired, 50 nm in width, at the same tunneling current and a sample bias of +2.0 V. Reprinted with permission from Pamela Peña Martin, Angus Rockett, and Joseph Lyding, "Growth mechanism and surface atomic structure of $AgInSe_2$", Journal of Vacuum Science & Technology A, Vol. 30/4 04D115 (2012). Copyright [2012], American Vacuum Society.

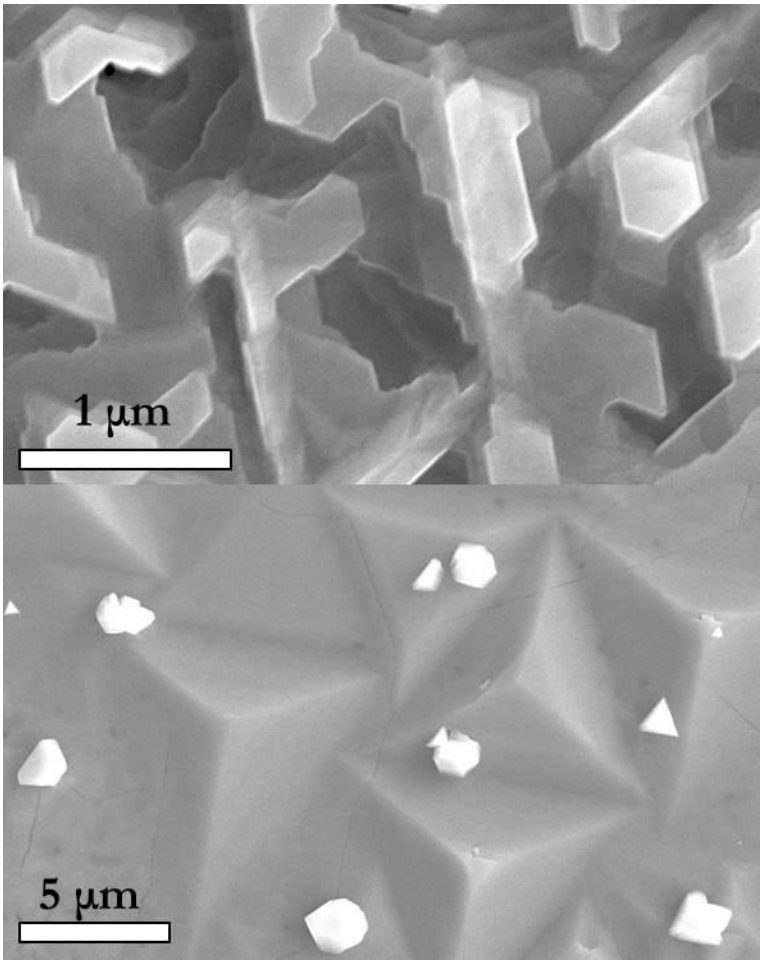

Figure 6.3: SEM micrographs of (a) of the surface of AIS (112) at a magnification of x35,000 and (b) CIS (112) at a magnification of x5,000.

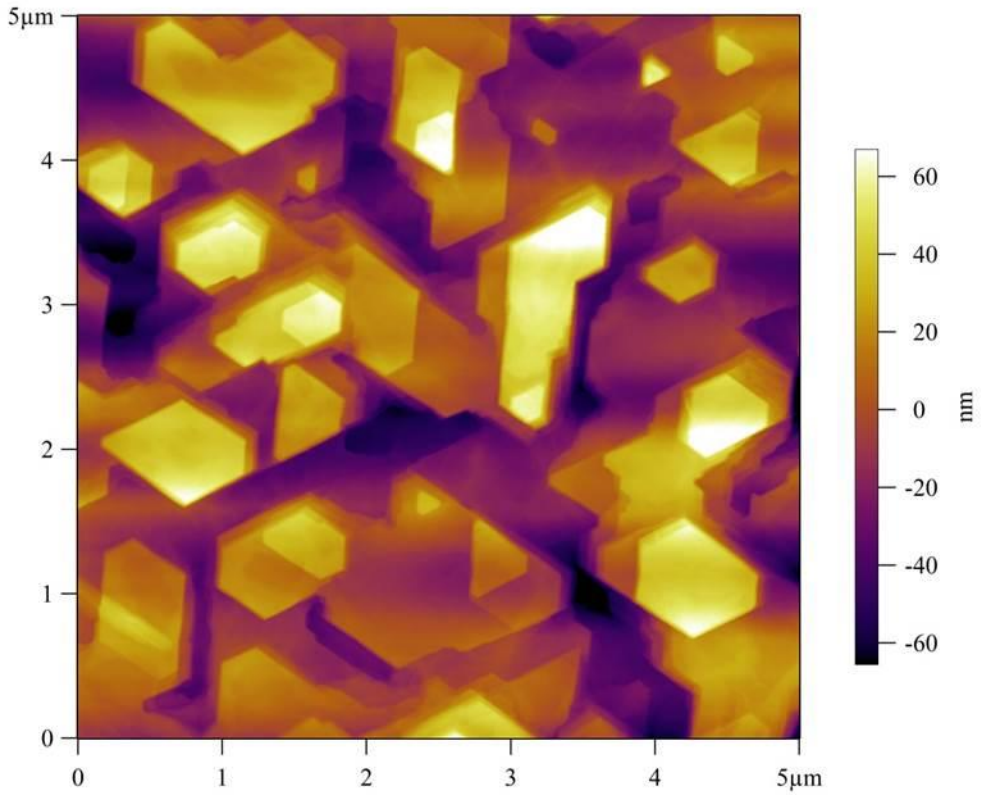

Figure 6.4: Atomic force microscope topograph of AIS(112)A. Image acquired in tapping mode.

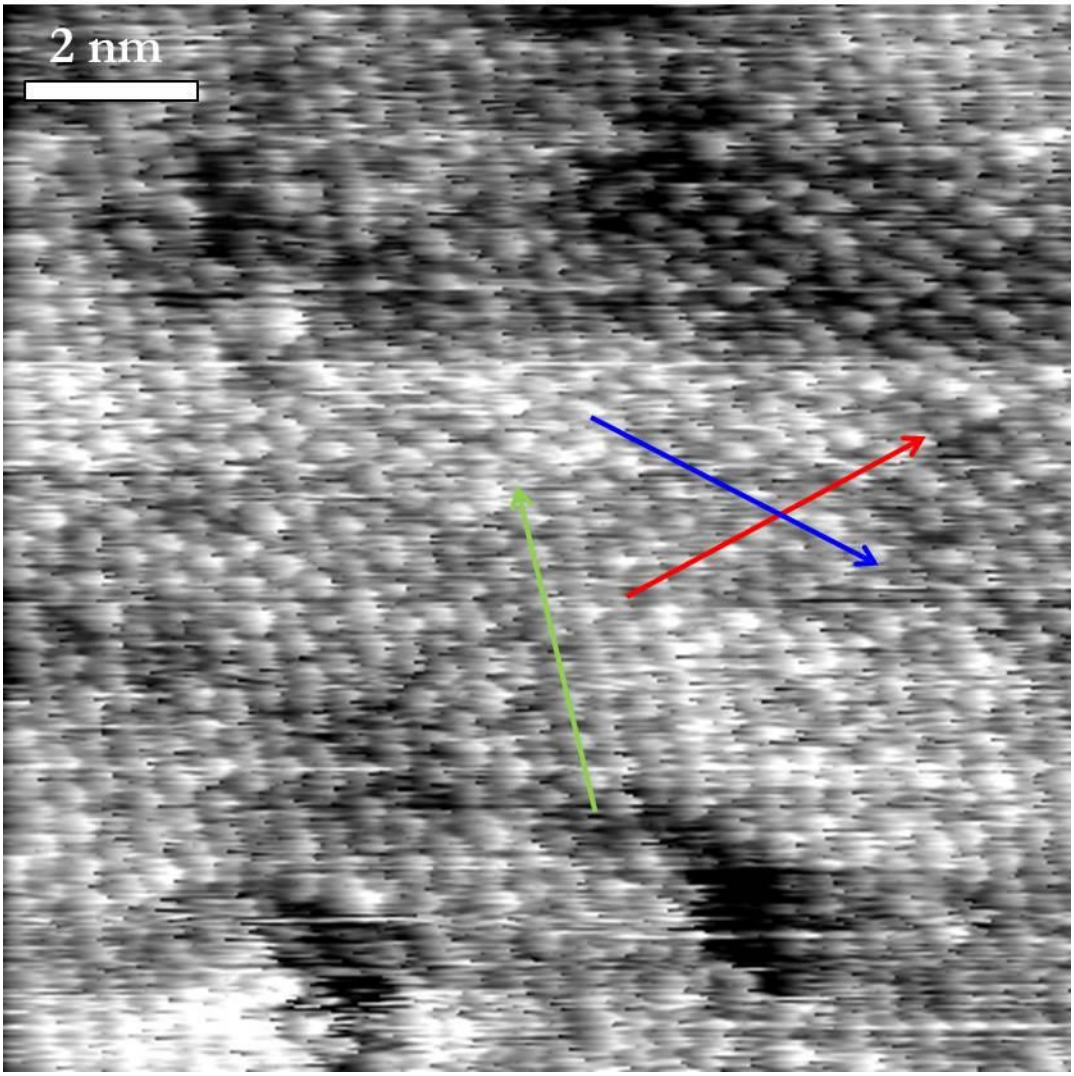

Figure 6.5: STM topographic image showing the AIS (112)A surface with atomic resolution. The 12.3 nm wide image was acquired at 0.1 nA and +2.5 V. The green, red, and blue lines indicate locations where height profiles were acquired to show the detail of the atomic spacing along different directions.

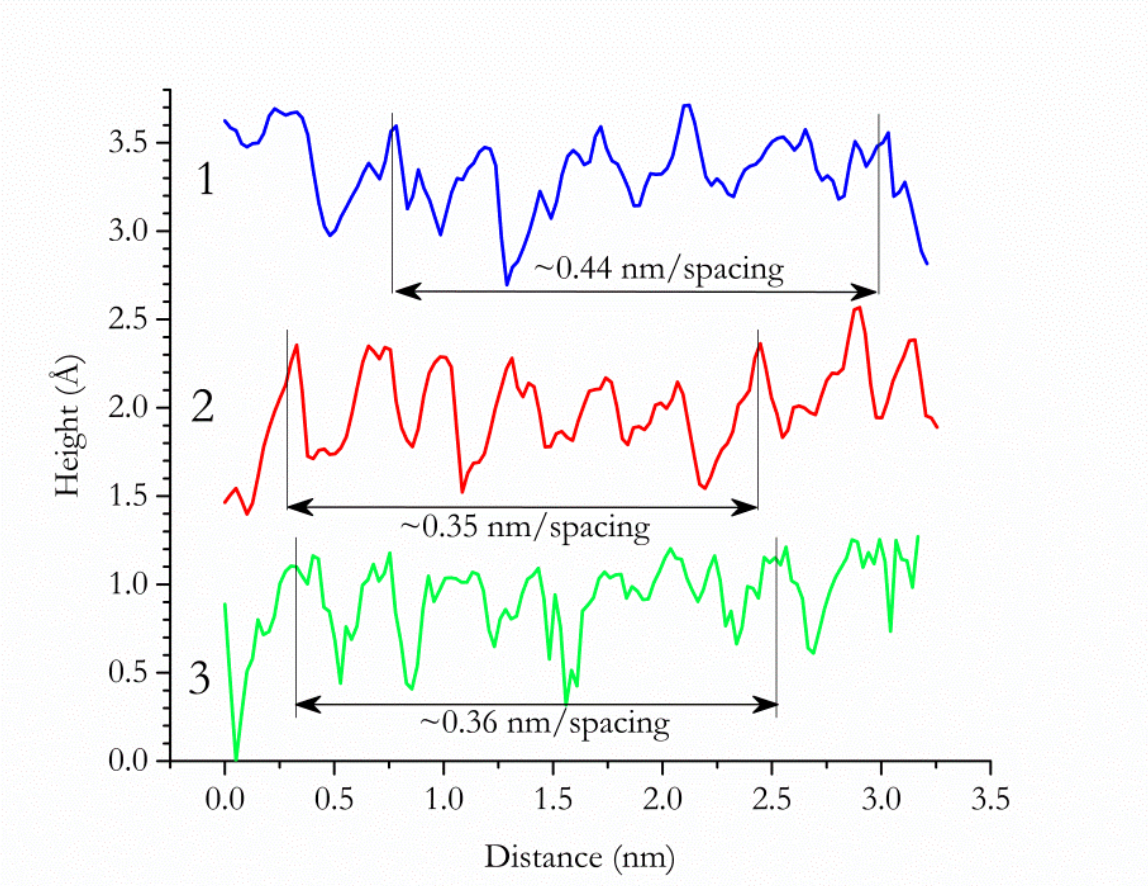

Figure 6.6: Height profiles acquired from the STM topographic image shown in Fig. 6.5 in the locations corresponding to the lines. The colors of the lines match those in Fig. 6.5 to indicate which topograph matches. The red and green lines show a region over which 6 atomic spacings were measured, yielding the approximate average atomic spacing, and the blue line has a measured average spacing over 5 spacings.

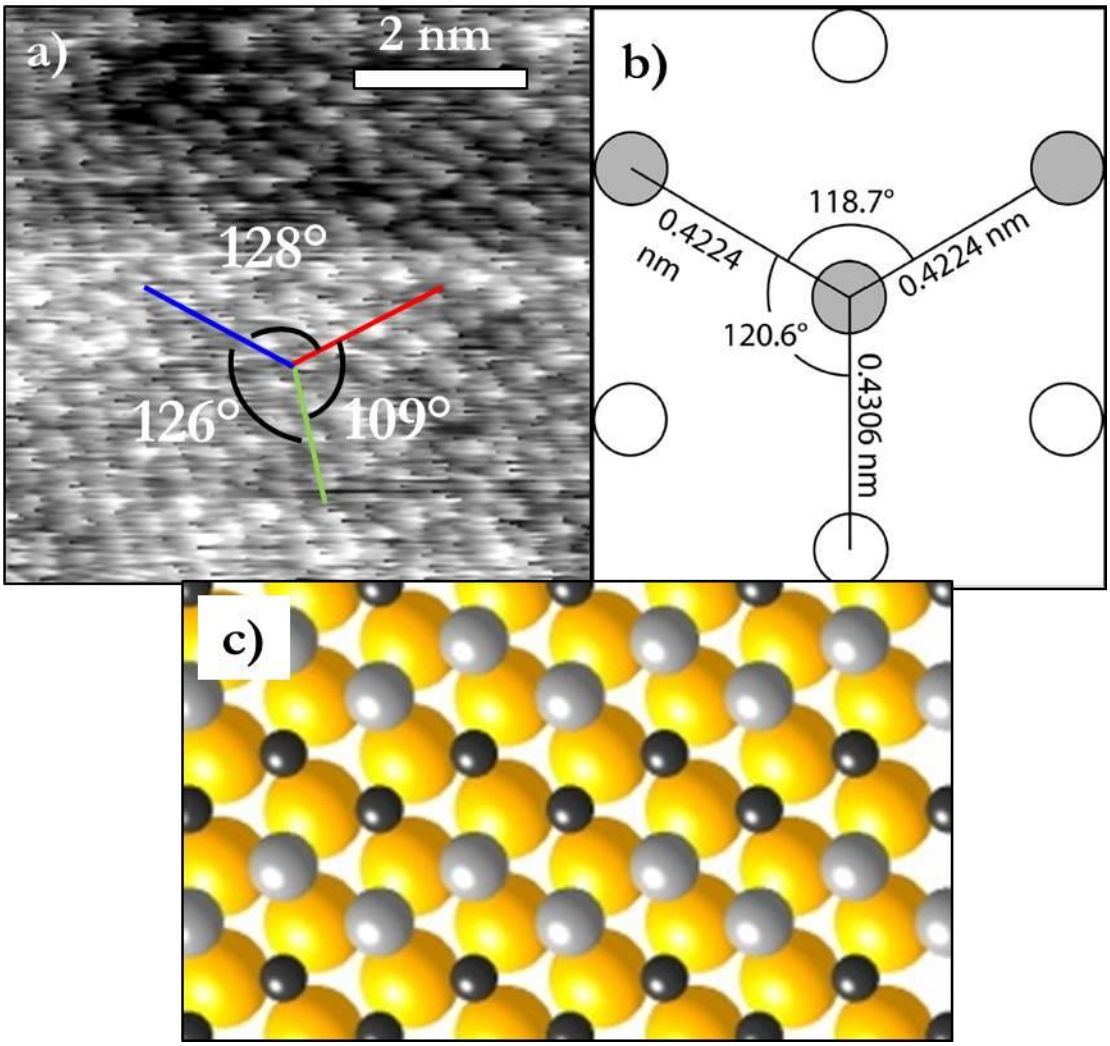

Figure 6.7: A section of the topograph from Fig. 6.5 with the directions and angles shown, along with representations of the surface atomic spacings for bulk terminated AIS (112)A using the lattice parameters from literature, in which white atoms represent In atoms and gray represent Ag, with the spacings and angles labeled (b) Reprinted with permission from Pamela Peña Martin, Angus Rockett, and Joseph Lyding, "Growth mechanism and surface atomic structure of $AgInSe_2$", Journal of Vacuum Science & Technology A, Vol. 30/4 04D115 (2012). Copyright [2012], American Vacuum Society. Finally, a simulated bulk terminated AIS surface with the top two layers of bulk terminated AIS(112)A showing the In and Ag (black and gray, respectively) and the underlying Se atoms (yellow). Figures 6.7b and c were made using Crystalmaker software.

CHAPTER 7

SURFACE ELECTRONIC STRUCTURE

7.1 Introduction

The surface electronic properties of a semiconductor are extremely important to understand in order to predict what will happen once it forms a heterojunction to help turn it into a device. Surface studies of CIS have been critical to understanding the importance of having the right heterojunction partner, in that simply considering obvious things like the work function and lattice parameter is not enough. Additionally, surface defect states can pin the Fermi level and cause the band alignment to differ from what is predicted, with the potential for trapping charge or making barriers to carrier conduction. Clearly having an understanding of the surface electronic properties is a crucial step in making a material relevant to devices.

This chapter will show the results of electronic properties measurements of the surface of AIS at the atomic scale using scanning tunneling spectroscopy (STS) in an STM. The surface band gap and conductivity type were acquired, and a decaying tail of states was observed to emanate from the valence band edge. Band edge fluctuations were also measured and found to be less than those previously measured for CIS. These findings have been published [1].

7.2 Results and discussion

An epitaxial thin film of AIS (112)A grown at 670°C was studied in UHV by STS, in which current-voltage (I-V) measurements are obtained during the acquisition of the STM topography scan at predefined locations. The method for taking the I-V curves is described in detail in section 3.4. Figure 7.1a shows a topographic scan, during which a line of 80 I-V points were acquired at a spacing of 0.12 nm. The topographic image itself shows the surface atomically resolved, with corrugations easier to see in the current mode image of 7.1b. There are dark features in the scan that

indicate lower local density of states in that particular region, for example the dark region near the top center part of the image that is 3-5 nm in width. These are likely real local electronic fluctuations. Additionally there are some streaks in the image. Those that occur from one line to the next are likely tip changes upon interacting with surface adsorbates or water molecules that were not completely driven off during the low temperature anneal before these measurements were taken.

A representative curve out of those 80 points is plotted in Fig. 7.2. I-V curves were obtained in variable height mode, and the details have been described in 3.4. The bias was swept from -2.0 to +2.0 V, and the measured current is shown. The curve received light Gaussian smoothing to minimize fluctuations that were less than kT, which serves as the minimum energy resolution that can be obtained through STS. As described in the background in section 2.4, the measured tunneling current for a given sample bias is a function of the local density of states. The voltage sweep on the negative side, when the sample is negatively biased, leads to an accumulation of electrons at the surface and therefore tunneling occurs out of occupied states in the sample to the tip. Conversely, at positive biases, the sample surface is electron depleted and electrons from the tip tunnel into unoccupied states in the sample. Thus, the negative bias side of the sweep is probing the valence band of the sample and the positive bias side probes the conduction band. The 0 V position is considered the Fermi level. Fig. 7.2 shows clearly that there is a gap in the density of states, which is expected for a semiconducting surface. However, there is much more information to be gleaned from this I-V curve than that.

A band gap can be measured once the band edges are determined. To determine the band edges in a more precise way, the conduction and valence bands were each fit with a forth order polynomial, shown in Fig. 7.2 by the dotted and dash-dotted lines, respectively. The noise floor of $3x10^{-15}$ A is represented by a horizontal square dotted line in the figure. The locations where the band edge fits meet the noise floor were considered the band edges for this study. The width

between these, the band gap, is about 1.3 eV. This matches closely with the experimentally measured bulk band gap of 1.25 eV for AIS [2], which is not necessarily an anticipated result. Surfaces often exhibit electronic properties that are different than the bulk due to the presence of dangling bonds or a reconstruction at the surface. For example, Si(111):7x7 reconstructed surface of Si shows states within the gap, which effectively close the 1.1 eV gap that would be expected in bulk Si [3]. The lack of an apparent surface reconstruction in AIS, as discussed in Chapter 6, would seem to indicate that there should be dangling bonds for surface atoms, which should contribute a high density of surface states that would have the potential for significantly altering the surface electronic properties. Apparently this is not the case, which indicates that the dangling bond states are passivated by some means not apparent from surface measurements, such as defects in the underlying layer.

The position of the band edges with respect to 0 V gives an indication of where the Fermi level lies within the gap. In Fig. 7.2, the distance from the Fermi level to the conduction band edge (0.4 eV) is just under half the distance from the Fermi level to the valence band edge (0.9 eV), indicating n-type behavior. Samples grown with the same conditions as the one included in this study were measured by hot point probe which also showed n-type carrier conduction, in agreement with most literature that shows that AIS is typically n-type as grown, and requires further processing steps to convert to p-type conductivity. In semiconductors, the presence of surface states can pin the Fermi level to mid gap, so apparently this is not occurring in AIS. There does appear to be a continuum of states that decay exponentially from the valence band edge well into the gap. This tail could be a signal of defects or dopant states that lead to increases current beyond the band edge. It has been observed that for III-V surfaces, there can arise dopant induced states at the band opposite to the majority carrier type, for example near the valence band in an n-type material [4]. Photoluminescence studies on AIS have observed a decaying tail of states that extended deep into the band gap [5]. One group proposed that this exponentially decaying tail of states actually decay

from the conduction band, where donor sites would be [6], but PL alone gives only the energy of transitions without reference to either band so additional studies are needed to be able to corroborate this. The findings from this STM work seem to indicate that the states decay from the valence band edge.

Including the I-V curve represented in Fig. 7.2, a total of 80 I-V data points were obtained along the line in Fig. 7.1 at a spacing of 0.12 nm. Viewing these points collectively allows one to discern how uniform the observed properties are across the surface and whether or not there are large scale fluctuations present. In Fig. 7.3 the points are plotted as a spectra map in the direction of the arrow in Fig. 7.1, in which the x-axis gives the distance along that line, the y-axis is the voltage range, and a grayscale color map indicates the log of the measured current, with dark (light) color indicating low (high) current. Below the spectra map, with the same distance scale, a height profile is shown from the place where the line was obtained, and the circles that form a dotted horizontal line represent the locations where the IV points were taken. There are fluctuations between low and high current that occur from point to point, with a height scale of about 0.1-0.3 nm, which are potentially due noise, changes in the arrangement of atoms at the end of the tip, or even the presence of mobile surface species that can transfer in and out of the tip-sample junction or even hop onto the tip. The height associated with these fluctuations is consistent with atomic sized height changes between the tip and sample.

There also exists larger scale narrowing and widening of the band gap over the course of several points, or a few nm across the surface, in Fig. 7.3, with fluctuations in the gap occurring mainly due to valence band shifts rather than in the conduction band. These large scale shifts in band gap do not appear to be due to topographic features, which do not show a connection between topographic height and current. Four sections of ten neighboring points have been selected from regions that appear to have a narrow gap, labeled N in Fig. 7.3; a wider gap, labeled W; and two

medium gap sections, M1 and M2. The curves of each set are potted together in Fig. 7.4a-d in gray, with the average of the curves shown in black, to illustrate that the average represents that section of data well. The averages are plotted again in Fig. 7.5a-d along with the polynomial fits to the valence and conduction bands, to show how the band gap of each region was obtained. The gaps of region N, W, M1, and M2, are ~0.9 eV, ~1.5 eV, ~1.2 eV, and ~1.3 eV, respectively. The M1 and M2 regions are closest to the bulk optical band gap of AIS.

Fig. 7.6 shows these average sections plotted together on one plot, which shows the amount of fluctuation in the band edges from one section to another. The valence band of AIS, like other chalcopyrites, is derived from Se p-orbitals, which experience a repulsion from the underlying group I d-orbitals, while the conduction band is mainly composed of group III s-orbitals [7]. Since the fluctuations are observed to mainly occur in the valence band, and the materials are grown with a group I poor composition, the defects responsible for the fluctuations are likely related to the group I defects such as In_{Ag} or V_{Ag}. While these are not identified directly on the surface from STM topographic measurements, these could be in the layer directly below, which could still significantly alter the measured surface band structure. A decrease in the amount of Ag would mean fewer d-orbitals interacting with the Se p-orbitals of the valence band, which could explain a widened gap.

These observations on the surface of AIS represent significantly different electronic behavior than the surface of CIS in earlier STM work. The CIS surface, on which the atoms could not be resolved, showed band tails that extended well into the gap, which showed significant variation across the surface [8]. Fig. 7.7a-b plots the measured band edges as a function of displacement along the surface measured along 10 nm lines on AIS (7.7a) and CIS (7.7b). Each profile is represented by a different shaped marker, circles, triangles, or squares. The solid markers are measurements of the conduction band edge, and the open markers are from the valence band edge. Visually it is apparent that the AIS band edges form a relatively distinct line in the conduction

band and, while there is more deviation in the valence band, a relatively consistent gap is found across both sets of data shown. However, in CIS, both band edge positions shift significantly along the same width. Three profiles show the widely varying behavior and gap width measurement. What is seen visually is quantified in Table 7.1, which gives the average band edge position and a measure of the magnitude of the fluctuations in the standard deviation. The average band edge positions in AIS and CIS both yield an average gap that is consistent with accepted literature values for the optical gaps. However the standard deviation in CIS is higher for both the conduction and valence band edges. The ratio of the conduction band to the valence band position is also computed, which gives a measure of departure from mid-gap of the Fermi level. A value of 1.0 indicates that both bands are equidistant from the Fermi level, meaning it is exactly mid-gap, values less than (more than) 1.0 indicate that the Fermi level is nearer the conduction (valence) band, indicating n-type (p-type) carrier conduction. AIS shows n-type behavior while CIS, which in bulk shows p-type conductivity, appears to be intrinsic in these surface measurements on average. As these fluctuations from bulk behavior represent surface defects, the surface defect density is apparently much higher in CIS than AIS. The lower magnitude of band edge fluctuations in AIS should translate to a device with more uniform behavior across the surface, which should improve device performance.

7.3 Conclusions

The surface of AIS(112)A has been studied and shown to have a number of interesting properties. The first is that the surface shows an average band gap of about 1.3 eV, which is close to the literature reported bulk band gap for this material, as well as n-type behavior. Measuring the bulk gap at the surface is an indication that dangling bonds or other defects are not present to an extent that would cause significant mid-gap states, and showing the Fermi level nearer a band edge instead of at midgap indicates that the Fermi level is not pinned by defects. The valence band has a region of states that decay well into the gap, which were observed in PL studied but not positively

attributed to either band until now, while the conduction band appears sharp. The bands fluctuate across the surface at the scale of a few atoms, and these fluctuations are significantly less than those observed in CIS, indicating a lower defect density.

7.4 References

[1] P. Peña Martin, J. Lyding, and A. Rockett, "Scanning tunneling spectroscopy of epitaxial silver indium diselenide," *Surf. Sci.*, vol. 636, pp. 8–12, 2015.

[2] J. L. Shay, B. Tell, H. M. Kasper, and L. M. Schiavone, "Electronic Structure of $AgInSe_2$ and CuInSe2," *Phys. Rev. B*, vol. 7, no. 10, pp. 4485–4490, 1973.

[3] R. J. Hamers, R. M. Tromp, and J. E. Demuth, "Surface electronic structure of Si(111)-(7x7) resolved in real space," *Phys. Rev. Lett.*, vol. 56, no. 18, pp. 1972–1975, 1986.

[4] R. M. Feenstra, "Tunneling spectroscopy of the GaAs(110) surface," *J. Vac. Sci. Technol. B Microelectron. Nanom. Struct.*, vol. 5, no. 4, p. 923, Jul. 1987.

[5] A. R. Aquino, S. A. Little, S. Marsillac, R. Collins, and A. Rockett, "Identification of defect levels in $Cu_xAg_{1-x}InSe_2$ thin films via photoluminescence," *Photovolt. Spec. Conf. (PVSC), 2011 36th IEEE*, pp. 3532–3536, 2011.

[6] S. Ozaki and S. Adachi, "Optical absorption and photoluminescence in the ternary chalcopyrite semiconductor $AgInSe_2$," *J. Appl. Phys.*, vol. 100, no. 11, p. 113526, 2006.

[7] A. R. Aquino Gonzalez, "Physical and optoelectronic properties of copper silver indium diselenide thin films," 2012.

[8] M. A. Mayer, L. B. Ruppalt, D. Hebert, J. Lyding, and A. A. Rockett, "Scanning tunneling microscopic analysis of $Cu(In,Ga)Se_2$ epitaxial layers," *J. Appl. Phys.*, vol. 107, no. 3, p. 034906, 2010.

7.5 Tables

Table 7.1: Mean valence and conduction band positions (in volts) measured in AIS and CIS, along with the standard deviation in brackets. The positions are given with respect to a fermi level at 0 V. The ratio of the conduction band to the valence band represents the deviation of the Fermi level from mid-gap.

	Valence band position (V)		**Conduction band position (V)**		**Ratio of mean band positions |CB/VB|**
	Mean position	**St. Dev.**	**Mean position**	**St. Dev.**	
$AgInSe_2$	-0.9	0.2	0.4	0.1	0.5
$CuInSe_2$	-0.5	0.3	0.5	0.3	1.0

7.6 Figures

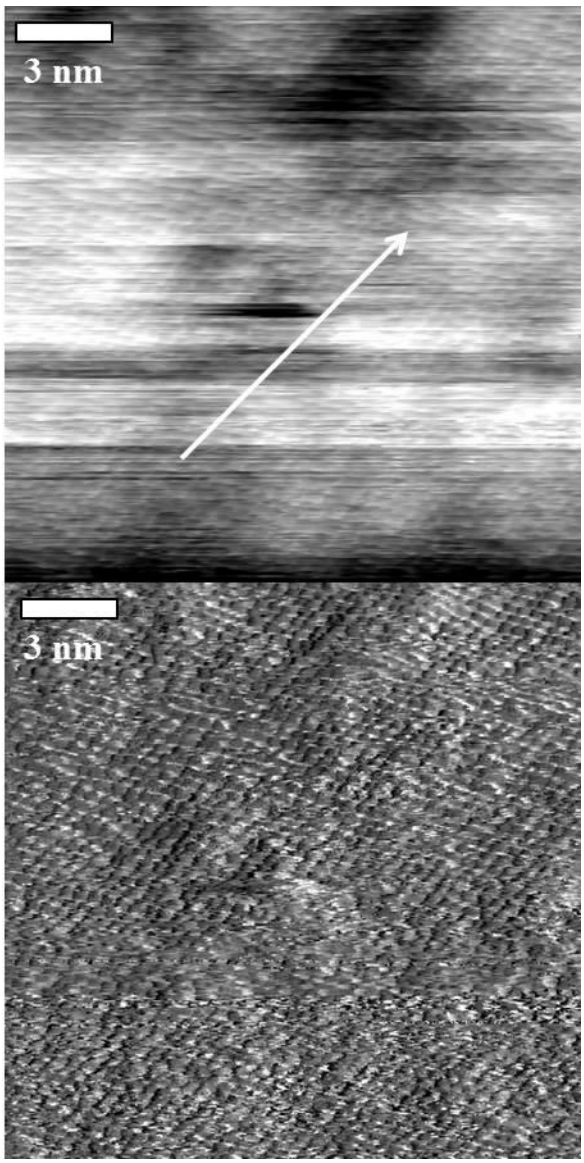

Figure 7.1: STM topographic image 18 nm in width of the AIS (112)A surface during which scan 80 I-V curves were obtain along the line indicated in the upper panel. The lower panel (b) shows the current image, in which the atomic resolution is easier to identify. The scan conditions are 0.8 nA tunneling current and the sample had a bias of +2.5 V. Reprinted from Surface Science, Vol 636, Pamela Peña Martin, Joseph Lyding, Angus Rockett, Scanning tunneling microscopy of epitaxial silver indium diselenide, Page 9, Copyright (2012), with permission from Elsevier

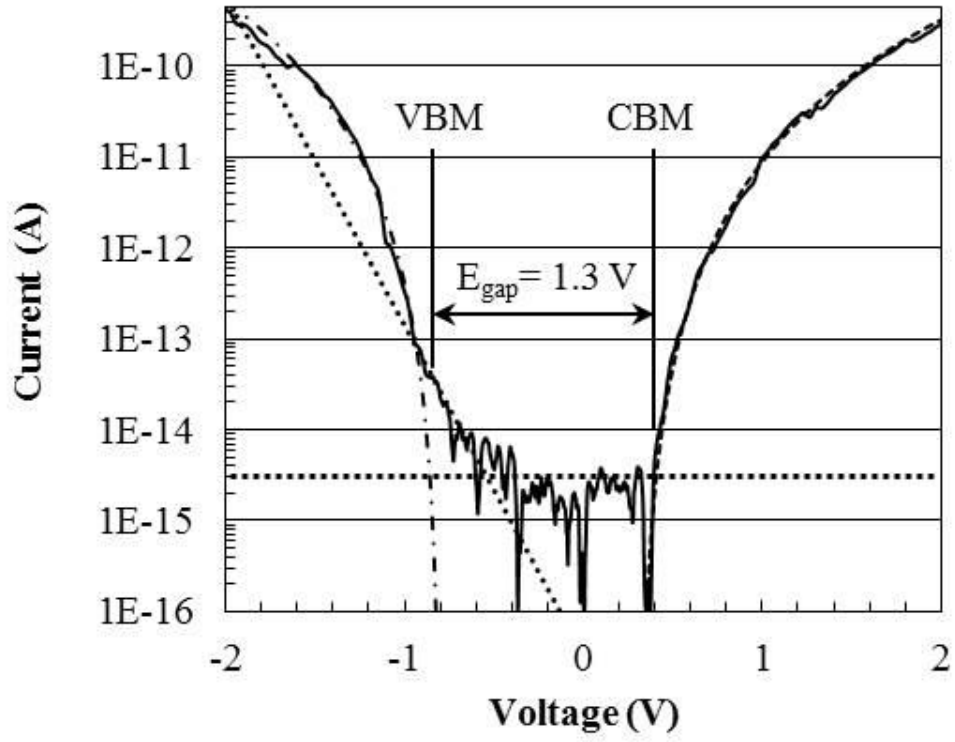

Figure 7.2: A typical I-V curve obtained during the acquisition of the image in Fig. 7.1. The conduction and valence bands were fit by polynomial fits, shown by the dashed and dash-dotted lines, respectively. The fit to the states decaying from the valence band edge are fit with an exponential, shown by the dotted line. The noise level is represented by the horizontal square dotted line, and the locations where the band edges cross this line are considered the conduction band minimum (CBM) and the valence band maximum (VBM), labeled on the figure along with the gap. Reprinted from Surface Science, Vol 636, Pamela Peña Martin, Joseph Lyding, Angus Rockett, Scanning tunneling microscopy of epitaxial silver indium diselenide, Page 10, Copyright (2012), with permission from Elsevier

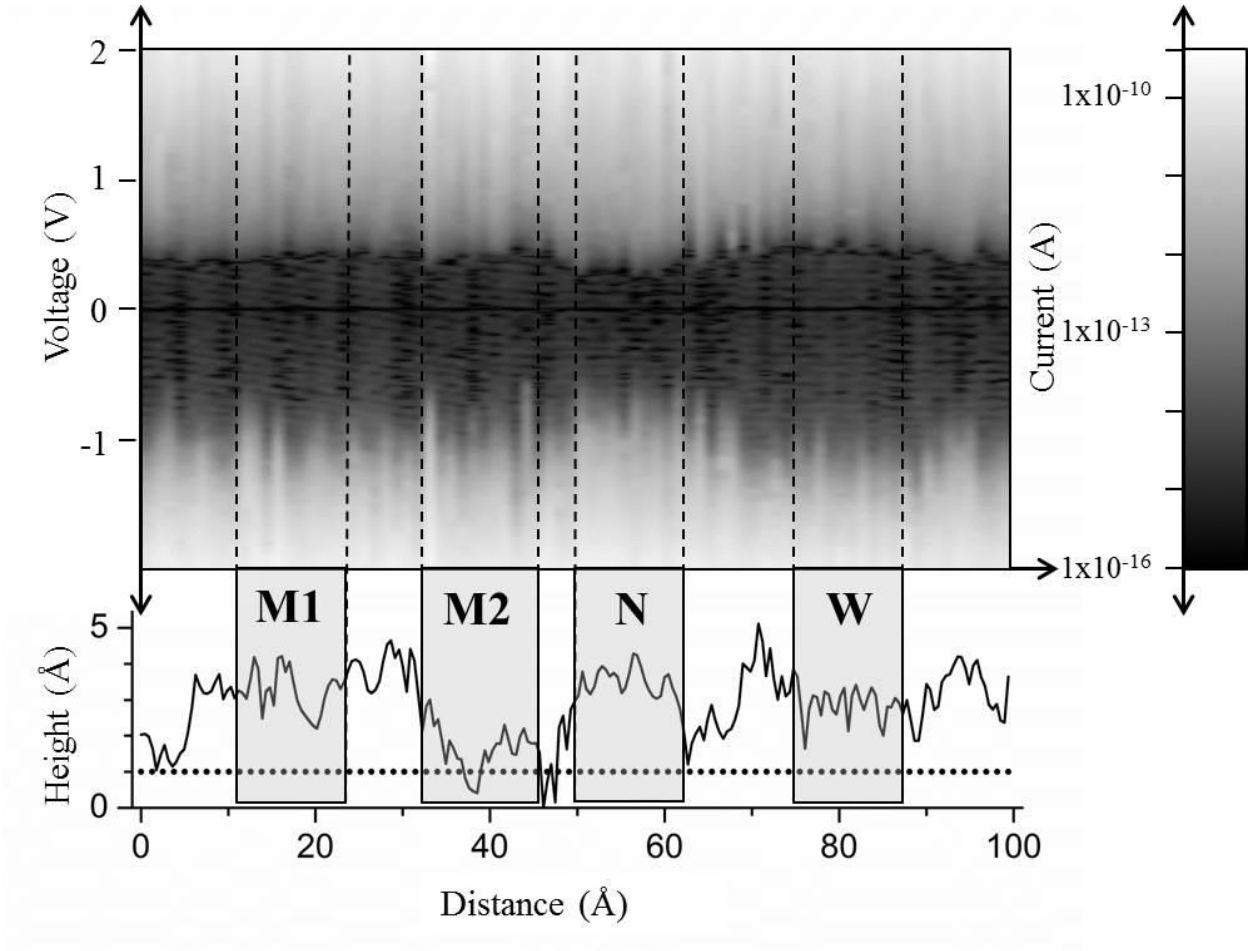

Figure 7.3: A current-voltage spectra map, which plots STS data points obtained during the acquisition of the image in Fig. 7.1. The x-axis is the distance along that line, the y-axis is the voltage range, and a grayscale color map represents current. A height profile shows the topography along the line where the spectra were acquired, and the horizontal row of circles below that represent the locations where the IV points were taken. Reprinted from Surface Science, Vol 636, Pamela Peña Martin, Joseph Lyding, Angus Rockett, Scanning tunneling microscopy of epitaxial silver indium diselenide, Page 10, Copyright (2012), with permission from Elsevier

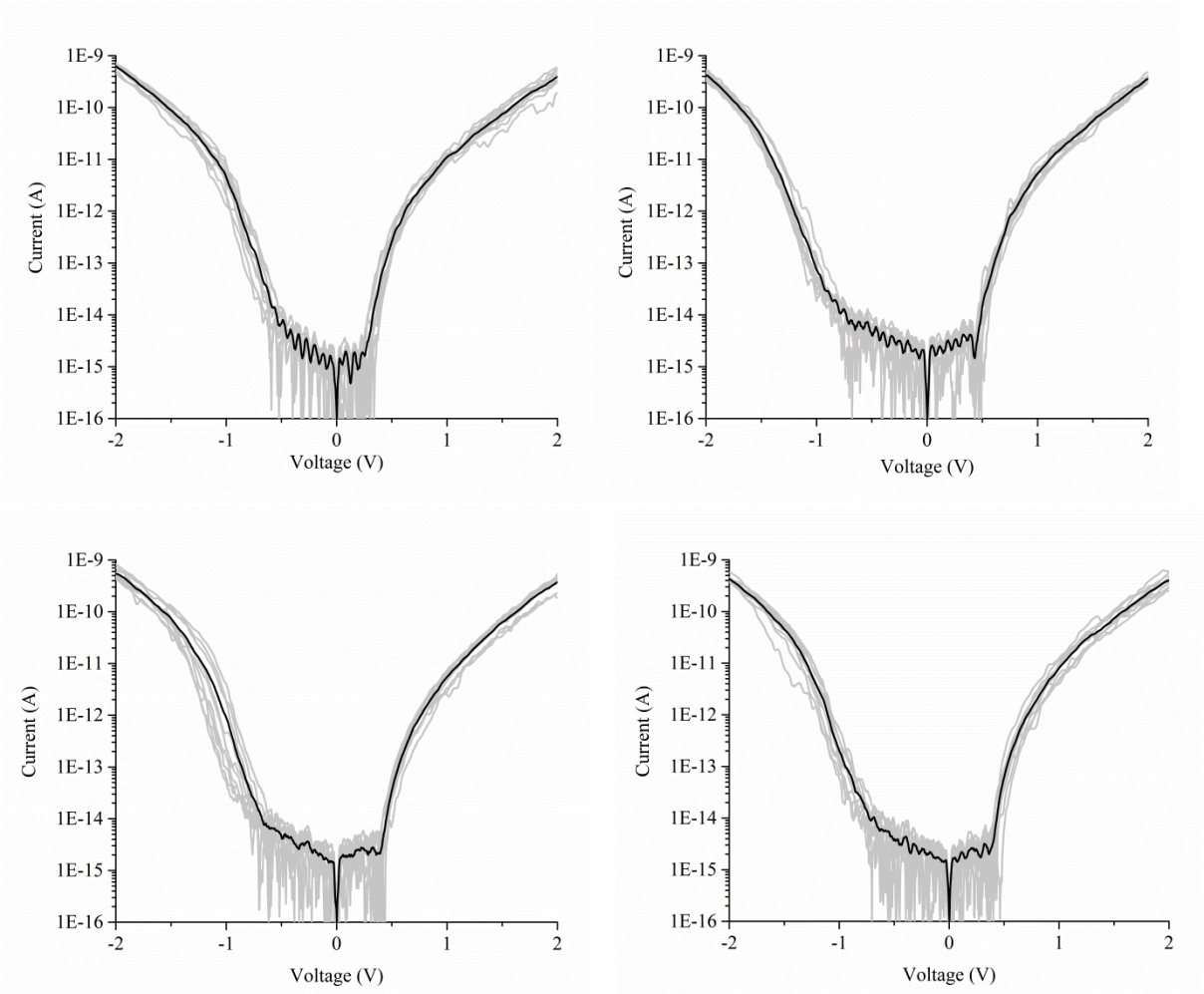

Figure 7.4: The I-V points within the sections from the IV spectra map shown in Fig. 7.3, labeled N, W, M1, and M2. The individual curves are in gray and average of the curves is shown in black. Reprinted from Surface Science, Vol 636, Pamela Peña Martin, Joseph Lyding, Angus Rockett, Scanning tunneling microscopy of epitaxial silver indium diselenide, Supplementary, Copyright (2012), with permission from Elsevier

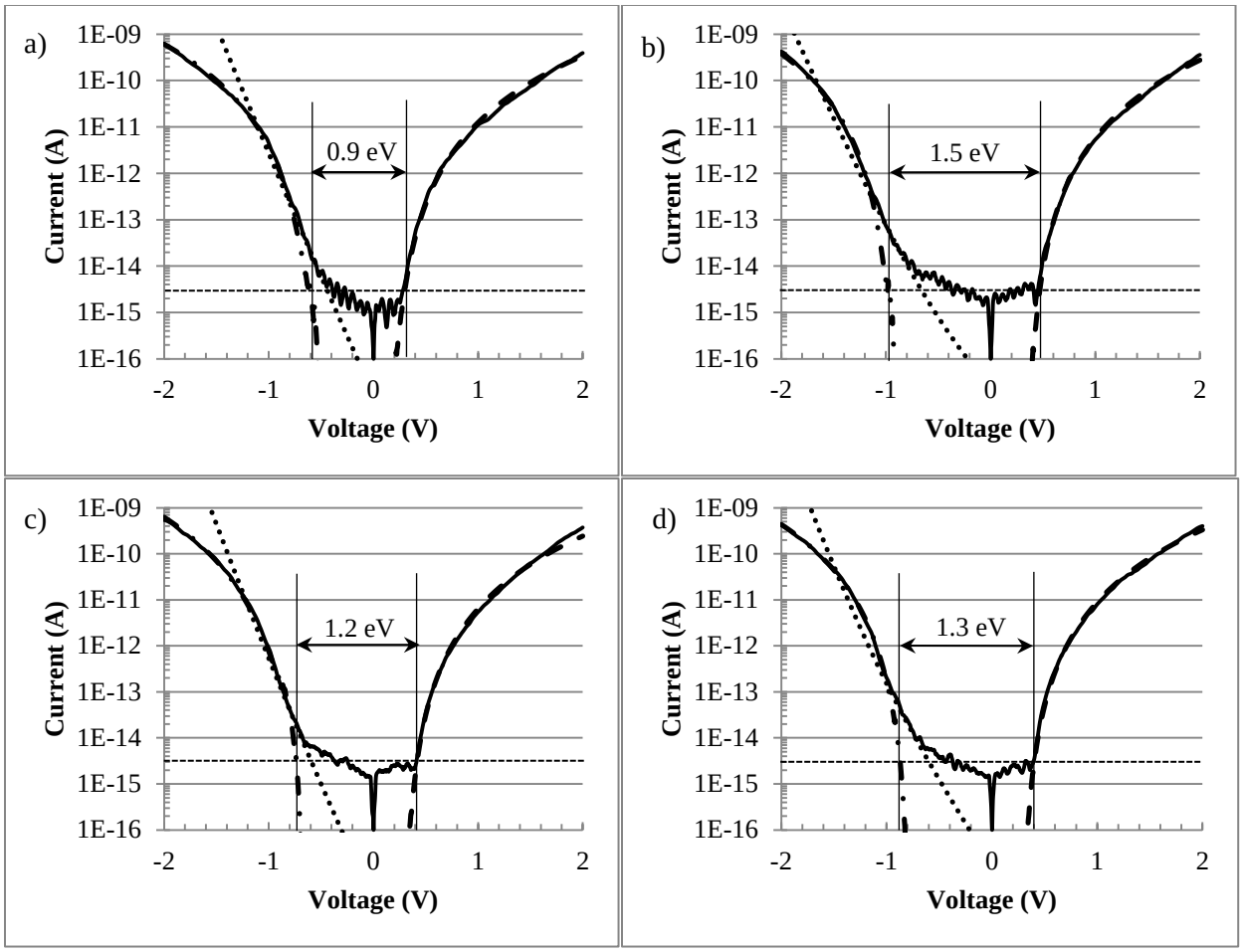

Figure 7.5: The average curves with valence band fits and band gap measurement for the sets of curves in Fig. 4 labeled a) N, b) , c) M1, and d) M2. Reprinted from Surface Science, Vol 636, Pamela Peña Martin, Joseph Lyding, Angus Rockett, Scanning tunneling microscopy of epitaxial silver indium diselenide, Supplementary, Copyright (2012), with permission from Elsevier

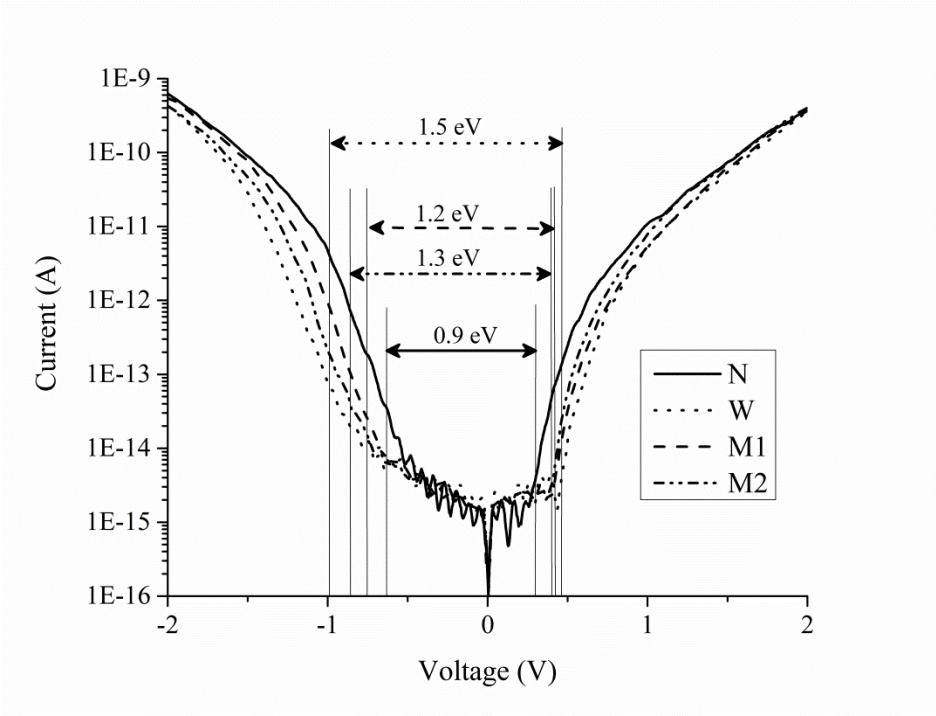

Figure 7.6: The averaged regions N, W, M1, and M2 plotted together to illustrate the fluctuations between the regions. Reprinted from Surface Science, Vol 636, Pamela Peña Martin, Joseph Lyding, Angus Rockett, Scanning tunneling microscopy of epitaxial silver indium diselenide, Page 10, Copyright (2012), with permission from Elsevier

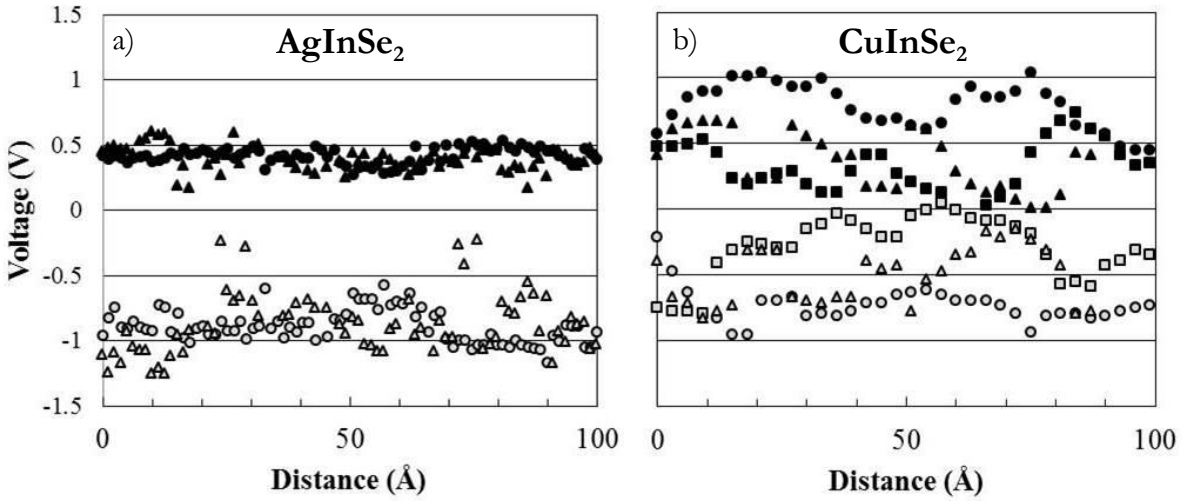

Figure 7.7: Plot showing the conduction (solid points) and valence (open points) band edge positions for two 10 nm sections in AIS (7.7a) and three 10 nm sections in CIS (7.7b) from data collected from an earlier STM study [8]. Each set of points from a given profile is represented with a different shape, circles, triangles, or squares. Reprinted from Surface Science, Vol 636, Pamela Peña Martin, Joseph Lyding, Angus Rockett, Scanning tunneling microscopy of epitaxial silver indium diselenide, Page 11, Copyright (2012), with permission from Elsevier

CHAPTER 8

CONCLUSIONS

8.1 Conclusions

The growth behavior and surface atomic and electronic properties of chalcopyrite $AgInSe_2$ (AIS) have been studied in this work to fulfill a portion of the growing body of knowledge regarding this attractive optoelectronic material that was much needed. Epitaxial growth of AIS on GaAs provided the basis for this study, allowing the surface energetics and growth dynamics to be elucidated from observations on the films as a function of growth direction and temperature. The conditions for epitaxial growth by a hybrid sputtering and evaporation technique were determined, with growth direction and temperature being varied in order to elucidate the significance of these parameters on growth. Throughout this study AIS is compared to the more thoroughly studied related material $Cu(In,Ga)Se_2$ (CIGS) and points out the similarities and differences in growth and surface properties, a necessary step in understanding how the addition of Ag to CIGS or the use of AIS by itself might improve or complicate the resulting devices.

Study of the morphology of the epitaxial AIS films yielded the discovery that the (112) type planes are lowest in energy, with a strong preference of facets forming these planes over any other. Morphological feature size indicates that thermodynamic roughening occurs as growth temperature increases, while the exposed facets become smoother at higher temperatures due to increased adatom mobility resulting in kinetic smoothening. The preference for (112) facets in AIS is akin to CIS, though the striking difference in smoothness observed on CIS (220) between cation and anion terminated facets is much less significant in AIS, indicating that there is less of a difference in the sticking coefficient and atomic diffusion kinetics between two terminations in AIS.

The film structure was studied as a function of temperature and orientation, finding that films are highly aligned, tetragonal, and fully relaxed. The films are single phase, but in some cases an

intermixed epitaxial region between the film and substrate form, which was observed through x-ray diffraction studies and confirmed by transmission electron microscope measurements of the interface cross section. This layer likely aids in accommodating the mismatch in lattice parameter between the film and substrate. Unlike for CIS and some previous AIS studies, there was no substantial evidence for a surface ordered defect compound at the sample surface. Ga from the substrate was observed to diffuse into the AIS film during growth, leaving behind kirkendall voids and forming a Ga profile within the film such that the activation energy of diffusion of Ga in AIS could be calculated.

Scanning tunneling microscopy (STM) studies of the AIS (112)A surface revealed the terrace edge structure, which indicates that the kink formation on AIS is extremely low, and that film growth appears to carry out through screw dislocation mechanism. The terrace height consists of two atomic spacings, consistent with doubled steps. The surface was imaged with atomic resolution, revealing that the atomic positions are near their bulk values, with no significant restructuring within the limit that STM can make this observation. This may indicate a difference in the type of reconstruction for this surface, which would be significant in that it may lead to a significantly different heterojunction behavior from CIS.

Electronic measurements of the surface of AIS by scanning tunneling spectroscopy (STS) find that the surface electronic properties are similar to what would be expected of bulk AIS, including a band gap consistent with the optical gap of 1.25 eV and n-type carrier conduction. These indicate that the defects at the surface do not lead to significant pinning of the Fermi level and that the defects may be similar to those found in the bulk of AIS. Additionally, the surface band edge fluctuations were measured and found to be much lower than in $CuInSe_2$.This is a good indication of a low defect concentration at the surface, and in light of these findings, it seems plausible that AIS-related materials may have potential to out perform CIS.